



Large format LEKID arrays for millimeter-wave astronomy

Shibo Shu

► To cite this version:

Shibo Shu. Large format LEKID arrays for millimeter-wave astronomy. Optics / Photonic. Université Grenoble Alpes, 2019. English. NNT : 2019GREAY042 . tel-02493945

HAL Id: tel-02493945

<https://theses.hal.science/tel-02493945>

Submitted on 28 Feb 2020

HAL is a multi-disciplinary open access archive for the deposit and dissemination of scientific research documents, whether they are published or not. The documents may come from teaching and research institutions in France or abroad, or from public or private research centers.

L'archive ouverte pluridisciplinaire **HAL**, est destinée au dépôt et à la diffusion de documents scientifiques de niveau recherche, publiés ou non, émanant des établissements d'enseignement et de recherche français ou étrangers, des laboratoires publics ou privés.

THÈSE

Pour obtenir le grade de

DOCTEUR DE LA COMMUNAUTE UNIVERSITE GRENOBLE ALPES

Spécialité : **Physique de la Matière Condensée et du
Rayonnement**

Arrêté ministériel : 25 mai 2016

Présentée par

SHIBO SHU

Thèse dirigée par **Eduard DRIESSEN**, Institut de
Radioastronomie Millimétrique
et codirigée par **Karl SCHUSTER**
et co-encadrée par **Martino CALVO**

préparée au sein du **Laboratoire INSTITUT DE
RADIOASTRONOMIE MILLIMÉTRIQUE**
dans **l'ÉCOLE DOCTORALE PHYSIQUE**

Matrices LEKIDs grand format pour l'astronomie millimétrique

Large format LEKID arrays for millimeter- wave astronomy

Thèse soutenue publiquement le **8 octobre 2019**,
devant le jury composé de :

Monsieur Jochem BASELMANS

Professeur, SRON et Delft University of Technology, Rapporteur

Monsieur Simon DOYLE

Professeur adjoint, Cardiff University, Rapporteur

Monsieur Olivier BUISSON

Directeur de Recherche, Institut Néel, Examineur

Monsieur Fabien MALBET

Directeur de Recherche, IPAG, Examineur et Président du jury



Acknowledgments

First, I would like to thank my advisor Dr. Eduard Driessen. I am truly privileged to be the first PhD student advised by him. I am grateful for the time and effort he has patiently put into helping me. He encourages me and supports me through all time.

This thesis would have been impossible without the patient help from Dr. Martino Calvo and Dr. Samuel Leclercq. Martino always helps me push the performance of the instruments to their limits. Samuel always helps me understand all the optical details, which is crucial for this invisible wavelength. I would like to thank Dr. Alessandro Monfardini for supporting our collaboration and endless help with my experiments. I would like to give special thanks to Dr. Karl Schuster, who motivated me to use the phase information to locate resonators. His broad experience and vision always inspired me. I would like to thank Dr. Claude Chapelier and Dr. Nicolas Ponthieu for being my Ph.D. follow-up committee.

Dr. Johannes Goupy helped me with device fabrication and especially on wire-bonding at Institute Neel. Dr. Florence Levy-Bertrand, Dr. Andrea Catalano and Dr. Aurelien Bideaud helped me with cryogenic experiments. Arnoud Barbier and Dominique Billon-Pierron trained and supported me with device fabrications in the IRAM cleanroom. Dominique guided me through my whole life in France. No doubt you are a great woman.

Many thanks to Dr. Charles Romero and Dr. Heather McCarrick for the happy one-month NIKA2 data reduction. Charles also guided me to explore the nature around Grenoble. I would like to thank Dr. Nichol Cunningham, Dr. Edwige Chapillon, Dr. Cinthya Herrera, Dr. Ana Lopez and Sylvain Mahieu for all the activities we

enjoyed. Special thanks to Dina Ferreira who welcomed me warmly every workday. Paolo Della Bosca helped me for all the security training and for bringing us to the NOEMA Observatory. Dr. Bilal Ladjelate helped me during the NIKA2 observation pool at the 30-m telescope. I would like to thank Catherine Berjaud for teaching me French. Many thanks to the whole NIKA2 team who provided me such a great instrument and platform. Many thanks to everyone at IRAM. I would also like to thank Marta Pakovska for your help, smile and blackberries.

Prof. Yutaro Sekimoto guided me into this field six years ago. The optical analysis of LEKIDs would not have been done without his help. I would also like to thank Prof. Wenlei Shan for all the help and discussions from the beginning of my postgraduate study.

I really enjoyed a happy three-year stay in Grenoble. I would like to thank Menyyao He, Tianyi Wei, Dr. Dazhi Lu, Dr. Kewen Shi, Weijia Qian, Zhu Ai, Xiao Xu, Taoran Yan, Detian Xiong, Yixuan He, Te Gai, Qianqian Fu, Wei Li, Yuanyuan Zhai, Li Fan, Dianchun Du, Xiangfeng Guo, Qiangqiang Sun, Dr. Weiguang He, Dr. Yang Li, Dr. Yubing Li, Yanhui He, Dr. Qingyu Wang, Dr. Honghao Gao, Bingyu Zhang, Dr. Jian Wang, Yuxin Lin, Dr. Ji'an Jiang, Dr. Jie Hu, Dr. Zhengwei Li and Dr. Guohua Hu for your companies.

Most importantly, I would like to thank my mother Shu Lu, my father Ping Shu and my family for their unconditional support.

Abstract

Millimeter-wave astronomy contains rich information from the cosmic microwave background to cold matter, like cosmic dust and molecular gas. It is one of the key wavelengths to understand star formation and the evolution of the universe. The IRAM 30-m telescope is one of the largest telescopes in the millimeter wavelength range. It fully covers from the 2 mm to 0.8 mm atmospheric windows. For continuum wave observation, the NIKA2 instrument is designed for the 2 mm and 1 mm windows, and has been producing scientific results since 2017. NIKA2 has angular resolutions of 17.5'' for 2 mm wavelength and 10.9'' for 1 mm wavelength with a 6.5' field-of-view. To cover the 80 mm focal plane, 4-inch kilo-pixel lumped-element kinetic-inductance detector (LEKID) arrays are installed. This thesis studies possible improvements of the LEKID design utilized in the NIKA2 instrument, in order to render the instrument even more powerful in the available frequency windows.

In this thesis, we first introduce the scientific motivation in Chapter 1 and the principles of LEKIDs in Chapter 2. In Chapter 3, the optical response of the current NIKA2 1 mm array is simulated and compared to measurements. The simulation shows that the absorption efficiency is limited by the filling factor. The measurement matches the simulated frequency response. In Chapter 4, we made a small pixel design to improve on-telescope angular resolution. The measurements show that the resolution can be improved from 10.9'' to 10.2'' with the new design. In Chapter 5, we applied the capacitor trimming technique on a compact and quasi lumped-element pixel design. Before trimming only 71% resonators can be used in the limited bandwidth. After trimming a yield of 97% is achieved. In Chapter 6, We further extended this technique on a 4-inch kilo-pixel array design. The optical yield of 76%

is achieved, limited by the readout system and fabrication yield, instead of by the trimming technique. In Chapter 7, we developed a new method to locate the positions of resonators by measuring the reflected phase. We discuss the potential to use this technique on a large format array.

Résumé

L’astronomie des ondes millimétriques contient de précieuses informations allant du fond diffus cosmologique aux matières froides, telles que la poussière cosmique et les gaz moléculaires. C’est l’une des longueurs d’onde clé pour comprendre la région de formation des étoiles et l’évolution de l’univers. Le télescope de 30 m de l’IRAM est l’un des plus grands télescopes aux longueurs d’onde millimétriques. Il couvre entièrement les fentes atmosphériques de 1 mm et 2 mm. Pour l’observation des ondes continues, l’instrument NIKA2 est conçu pour ces deux fentes et a fourni des résultats scientifiques prometteurs depuis 2017. NIKA2 a une résolution angulaire de $17,5''$ pour une longueur d’onde de 2 mm et de $10,9''$ pour une longueur d’onde de 1 mm avec un champ de vue de $6,5'$. Pour couvrir le plan focal de 80 mm, des réseaux de détecteurs à inductance cinétique (LEKID) de 4 pouces de diamètre sont installés. Les LEKID se sont développés rapidement au cours de la dernière décennie grâce à leur structure simple, leurs dimensions adaptables et le besoin de matrices de détecteurs grand format. Cette thèse étudie les possibles améliorations de la structure LEKID utilisée pour l’instrument NIKA2 1 mm, afin de le rendre d’autant plus puissant dans la bande de fréquence disponible.

Dans cette thèse, nous présentons d’abord la motivation scientifique au chapitre 1 et le concept de LEKID au chapitre 2. Dans le chapitre 3, la réponse optique du réseau NIKA2 actuel de 1 mm est simulée et comparée aux mesures. La simulation montre que l’efficacité d’absorption est limitée par le facteur de remplissage. La mesure est en accord à la réponse en fréquence simulée. Au chapitre 4, nous avons conçu un pixel de taille réduite pour obtenir une résolution angulaire plus élevée. Les mesures montrent une amélioration de la résolution de $10,9''$ à $10,2''$ avec le nouveau design.

Dans le chapitre 5, nous avons appliqué une technique de rognage du condensateur à un pixel compact. Avant le rognage, seulement 71% des résonateurs sont exploitables dans la bande passante donnée. Après le rognage, un rendement de 97% est atteint. Dans le chapitre 6, nous avons étendu cette technique à la conception d'une matrice kilo-pixels de 4 pouces de diamètre. Le rendement optique de 76% est atteint, limité par le système de lecture et le rendement de fabrication au lieu de la technique de rognage. Au chapitre 7, nous avons développé une nouvelle méthode pour localiser les positions des résonateurs en mesurant la phase réfléchie. Nous avons discuté de la possibilité d'utiliser cette technique sur une matrice de détecteur grand format.

Contents

1	Introduction	1
1.1	Scientific motivation	1
1.1.1	Cosmic microwave background B-mode polarization	1
1.1.2	Sunyaev-Zel'dovich effect	2
1.2	NIKA2 instrument	4
2	Microwave kinetic inductance detectors	7
2.1	Microwave response of superconductors	7
2.1.1	BCS theory	7
2.1.2	Mattis-Bardeen theory	8
2.1.3	Surface impedance	9
2.2	Principle of MKID	10
2.2.1	Circuit model of LEKID	12
2.2.2	Quality factor	13
2.2.3	Resonator response	14
2.2.4	Optical response	15
2.2.5	Noise	16
2.3	Architectures of MKID focal plane	18
3	Optical response of LEKID arrays	21
3.1	Introduction	21
3.2	Array layout	23
3.3	Simulation method	24
3.3.1	Calculation of absorption efficiency using S-parameters	24

3.3.2	Calculation of absorption efficiency using Surface Loss method	26
3.4	Simulation and measurement of LEKID array	28
3.4.1	Absorption of NIKA2 1mm array	28
3.4.2	FTS measurements	30
3.5	Further analysis	32
3.5.1	Absorption efficiency by different components	32
3.5.2	Absorption efficiency with different materials	34
3.5.3	Absorption efficiency with different pitch sizes	35
3.6	Conclusions	37
4	High angular resolution LEKID	39
4.1	Introduction	39
4.2	Angular resolution of filled array	40
4.3	Angular resolution of NIKA2 instrument	42
4.4	Array Design	42
4.5	Optical measurements	44
4.6	Results and Discussion	47
4.7	Conclusion	49
5	Increased multiplexing of LEKID arrays by trimming the capacitors	50
5.1	Introduction	50
5.2	Characterization before trimming	52
5.2.1	Array design	52
5.2.2	Locating resonators using a beam mapper	54
5.2.3	Resonance frequency deviation	56
5.3	Apply trimming on IDC fingers	57
5.4	Results after trimming	58
5.4.1	Resonance frequency deviation	58
5.4.2	Optical property	60
5.4.3	Quality factor	60
5.5	Conclusion	61

6	Applying capacitor trimming technique on 4-inch LEKID arrays	63
6.1	Introduction	63
6.2	Array design	63
6.3	Characterization before trimming	66
6.4	Trimming process	73
6.5	Characterization after trimming	78
6.5.1	Resonance frequency deviation	79
6.5.2	Quality factor and peak response	82
6.6	Conclusion	84
7	Locating superconducting micro-resonators in darkness	85
7.1	Introduction	85
7.2	Reflected phase of a resonator	86
7.2.1	Theory	86
7.3	Simulation	87
7.4	Measurement on resonators with known positions	88
7.5	Measurement on resonators with unknown positions	93
7.5.1	Array design	93
7.5.2	Measurement	93
7.6	Conclusion	95
8	Conclusions	98
A	Fabrication procedure	101
A.1	Wafer preparation	101
A.2	Deposition of Al device layer	101
A.3	Deposition of backside aluminum	102
A.4	Pattern definition	102
A.5	Pattern re-definition for trimming	102
B	Martin-Puplett Interferometer	104

List of Figures

1.1	The SZ effect	3
1.2	Optics of NIKA2 instrument	4
2.1	Circuit scheme of MKIDs	11
2.2	Readout scheme for MKID using IQ mixer	14
2.3	Resonator response in IQ plane and as S21	15
2.4	Architectures of MKID focal plane arrays	19
3.1	Design parameters for NIKA2 array	25
3.2	Simulation setup and polarizations	27
3.3	S-parameter results from simulation	28
3.4	Absorption efficiency by different components	30
3.5	Comparison of simulation and FTS measurement	31
3.6	Simulated absorption efficiency by different components	33
3.7	Simulated absorption efficiency by using high T_c material	34
3.8	Simulated absorption efficiency with different pitch size	35
4.1	Illustration of the calculation of angular resolution	41
4.2	Comparison of two pixel designs and their expected angular resolution	43
4.3	Simulated crosstalk in the array design	45
4.4	Optical setup of the measurement system	46
4.5	Optical mapping of two arrays and comparison of measured angular resolutions	47
5.1	Resonator design and photo of the trimming process	52

5.2	Comparison of measured resonance frequencies before and after trimming process	53
5.3	Explanation of the resonance frequency deviation using SEM measurement	55
5.4	Design for the trimming frequency	58
5.5	Optical beam mapping after trimming	59
5.6	Internal quality factor before and after trimming	62
6.1	A new LEKID design for 4-inch wafer	64
6.2	Resonance frequencies for 4-inch arrays	65
6.3	Photo of the new 4-inch array	67
6.4	S21 of feedline 1	68
6.5	S21 of feedline 3	69
6.6	S21 of feedline 4	70
6.7	Mapping results of the array	74
6.8	Analytic results for feedline 1	75
6.9	Analytic results for feedline 3	76
6.10	Analytic results for feedline 4	77
6.11	Analytic results for all feedlines	78
6.12	Comparison of Q_i and Q_c before and after trimming	81
6.13	Mapping of the internal quality factors Q_i before and after trimming .	82
6.14	Histogram of peak responses of pixels	83
7.1	Configuration of simulation in Sonnet	87
7.2	Simulation result compared with calculation	89
7.3	Phase measurement setup and the configuration of the array	90
7.4	S11 and S21 results for trimmed array	91
7.5	Comparison of measured and calculated phase	92
7.6	Phase results of S11 and S22 for simple design	94
7.7	Analysis of S11 and S22 for simple design	96
B.1	Setup of Martin-Puplett interferometer	105

List of Tables

3.1	Absorption efficiency of the NIKA2 1mm arrays	32
3.2	Averaged absorption efficiency of the inductor	36
4.1	Characterization of the two arrays	48
6.1	Feedline configuration	66
6.2	Numbers of resonators before and after trimming	71
6.3	Fitting results of resonance frequency deviation after trimming	79
A.1	Properties of evaporated Al film. Credit: Gregoire Coiffard	102

Chapter 1

Introduction

1.1 Scientific motivation

1.1.1 Cosmic microwave background B-mode polarization

Cosmic microwave background (CMB) is the leftover radiation from the 3000 K plasma when the universe was about 380 000 years old. At that time, photons could only travel for a very short range due to scattering and thus the whole universe was opaque for photons, like a blackbody. As the universe expanded, the plasma cooled and the universe became more and more transparent for photons. In 1965, Arno Penzias and Robert Wilson detected this radiation and identified it is from the sky and not the earth [1, 2]. This was achieved by cooling the receiver down to 4 K. Thanks to the successful launches of the three satellites COBE, WMAP and Planck, the blackbody spectrum of the CMB [3], the temperature anisotropy [4] and the full-sky E-mode polarization [5] are well observed. The spectrum of the CMB is well described by a blackbody function with temperature $T = 2.725$ K. That the CMB is remarkably uniform with temperature fluctuations $\Delta T/T$ at a level of 10^{-5} .

The polarized CMB signal can be separated in two types: E-mode and B-mode. The E-modes are caused by Thompson scattering and were first observed by DASI [6]. The B-modes can be created by gravitational lensing of E-modes, which was observed by BICEP2 [7], SPT [8] and POLARBEAR [9], and gravitational wave rising from cosmic inflation. From the B-mode polarization signal, generated by primordial grav-

itational waves, we can understand the physics of inflation and the mechanism of primordial gravitational waves. However, the B-mode polarization signal generated by inflation is still not measured.

Several groups proposed to launch a next generation satellite to observe B-mode polarization signal such as the LiteBIRD satellite [10]. Some ground-based projects are still trying to detect B-mode at large scale such as BICEP Array [11], SPT-3G [12], Simons Observatory [13] and CMB-S4 [14].

1.1.2 Sunyaev-Zel'dovich effect

Beside the polarization signals, there are also secondary anisotropies in the CMB signal. The Sunyaev-Zel'dovich (SZ) effect [15, 16] is one of them. There are two kinds of SZ effects: the thermal SZ effect (tSZE) and the kinetic SZ effect (kSZE). The tSZE is caused by the inverse Compton scattering of CMB photons off the hot electrons in galaxy clusters[17]. This modifies the CMB spectrum in a distinctive frequency-dependent manner. The CMB temperature is increased for the frequency range from 218 GHz to 800 GHz and decreased for frequency below 218 GHz, shown in Fig. 1.1. This feature can be identified by observing CMB photons at different frequencies. Observations of tSZE provide a lot of information about clusters, like the mass and temperature. The important feature of tSZE is that this effect is independent of redshift, so tSZE can be used to detect distant clusters. The tSZE has been observed in many surveys, like Planck[18], ACT[19] and SPT[20] and has been also studied using NIKA[21] and NIKA2[22] instruments.

The kSZE is caused by the hot electrons interacting with the CMB photons. The motions of the hot electrons acts like a moving mirror and reflects the CMB photons[23]. The CMB spectrum is then shifted to a new temperature, shown in Fig. 1.1. From the observations of kSZE we can tell the total baryon mass from the optical depth and the velocities of the clusters. Since the level of tSZE is generally at least an order of magnitude larger than the kSZE in general, it is harder to measure kSZE. The first detection of the kSZE was made by stacking ACT maps on the SDSS

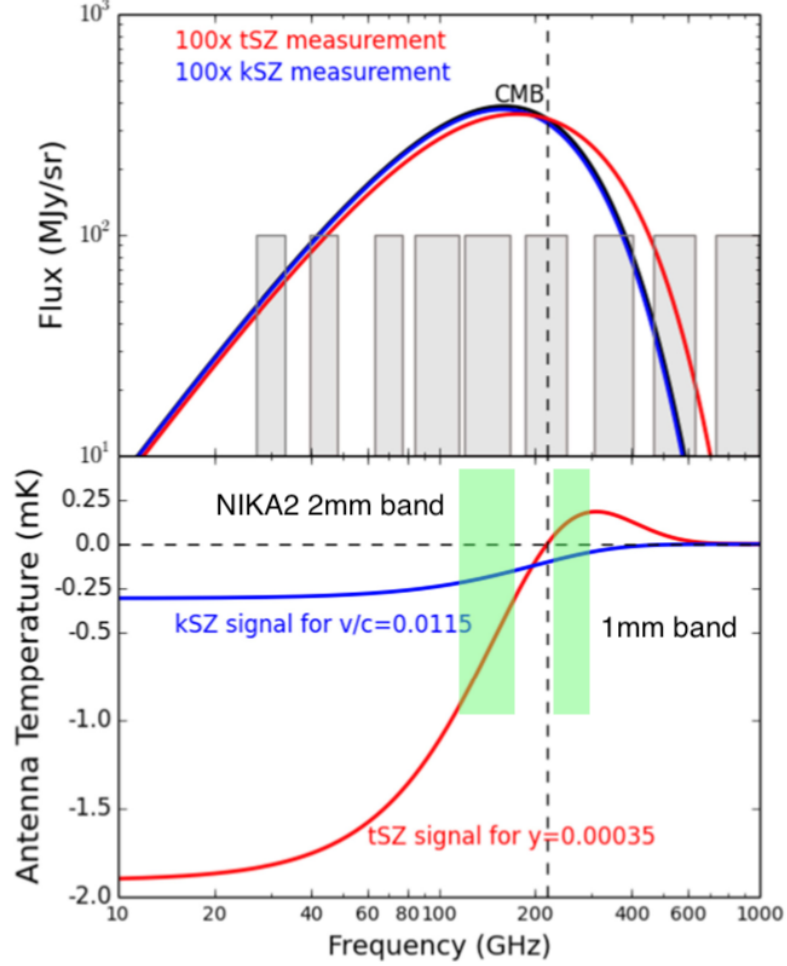


Figure 1.1: The SZ effect on the CMB spectrum. The upper panel shows the flux of tSZE and kSZE which are magnified by 100 times. The grey parts show the observation bands of Planck satellite. The lower panel shows the difference of temperature spectrum between SZE and CMB. v is the velocity of the cluster and y is the Compton value. The dashed lines show the tSZE null at 217 GHz. Two NIK A2 bands are also plotted. Modified from [23]

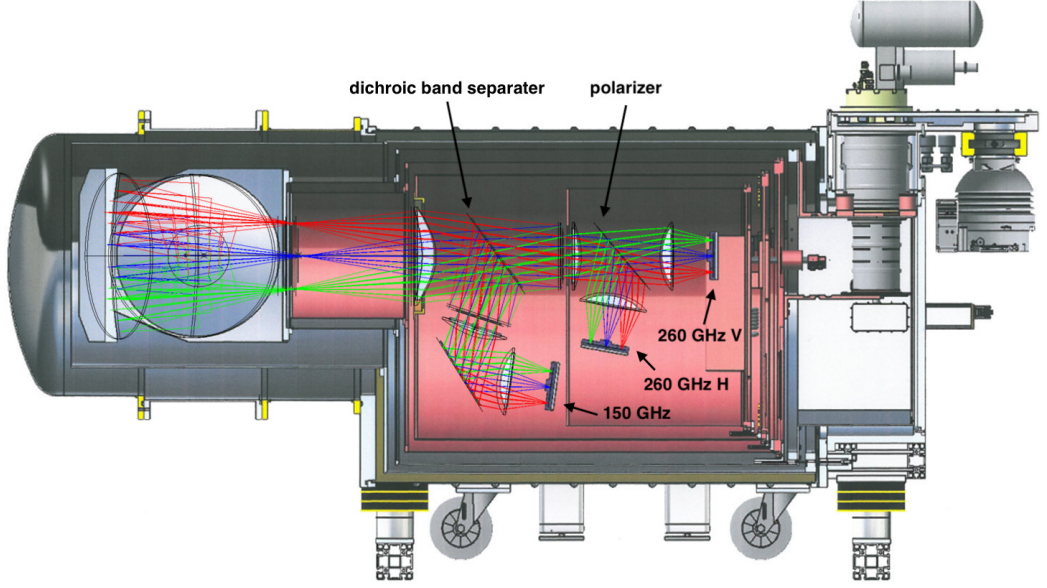


Figure 1.2: The cryostat and cold optics of the NIK A2 instrument. The incident light is first separated by the dichroic into two bands: 150 GHz and 260 GHz. For the 260 GHz band, the light is divided into two linear polarizations, which are detected by two single LEKID arrays.

survey [24].

To study SZE, the NIK A2 instrument is one of the powerful tools, due to its large field-of-view, high-sensitivity and the high-angular resolution of the 30-m telescope.

1.2 NIK A2 instrument

The New IRAM KID Array 2 (NIK A2) is the successor of the NIK A instrument at the IRAM 30-m telescope operating for millimeter astronomy. NIK A had 132 pixels at 150 GHz and 224 pixels at 240 GHz with an instantaneous field-of-view of 2 arc-minutes. After three open science runs, NIK A is replaced by NIK A2 from 2015. During science runs, NIK A shows its promising capability on SZ effect [21] and interstellar medium [25].

The NIK A2 collaboration consists of more than 50 collaborators from Institut Néel, CEA Saclay, IPAG, LPSC, Cardiff University, IRAP, LAM, IAS, IRAM and so on. The principle investigators are Alain Benoit and Alessandro Monfardini from Institut Néel, where the instrument was built and tested.

Both NIKA and NIKA2 [26, 27] are based on microwave kinetic-inductance detectors (MKIDs), which will be introduced in the next chapter. NIKA2 consists of one 616-pixel array for the 150 GHz band and two 1140-pixel arrays for the 260 GHz band. The current NIKA2 260 GHz array is designed to fully cover the 80 mm diameter focal plane (6.5 arc-minutes field-of-view) with a large effective absorption area. Two frequency bands are separated by a dichroic band separator, shown in Fig. 1.2. For 260 GHz band, two arrays are placed after a polarizer, providing dual-polarization detection. The arrays are cooled down to a base temperature of 150 mK by a dilution fridge and two pulse tubes. This huge instrument has a total weight of around 1.3 tons. The weight of the 150 mK stage is about 100 kg, which takes approximately one week to cool down.

There are 8 feedlines for each 260 GHz array and 4 feedlines for the 150 GHz array. Each feedline has a 500 MHz bandwidth, determined by the NIKEL readout system [28]. The 150 GHz array has ~ 150 pixels with frequency spacing ~ 3.3 MHz. The pixel size is $1.8 \times 1.8 \text{ mm}^2$, corresponding to $0.58 F\lambda$ for 27.5 m effective aperture, and the pitch size is ~ 2.2 mm. The expected full-width half-maximum angular resolution is $16.4''$, quite close to the diffraction limit of $15.4''$. Also this array is sensitive to two polarizations. The 260 GHz array has ~ 143 pixels per feedline with frequency spacing ~ 3.5 MHz. The pixel size is $\sim 1.6 \text{ mm}$, corresponding to $0.9 F\lambda$ for 27.5 m effective aperture, and the pitch size is $\sim 2 \text{ mm}$. The expected angular resolution is $10.4''$ and could be improved, compared with the diffraction limit of $8.9''$.

Currently the NIKA2 instrument is the only MKID-based millimeter-wave continuum instrument scientifically running. Therefore, it is necessary to keep improving the performance of the NIKA2 detectors. Based on the current cryostat and optical design, we list some possible upgrades for NIKA2 detectors:

- Deeply understanding the optical performance of the current focal plane design (Chapter 3)
- Development of small-size pixels to increase the angular resolution (Chapter 4)

- Increasing the number of usable pixels: improvement on the detector part (Chapter 5, 6 and 7) and improvement of the readout bandwidth from the current 500 MHz to 1 GHz
- Development of two single-polarization sensitive arrays for all three arrays and replace the polarizer with another dichroic for three-band observations

Part of these upgrades are funded by ANR LabEx FOCUS ANR-1-LABX-0013. To study these upgrades, understanding the detection mechanism is necessary. In the next chapter, I will introduce the basics of superconductivity and the principle of microwave kinetic inductance detectors.

Chapter 2

Microwave kinetic inductance detectors

2.1 Microwave response of superconductors

2.1.1 BCS theory

Superconductivity was discovered by Heike Kamerlingh Onnes in 1911 [29]. When a superconductor is cooled down below a certain critical temperature T_c , the electrical resistance becomes zero and the magnetic flux is expelled from the interior of the superconductor. In 1957, a complete microscopic theory of superconductivity was proposed by Bardeen, Cooper and Schrieffer [30], known as the BCS theory, after their initials. The basic idea of BCS theory is that the superconducting current is carried by Cooper pairs which are pairs of electrons interacting through the exchange of phonons. Cooper pairs are bound together with a binding energy Δ_0 , which is given by

$$2\Delta_0 \approx 3.52k_B T_c, \quad (2.1)$$

at $T = 0$ K and k_B is the Boltzmann constant. Cooper pairs are responsible for the supercurrent and the quasiparticles cause the ohmic losses in the superconducting state. At nonzero temperature, Cooper pairs can be broken by phonons into quasiparticles which can be treated as fermionic particles. These quasiparticles give rise to the temperature dependence of binding energy. For the temperature range $T/T_c < 0.3$,

in which MKIDs work, the binding energy $\Delta(T) \approx \Delta_0$ and for temperature close to T_c the binding energy can be written as [30]

$$\Delta(T) = 3.2k_B T_c \sqrt{1 - (T/T_c)^2}. \quad (2.2)$$

The quasiparticle density is given by [31]

$$n_{\text{qp}} = 4N_0 \int_{\Delta}^{\infty} N_s(E) f(E) dE, \quad (2.3)$$

where N_0 is the single-spin density of states at the Fermi surface and for Al $N_0 = 1.72 \times 10^{10} / \mu\text{m}^3 \text{eV}$ [32]. $N_s(E)$ is the normalized density of states of quasiparticle, given by

$$N_s(E) = \frac{E}{\sqrt{E^2 - \Delta^2}} \quad (2.4)$$

and $f(E)$ is the Fermi-Dirac distribution

$$f(E) = \frac{1}{1 + e^{-\frac{\Delta}{k_B T}}}. \quad (2.5)$$

For a thermal quasiparticle distribution and $T \ll T_c$, the quasiparticle density n_{qp} can be approximated as

$$n_{\text{qp}} \approx 2N_0 \sqrt{2\pi k_B T \Delta} \exp(-\Delta/k_B T). \quad (2.6)$$

2.1.2 Mattis-Bardeen theory

The complex conductivity of superconductor can be expressed by

$$\sigma = \sigma_1 - i\sigma_2. \quad (2.7)$$

The first term σ_1 relates to the loss caused by the oscillation of quasiparticles and the second term $i\sigma_2$ corresponds to the response of Cooper pairs, which have finite inertia, under high frequency field. The complex conductivity can be calculated

using the Mattis-Bardeen theory. After having the complex conductivity, the complex impedance could be calculated, which will be discussed in the next section.

At a given angular frequency w , the two terms of Eqn. 2.7 can be calculated from the Mattis-Bardeen theory[33]:

$$\begin{aligned}\frac{\sigma_1}{\sigma_n} &= \frac{2}{\hbar\omega} \int_{\Delta}^{\infty} \frac{[f(E) - f(E + \hbar\omega)] |E^2 + \Delta^2 + \hbar\omega E|}{\sqrt{E^2 - \Delta^2} \sqrt{(E + \hbar\omega)^2 - \Delta^2}} dE \\ &\quad + \frac{1}{\hbar\omega} \int_{\min\{\Delta - \hbar\omega, -\Delta\}}^{-\Delta} \frac{[1 - 2f(E + \hbar\omega)] |E^2 + \Delta^2 + \hbar\omega E|}{\sqrt{E^2 - \Delta^2} \sqrt{(E + \hbar\omega)^2 - \Delta^2}} dE \\ \frac{\sigma_2}{\sigma_n} &= \frac{1}{\hbar\omega} \int_{\max\{\Delta - \hbar\omega, -\Delta\}}^{\Delta} \frac{[1 - 2f(E + \hbar\omega)] |E^2 + \Delta^2 + \hbar\omega E|}{\sqrt{\Delta^2 - E^2} \sqrt{(E + \hbar\omega)^2 - \Delta^2}} dE\end{aligned}\quad (2.8)$$

where σ_n is the normal-state conductivity. The first term of σ_1 is associated with the response of the quasiparticles to a high frequency field and the second term presents the response of the Cooper pairs to a high frequency field, relevant only for $\hbar\omega > 2\Delta$. σ_n can be measured at the low-temperature-resistance plateau when $T > T_c$. In the limit of $\hbar\omega \ll \Delta$ and $k_B T \ll \Delta$, Eqn. 2.8 can be simplified as

$$\begin{aligned}\frac{\sigma_1}{\sigma_N} &= \frac{4\Delta}{\hbar\omega} \exp\left(-\frac{\Delta}{k_B T}\right) \sinh\left(\frac{\hbar\omega}{2k_B T}\right) K_0\left(\frac{\hbar\omega}{2k_B T}\right) \\ \frac{\sigma_2}{\sigma_N} &= \frac{\pi\Delta}{\hbar\omega} \left[1 - 2 \exp\left(-\frac{\Delta}{k_B T}\right) \exp\left(-\frac{\hbar\omega}{2k_B T}\right) I_0\left(\frac{\hbar\omega}{2k_B T}\right)\right]\end{aligned}\quad (2.9)$$

where, I and K are zeroth-order modified Bessel functions of the first and second kind, respectively. To further understand the change of the conductivity due to incoming photons, the derivative of Eqn. 2.9 can be derived as [34]

$$\begin{aligned}\frac{d\sigma_1}{dn_{qp}} &\simeq \sigma_N \frac{1}{N_0 \hbar\omega} \sqrt{\frac{2\Delta_0}{\pi k_B T}} \sinh\left(\frac{\hbar\omega}{2k_B T}\right) K_0\left(\frac{\hbar\omega}{2k_B T}\right) \\ \frac{d\sigma_2}{dn_{qp}} &\simeq \sigma_N \frac{-\pi}{2N_0 \hbar\omega} \left[1 + 2 \sqrt{\frac{2\Delta_0}{\pi k_B T}} \exp\left(\frac{-\hbar\omega}{2k_B T}\right) I_0\left(\frac{\hbar\omega}{2k_B T}\right)\right].\end{aligned}\quad (2.10)$$

2.1.3 Surface impedance

The surface impedance can be calculated using the complex conductivity discussed in the last section. The nonzero impedance of a superconductor in AC field is expressed

by,

$$Z_s = R_s + i\omega L_s, \quad (2.11)$$

where R_s is the surface resistance and L_s is the surface (kinetic) inductance. For dirty limit, which means the mean free path limits the coherence length, the surface impedance can be expressed by [35]

$$Z_s = \sqrt{\frac{i\mu_0\omega}{\sigma_1 - i\sigma_2}} \coth \left(d\sqrt{i\omega\mu_0(\sigma_1 - i\sigma_2)} \right) \quad (2.12)$$

where μ_0 is the magnetic constant and d is the thickness of film. σ_1 and σ_2 can be calculated from Eqn. 2.8. In this thesis we use Al thin film, which is in the dirty limit. For $\sigma_1 \ll \sigma_2$, which means the surface resistance can be negligible, the surface resistance and inductance can be calculated as [34]

$$R_s = \mu_0\omega\lambda\frac{\sigma_1}{2\sigma_2}\beta \coth \left(\frac{d}{\lambda} \right) \quad (2.13)$$

$$L_s = \mu_0\lambda \coth \frac{d}{\lambda} \quad (2.14)$$

with $\beta = 1 + \frac{2d/\lambda}{\sinh(2d/\lambda)}$. For the bulk limit, $\beta = 1$ and for the thin film limit $\beta = 2$. The penetration depth is expressed as $\lambda = 1/\sqrt{\mu_0\omega\sigma_2}$. The surface inductance can also be calculated from the measured surface resistance as [36]

$$L_s = \frac{\hbar R_s}{\pi\Delta}. \quad (2.15)$$

2.2 Principle of MKID

Microwave kinetic inductance detector (MKID) is a kind of non-equilibrium superconducting detector, which takes advantage of the kinetic inductance of superconductors [37–39]. MKID is based on superconducting resonators, as shown in Fig. 2.1. Each resonator has a specific resonance frequency determined by the capacitance and inductance of the resonator. When an incident photon has energy larger than the superconducting gap ($\hbar\nu > 2\Delta$), it can break Cooper pairs and create quasi-particles,

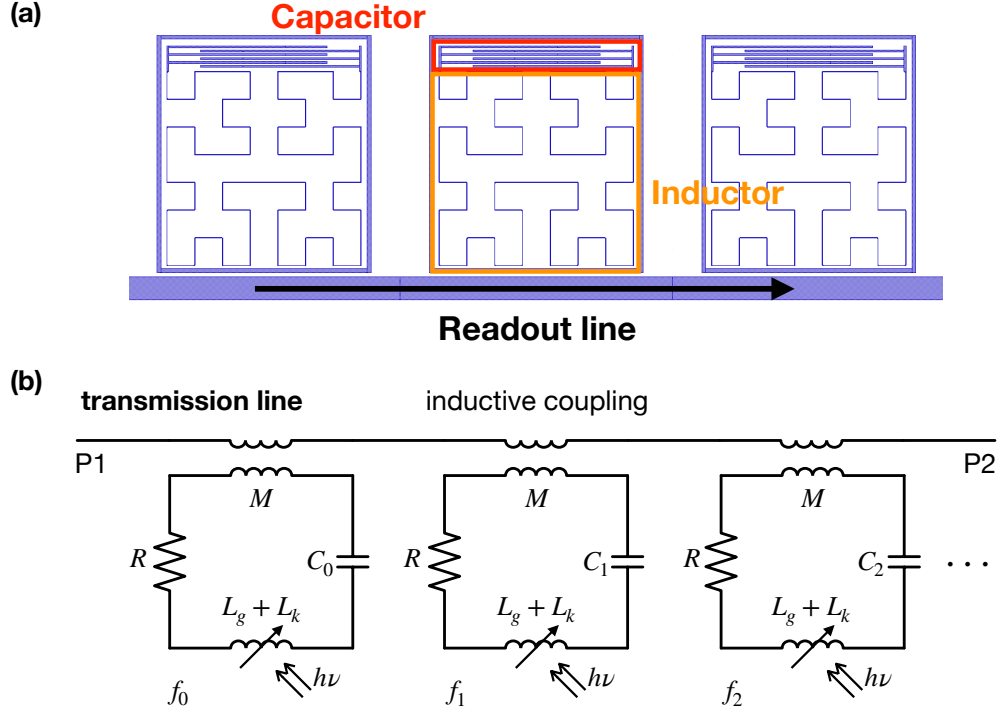


Figure 2.1: (a) Design of LEKID read out by a microstrip line. The inductor part is designed as a large absorber for optical coupling. The capacitor is used to tune the resonance frequency. (b) The circuit scheme of (a). The inductor part is simplified as geometry and kinetic inductors. The kinetic inductance changes due to the incident photons.

thereby modifying σ_2 and σ_1 , respectively. These changes reduce the resonator frequency and increase its losses, resulting in a shallower resonance dip at lower frequencies. This can be read out using. The resulting changes of resonance amplitude and phase response can be read out using a homodyne technique using a single frequency tone at microwave frequencies. Based on the intrinsic frequency multiplexing property, hundreds of resonators can be read out simultaneously, through a single feedline.

The traditional MKIDs are based on superconducting transmission line such as microstrip line and coplanar waveguide. The resonator has two different designs due to the resonance type: quarter-wave shorted end and half-wave open end. Instead of using distributed capacitance and inductance of transmission line, the lumped-element kinetic-inductance detector (LEKID) [40], consists of a lumped-element inductor and capacitor. The inductor part is designed to absorb the incident photons and the resonance frequency is tuned by changing the capacitance.

2.2.1 Circuit model of LEKID

Each LEKID is a superconducting LC resonator coupled either capacitively or inductively to a feedline. In Fig. 2.1, a circuit diagram is plotted for inductively coupled LEKIDs, which is the case in this thesis. The resonance frequency of each resonator is determined by the inductance and the capacitance, given by

$$f_r = \frac{1}{2\pi\sqrt{LC}}. \quad (2.16)$$

By changing the capacitance of each resonator the resonance frequency can be tuned individually. The inductance has geometric inductance L_g and kinetic inductance L_k . The geometric inductance L_g , also called magnetic inductance, is determined by the length, width, thickness and shape of the inductor and does not change under optical load. The kinetic inductance L_k is sensitive to quasiparticles which can be created by absorbing photons. To have the same sensitivity, all resonators usually share the same inductor design. Multiplexing is done by changing the capacitance of

the individual pixels.

2.2.2 Quality factor

A single feedline can read out hundreds of resonators by frequency-domain multiplexing. In Fig. 2.1, each resonator is coupled inductively to the feedline. The coupling intensity is described by the coupling quality factor Q_c , determined by the coupling structure. The width of resonance and the energy inside a resonator is directly related with Q_c . The internal quality factor of the resonator Q_i is defined as the energy stored over lost per cycle in the resonator itself, given by [41]

$$Q_i = \frac{\omega E}{P_{loss}} = \frac{1}{\alpha_k} \frac{\omega L_s}{R_s}, \quad (2.17)$$

where $\alpha_k = L_k/(L_k + L_g)$ is the fraction of kinetic inductance. R_s is the surface resistance describing the loss caused by quasiparticles. The calculation of R_s and L_s is discussed in Sec. 2.1.3. In dark environment the measured Q_i can achieve values up to 10^7 [42–44] but this is still much lower than the prediction from Eqn. 2.17. Some groups suggest that the extra loss is likely caused by two-level systems [45, 46]. When the resonator is used as photon detector, the background radiation can break Cooper pairs and create quasiparticles. Therefore, in the working status, the loss caused by photons is usually much larger than the intrinsic loss. Typically for observation condition in the NIKA2 instrument, Q_i is from 1×10^4 to 1.5×10^4 . This gives us a reference to design Q_c because the total quality factor Q_r is given by

$$\frac{1}{Q_r} = \frac{1}{Q_c} + \frac{1}{Q_i}. \quad (2.18)$$

In phase readout, the responsivity is proportional to Q_r , which has the maximum value when $Q_c = Q_i$, so Q_c is designed to be from 1×10^4 to 1.5×10^4 in our case. When $Q_c = Q_i$, the dip on S21 is -6 dB lower than the baseline and is easily observed from S21 spectrum with a vector network analyzer.

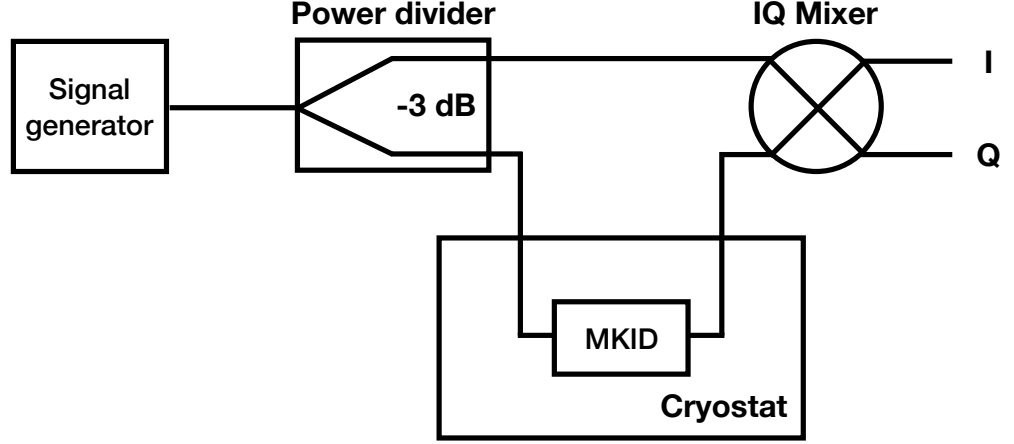


Figure 2.2: Readout scheme for MKID using IQ mixer.

2.2.3 Resonator response

For the frequency range close to the resonance frequency, the complex response can be expressed by the scattering parameter [47]

$$S_{21}(f) = Ae^{-2\pi j f \tau} \left(1 - \frac{Q_r/Q_c}{1 + 2jQ_r x} \right) \quad (2.19)$$

$$x = \frac{f - f_r}{f_r}$$

where A is a complex scale factor and $e^{-2\pi j f \tau}$ is the term to correct the cable delay with delay time τ . This complex response is shown in Fig. 2.3 together with the magnitude $|S_{21}|^2$.

To read out the resonator response, which consists of both the phase and amplitude information, a quadrature mixer (IQ mixer) is usually used, as shown in Fig. 2.2. The microwave signal is first fed to a power divider, after which one signal is sent to the device and the other one is used as the local oscillator (LO) signal of the IQ mixer. The signal transmitted after the device is inputted as the RF signal of the IQ mixer. In the IQ mixer, the LO and RF signals are mixed to have the in-phase component

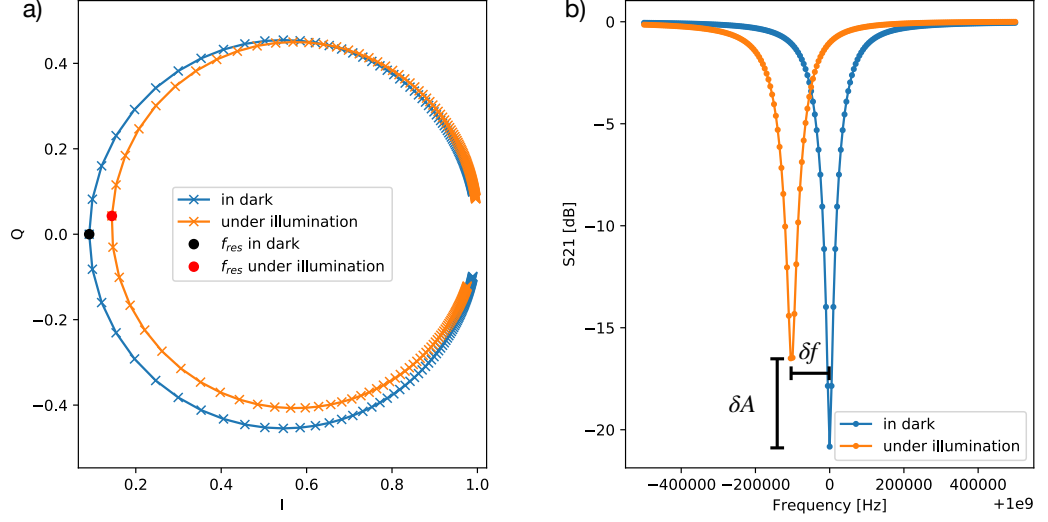


Figure 2.3: (a) Response of a resonator in IQ plane. (b) Response of a resonator as magnitude of S21.

I. The LO and the 90-degree-shifted RF signals are mixed to get the quadrature component *Q*. Then the full complex response of the measured device can be built from *I* and *Q*. The detector response is then converted from this complex response, introduced in Appendix C.

2.2.4 Optical response

Due to the complex response of resonator, there are two quantities, the amplitude and the phase, to measure the resonator response caused by incident photons. The amplitude readout is also called dissipation readout since the amplitude is determined by Q_i . From Eqn. 2.17, we have [48]

$$Q_i = \frac{1}{\alpha} \frac{\omega L_s}{R_s} = \frac{2}{\alpha_k \beta} \frac{\sigma_2}{\sigma_1} \quad (2.20)$$

and $\beta = 1 + \frac{2d/\lambda}{\sinh(2d/\lambda)}$. When $T \ll T_c$ we have $\delta\sigma_1 \gg \delta\sigma_2$ and a change in the internal quality factor is given by

$$\delta \left(\frac{1}{Q_i} \right) = \frac{\alpha_k \beta}{2} \frac{\delta\sigma_1}{\sigma_2}. \quad (2.21)$$

For a small frequency shift, a change in the frequency is expressed by

$$\frac{\delta\omega_0}{\omega_0} = \frac{\alpha_k\beta}{4} \frac{\delta\sigma_2}{\sigma_2}. \quad (2.22)$$

In the readout scheme, the Q_i and ω are usually derived from the fitting of IQ plane. Instead the amplitude and phase can be measured directly, so the response of the amplitude and phase due to a change in the number of quasiparticles can be expressed by [48]

$$\begin{aligned} \frac{dA}{dN_{qp}} &= -\frac{\alpha_k\beta Q}{|\sigma|V} \frac{d\sigma_1}{dn_{qp}} \\ \frac{d\theta}{dN_{qp}} &= -\frac{\alpha_k\beta Q}{|\sigma|V} \frac{d\sigma_2}{dn_{qp}} \end{aligned} \quad (2.23)$$

where V is the sensitive volume of the superconductor, i.e. the inductor in the case of a LEKID. In the limit of $\hbar\omega \ll \Delta$ and $k_B T \ll \Delta$, $d\sigma_1/dn_{qp}$ and $d\sigma_2/dn_{qp}$ are given by Eqn. 2.10. The change on the total number of quasiparticles is given by

$$\frac{dN_{qp}}{dP} = \frac{\eta_{qp}\tau_{qp}}{\Delta_0}, \quad (2.24)$$

where τ_{qp} is the quasiparticle lifetime and η_{qp} is the quasiparticle-creation efficiency with optical power. For our Al at about 300 GHz, a typical value for η_{qp} is about 0.45 [49].

2.2.5 Noise

For a MKID, the detection of photons is based on the generation of quasiparticles by breaking Cooper pairs. The quasiparticles will recombine to Cooper pairs after the lifetime of quasiparticle τ_{qp} . This process is called the generation and recombination (g-r) of quasiparticles and the fluctuation of quasiparticle number is an intrinsic noise source for MKIDs. The noise-equivalent power (NEP) of g-r noise is given by [50]

$$\text{NEP}_{gr} = \frac{2\Delta}{\eta_{qp}} \sqrt{\frac{N_{qp}}{\tau_{qp}}}. \quad (2.25)$$

For an ideal photon detector, the photon statistic noise should be the dominant noise source. The NEP of a thermal source is given by [39, 51]

$$\text{NEP}_{ph} = \sqrt{2P_o h\nu (1 + n_0)} \quad (2.26)$$

where the mean photon occupancy of a single mode $n_0 = 1/(e^{h\nu/k_B T} - 1)$ with frequency ν , the absorbed power from this mode $P_o = n_0 B h\nu$ and the optical bandwidth B . Since $B \ll \nu$, we assume both the absorption efficiency and the occupancy are constant in the bandwidth B . After coupling the source noise with MKID, the background limited instrument performance (BLIP) in terms of NEP is given by

$$\text{NEP}_{\text{BLIP}}^2 = \int (2P_o h\nu + 2P_o h\nu m n_0 + 4\Delta P_\nu / \eta_{qp}) d\nu \quad (2.27)$$

with

$$P_\nu \approx \frac{1}{2} \eta_{op}(\nu_0) B_s(\nu) \lambda^2 F(\nu). \quad (2.28)$$

In this equation $m = \eta_{op} F(\nu)$ is the total efficiency of photon absorption between the source and the MKID, η_{op} is the total optical efficiency, B_s is the blackbody spectrum of the source and F is the angular response of the MKID.

A low noise amplifier is usually used at the 4K stage after the detector. The amplitude noise of the readout signal is limited by the amplifier noise. The NEP of amplifier is given by [52]

$$\text{NEP}_{amp} = \frac{Q_c}{Q^2} \sqrt{\frac{k_B T_{amp}}{4P_g}} R_x^{-1} \quad (2.29)$$

where T_{amp} is the amplifier noise temperature, P_g is the readout tone power and R_x is the responsivity for either amplitude or phase readout.

There is an extra noise source on the device: the two-level systems [53]. When the electric dipoles are coupled to the electric field of the readout signal, the movement of the dipoles causes fluctuations in the dielectric constant of dielectrics. This fluctuation shifts the resonance frequency and causes extra frequency noise.

2.3 Architectures of MKID focal plane

There are mainly three kinds of architectures for MKIDs for millimeter and sub-millimeter wave detection. The first architecture is to use a planar antenna to couple the signal to the MKID. In Fig. 2.4(a), it shows a planar slot antenna design, sensitive to a single polarization. To increase the antenna gain, lenses, usually made from silicon, are placed in front of the antennas [54, 56]. The planar antenna can also be designed as a phased array which consists of many slot antennas in a single pixel [57]. With this planar antenna design, the optical properties are determined by the antenna design, including the lenses. Silicon lenses have a drawback that the high dielectric constant ~ 11.7 causes a high reflection. This can be solved by applying anti-reflection coating on the surface of silicon lenses [58, 59]. By using Al-NbTiN hybrid MKID, the sensitive Al trace can be designed separately from the resonator design, so the sensitivity can be tuned individually.

The phased array antenna is also a planar design but without lenses [57]. Therefore, some incident photons might be absorbed by MKIDs directly bypassing the antenna. For a $\lambda/4$ resonator design, the size of the resonator could be as large as 1 cm, so the directly absorbed energy is not negligible. To solve this problem, a delicate coupling structure has been designed [60].

The second architecture is the horn-coupled MKID. The main advantage of using a horn is that the horn design has been well studied for decades, the optical behavior is well understood and it is suitable for a large frequency range. To achieve the simplest design, the inductor of LEKID can be placed after the horn as an absorber, as shown in Fig. 2.4(c). Using two inductors, the detection of two polarizations is possible [61, 62]. To achieve multichroic detection, a coupling structure and a filter between the horn and the detector are needed. A planar ortho-mode transducer is developed for coupling both polarizations [63–65]. A diplexer is then used to separate two pass-bands. The disadvantage of this architecture is that the horn size limits the number of detectors on the focal plane.

The third architecture, which is the main focus of this thesis, is based on bare

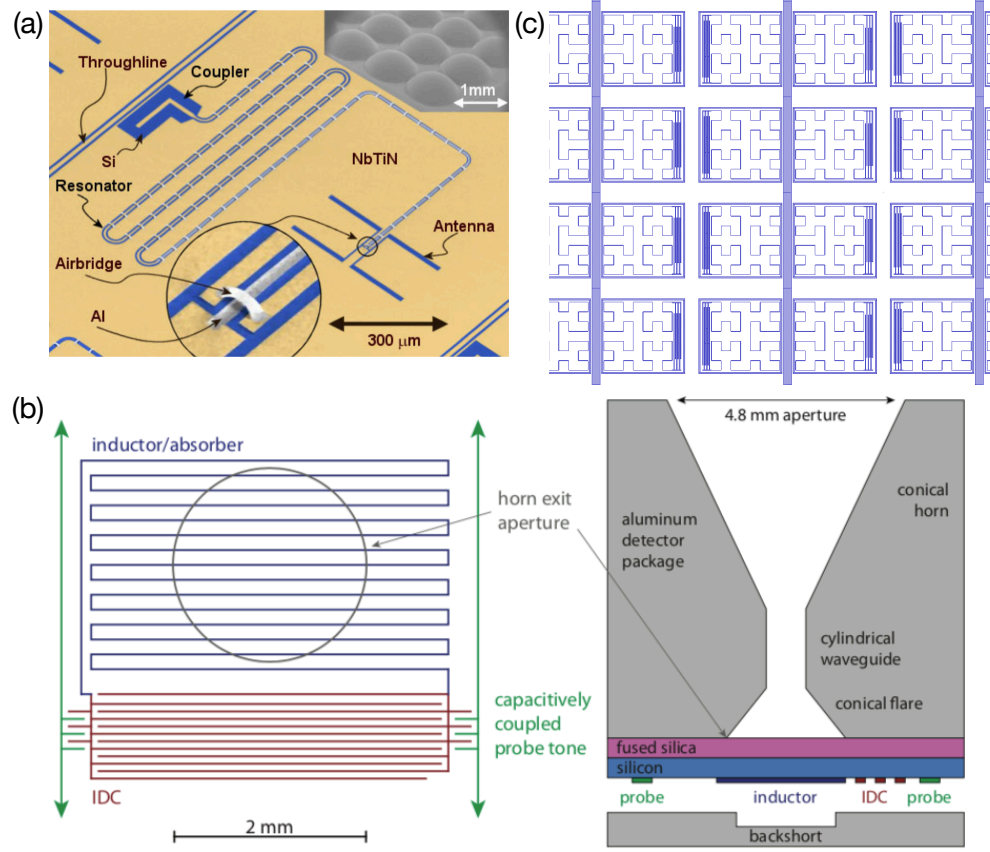


Figure 2.4: Architectures of MKID focal plane arrays. (a) Planar antenna coupled MKID setup. The sensitive part is the central Al trace of the coplanar waveguide. The coupler part is used for readout. The length of the transmission line determines the resonance frequency. The end of the line is connected to the ground, where a planar slot antenna is connected. The antenna is placed after a silicon lens to focus the light on the antenna. Reprinted from Yates et al. [54]. (b) Bare LEKID setup. On the focal plane, there are only LEKIDs and readout lines. The inductor is designed as an direct absorber to cover an area on the focal plane. (c) LEKID setup after a horn. The inductor here is also designed as absorber, which is placed after a horn, so the optical behavior is mainly determined by the horn. Reprinted from McCarrick et al. [55].

LEKID arrays. The bare LEKIDs are directly placed on the focal plane without any antenna, shown in Fig. 2.4(b). The inductor is designed as an absorber to the incident photons through impedance matching. The optical properties are mainly determined by the instrument and the detectors act as absorbers. The coupling efficiency is related with the filling factor, the ratio between the inductor size and the pitch size. The angular resolution is affected by the size of inductor, which will be discussed in Chapter 4. Since all components are exposed to radiation, the design parameters are linked to each other. For example, the thickness and the width of inductor determine the coupling efficiency and also the volume of inductor, which determines the number of residual quasi-particles and sensitivity. However, its simple structure makes it easy to be developed and the related projects, ARCONS [66], NIKA [67] and NIKA2 [27], have successfully achieved scientific observations.

Chapter 3

Optical response of LEKID arrays

3.1 Introduction

The lumped-element KID (LEKID) [40] consists of a lumped-element inductor and capacitor, which separates the photon-sensitive part, the inductor, and the frequency-tuning part, the capacitor. This separation allows for a more flexible design of the inductor. The inductor can be located after a horn for coupling signal [55, 61], utilizing the well-studied optical response of horn. The inductor can also be designed to absorb the free-space electromagnetic wave directly without any antenna [40]. This bare LEKID design is analyzed in this chapter.

To improve the sensitivity of KIDs, it is necessary to evaluate and maximize the amount of energy absorbed by the inductor. For distributed KIDs, the responsivity depends on the current distribution along the planar transmission line [69]. It can be improved by using a hybrid structure with a high- T_c superconductor to restrict the photons to be absorbed in the most-sensitive part [70]. For horn-coupled LEKIDs, only the inductor part is irradiated and the optical coupling is simply determined by the impedance matching between the inductor and incident wave [61]. For bare

This chapter is partially published as Shu, S., Calvo, M., Goupy, J., Catalano, A., Bideaud, A., Monfardini, A., Leclercq, S. and Driessen, E.F., 2018. Optical Response of Lumped-Element Kinetic-Inductance Detector Arrays. *IEEE Transactions on Terahertz Science and Technology*, 8(6), pp.605-612.[68]

LEKIDs, all components of LEKIDs are exposed to the incident photons, so not only the inductor but the whole pixel may absorb photons. The optical response of the whole pixel has been discussed [71, 72], but the absorption efficiency of only the inductor part has been seldom discussed.

The total efficiency η_{tot} of an instrument using bare LEKID arrays can be expressed as

$$\eta_{tot} = \eta_{opt} F \eta_L \eta_{qp}, \quad (3.1)$$

where η_{opt} is the optical efficiency, F is the filling factor of LEKIDs, η_L is the absorption efficiency of the inductor and $\eta_{qp} \approx 0.45$ is the quasiparticle creation efficiency [49], which is approximately constant for our wavelength of interest with Al. Since η_{opt} is mainly determined by the optics and η_{qp} is determined by the material and the frequency of the incident photon, we focus on the filling factor F and the inductor efficiency η_L . Roesch et al. [72] have investigated the optical response of a bare LEKIDs array in the 2 mm atmospheric band. In their model, the array consists of a set of periodic pixels only, and the readout line is not considered. The absorption efficiency is calculated from the return loss measured using a vector network analyzer. In their analysis the simulation and measurement matched well, however, the connection between the measured response of the KID and the absorption in the pixel is missing.

In this chapter, we demonstrate a thorough electromagnetic analysis of a bare LEKID array, such as the ones used in the NIKA2 instrument [27]. The energy absorbed in the inductor and in other components are separated using the Surface Loss function in the Field Calculator of HFSS [73]. The simulation results are compared to measurements using a Fourier transform spectrometer (FTS). We find that the LEKID array has a large difference of absorption efficiency for the two incident polarizations. Several configurations are simulated to understand the absorption in the different components of the pixel. This analysis can be used for optimization of the design of the focal plane components of LEKID arrays. Extending the analysis to other KID designs is also possible.

3.2 Array layout

The NIKA2 1mm LEKID array [27] (Fig. 3.1) is simulated and measured in this chapter. This array consists of 1140 pixels read out by 8 microstrip feedlines. The size of the array is a circle with radius of 40 mm corresponding to a $6.5'$ field-of-view on the IRAM 30-m telescope. The pixel pitch size and the inductor size are $2 \times 2 \text{ mm}^2$ and $1.6 \times 1.5 \text{ mm}^2$, respectively. Each pixel has the same inductor design with different capacitor finger lengths for different designed resonance frequencies. The back of the wafer is covered with 200 nm thick aluminum, and acts at the same time as ground plane for the microstrip readout feedline and as backshort to optimize the optical coupling.

This array uses the bare LEKID design, which has no antenna structure on the focal plane. The incident light illuminates the array directly. The detection band of the LEKIDs is determined by the backshort distance, which is the thickness of the silicon substrate. The band central frequency (wavelength) is designed to be 260 GHz (1.15 mm), the central part of the 1 mm atmospheric window. The backshort is designed to be $3\lambda_{\text{Si}}/4 = 250 \mu\text{m}$, where the wavelength in silicon $\lambda_{\text{Si}} = \lambda/\sqrt{\epsilon_r} = 333 \mu\text{m}$, the wavelength in free space $\lambda = 1.15 \text{ mm}$ and the relative permittivity of silicon $\epsilon_r = 11.9$. The bandwidth is expected from 230 GHz to 290 GHz, limited by the $3\lambda/4$ backshort distance. Using a $\lambda/4$ backshort will increase the bandwidth to fill the entire 1 mm atmospheric window, but is technologically difficult since it would imply a substrate thickness of 90 μm only.

The inductor is designed with a 3rd-order Hilbert curve [74] for dual-polarization sensitivity. The inductor width and the line spacing are designed as $s = 4 \mu\text{m}$ and $w = 240 \mu\text{m}$, respectively, shown in Fig. 3.1(d). Since the wavelength is much larger than the structure, the inductor can be roughly modeled as a sheet impedance Z_{KID} . The optical coupling can be modeled using the transmission line model [75], shown in Fig. 3.1(c). The impedance of the backshort can be expressed as

$$Z_{\text{bs}} = j Z_{\text{sub}} \tan(\beta l), \quad (3.2)$$

where $\beta = 2\pi/\lambda_{\text{Si}}$ and l is the backshort distance (250 μm). The effective impedance of the KIDs together with the backshort is

$$Z_1 = \frac{1}{\frac{1}{Z_{\text{KID}}} + \frac{1}{Z_{\text{bs}}}}. \quad (3.3)$$

Assuming the reactance is zero, the impedance of KID is

$$Z_{\text{KID}} = R_{\square}/(s/w). \quad (3.4)$$

Then the absorption efficiency is calculated as

$$\text{absorption efficiency} = 1 - |S_{11}|^2 = 1 - \left| \frac{Z_0 - Z_1}{Z_0 + Z_1} \right|^2, \quad (3.5)$$

where the vacuum impedance $Z_0 = 377 \Omega$. Given the sheet resistance $R_{\square} = 1.6 \Omega/\square$ of the used 20 nm aluminium film, $Z_{\text{KID}} = 96 \Omega$, and the maximum absorption is 64.7% at the band center. This is only a simple estimation for the absorption efficiency. Actually, away from the band center, the absorption efficiency largely depends on the reactance of Z_{KID} , which is usually not zero and difficult to be evaluated analytically. Therefore, we use electromagnetic simulations as a useful tool for focal plane array design.

3.3 Simulation method

3.3.1 Calculation of absorption efficiency using S-parameters

For a bare LEKID array, the pixels are arranged repeatedly on the focal plane and the differences of capacitor finger lengths are relatively small compared to the wavelength. Therefore, the full array can effectively be approximated as a single pixel with periodic boundary conditions. This method dramatically decreases the simulation time and enables the analysis of the optical response of the array. All simulations presented in this chapter are simulated in HFSS [73].

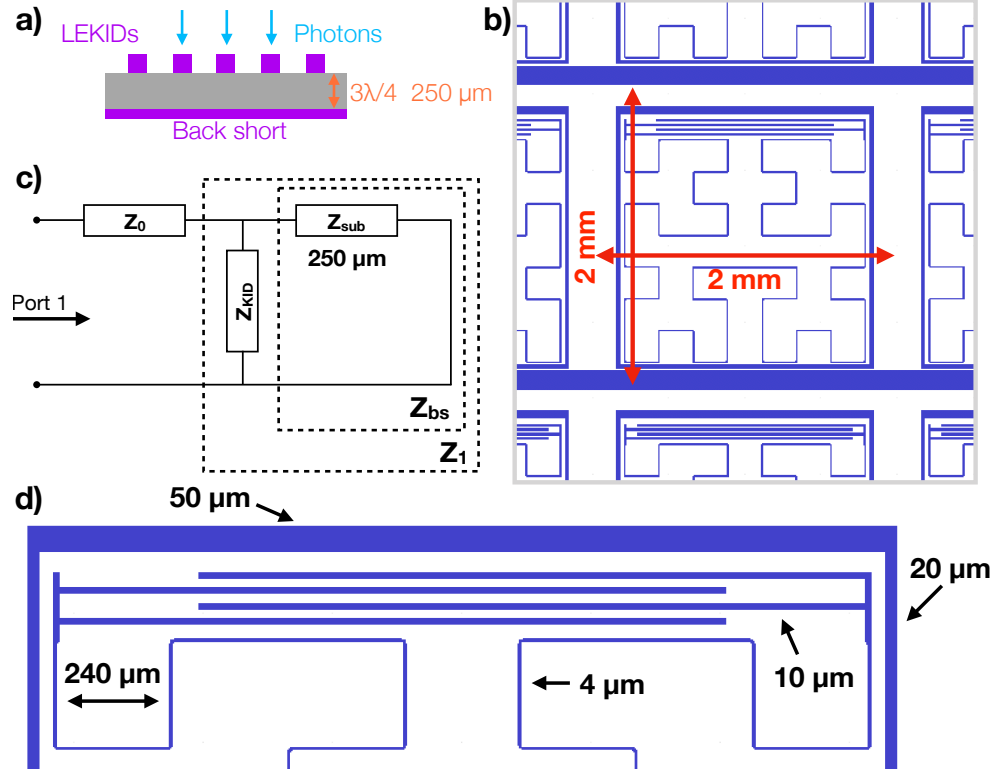


Figure 3.1: a) Cut view of the LEKIDs array in the photon incident direction. b) Schematic drawing of the NIKA2 1mm array. The pitch size is 2 mm. c) Transmission line model of the optical coupling in (a). The LEKID, mainly the inductor, is represented by a sheet impedance Z_{KID} . d) The design geometries of the LEKID pixel. The frame size is $1.6\ \text{mm} \times 1.7\ \text{mm}$ and the readout line width is $120\ \mu\text{m}$.

The pixel is built with a 20 nm thick structure, which is the smallest size in our model. All the metal structures are assigned as either impedance boundaries of $1.6 \Omega/\square$ or perfect electric conductor (PEC), depending on the configurations we are considering. The 200 nm Al backshort is simplified as a PEC boundary assigned to the backside of the substrate, since the absorption efficiency is negligible due to the impedance mismatch. The only excitation port is Port 1, located on top of the model (Fig. 3.2(a)). The four sides of the model are assigned as periodic boundaries.

In our instrument, the incident direction of the focused radiation is perpendicular to the focal plane for all positions, due to our telecentric lens system design [27]. This is similar to a plane wave illumination. In the model, a Floquet port is assigned to Port 1 for exciting plane waves. Considering the simulating frequency from 150 GHz to 350 GHz, 18 modes are included in the analysis based on the mode calculator in HFSS. Two TEM modes, TE_{00} and TM_{00} with y and x -axis polarizations, respectively, are simulated as the incident signal.

The absorption efficiency in the pixel is calculated as

$$AE_{S11} = 1 - \sum_{\text{All modes}} |S11|^2, \quad (3.6)$$

where S11 are the return losses.

3.3.2 Calculation of absorption efficiency using Surface Loss method

The absorption efficiency calculated using Eqn. 3.6 includes the energy absorbed by all components. However, the most sensitive part of a LEKID is the inductor, where the created quasi-particles give rise to the change of readout signal. To extract the energy absorbed by this individual component, we use the surface loss density function in the Field Calculator. The surface loss density is calculated as

$$p_s = Re(\vec{P} \cdot \vec{n}), \quad (3.7)$$

where \vec{P} is the Poynting vector and \vec{n} is the vector normal to the surface. The surface loss is then calculated by integration of the surface loss density over all surfaces of a component,

$$\text{surface loss} = \int_S p_s dS. \quad (3.8)$$

The absorption efficiency calculated from surface loss, AE_{SL} , is given by

$$\text{AE}_{\text{SL}} = \frac{\text{surface loss}}{\text{incident power}}, \quad (3.9)$$

where the incident power is known. In the simulation, the pixel is geometrically separated into four components: the inductor, capacitor, frame, and readout line. Each component has a defined thickness (20 nm). This analysis allows to evaluate the absorption efficiency in each component. The difference between the absorption efficiency calculated from S11 and surface loss is negligible and discussed in Sec. 3.4.1

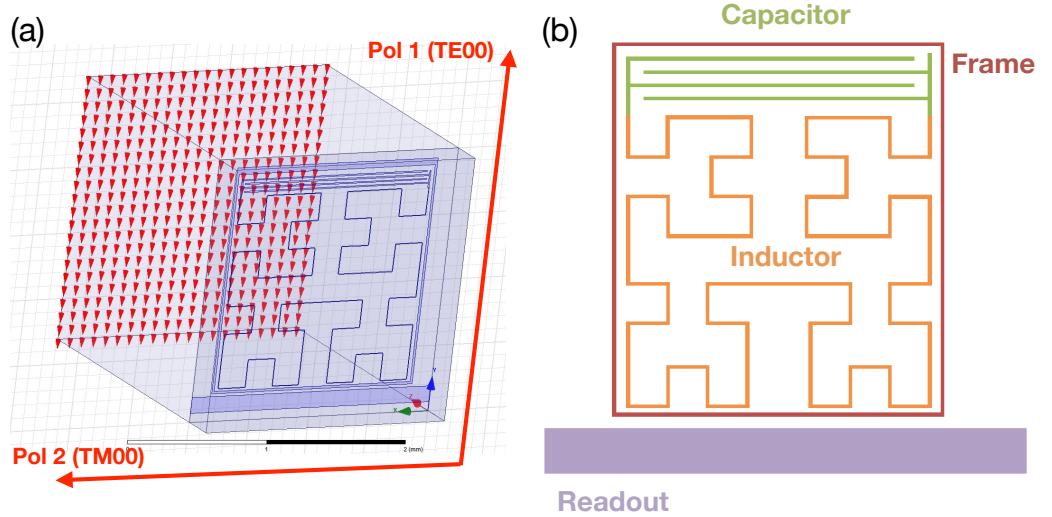


Figure 3.2: a) The exact structure of the simulation model in HFSS. The Master/Slave boundaries are used for two sidewalls. On the bottom and the backside of the substrate a Perfect E boundary is used. On top of the model a Floquet port is used to simulate plane wave with 18 modes. Two polarizations (TE_{00} and TM_{00}) are stimulated as the incident signal. The arrows show the direction of the electric field in the two dominant modes. b) A single pixel in simulation is separated into four components, the inductor capacitor, frame and readout line. The absorption efficiency of each component is estimated individually.

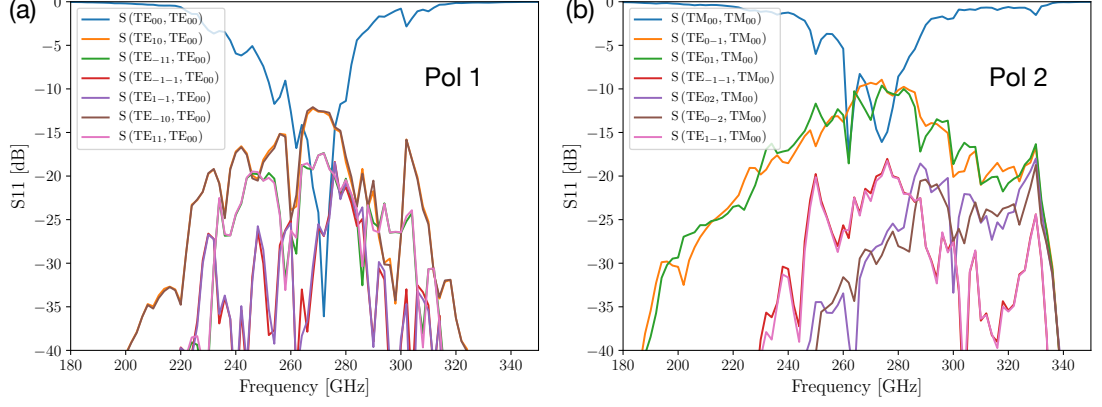


Figure 3.3: a) S-parameter results for a TE₀₀ excitation (Pol 1). Only the modes with a maximum return loss higher than -20 dB are plotted for clarity (same for (b)). The TE₁₀ and TE₋₁₀ modes have more reflect energy than other higher modes. b) S-parameter results for a TM₀₀ excitation (Pol 2). TE₀₋₁ and TE₀₁ modes reflect more energy than other higher modes.

3.4 Simulation and measurement of LEKID array

3.4.1 Absorption of NIKA2 1mm array

In this section, the surfaces of all components of pixel are assigned with an impedance boundary in the simulation. The simulated S-parameters are shown in Fig. 3.3(b) and (c) for incident polarization 1 and 2, respectively. For the clarity of the discussion, only the modes with maximum values larger than -20 dB are considered and plotted.

From the S11 of the dominant mode, the band center is -36 dB at 272 GHz and -17.5 dB at 274 GHz for Pol 1 and Pol 2, respectively. Compared with the design central frequency 260 GHz, there is a 12 GHz difference. In Fig. 3.4 the dashed curves show the total absorption in the pixel, as calculated from Eqn. 3.6. It has a maximum at 262 GHz for both polarizations, which is consistent with the design. This analysis shows that actually a non-negligible part of the energy is reflected into higher modes, which are not considered in earlier studies [74].

The two dominant reflected higher modes are TE₁₀ and TE₋₁₀ for Pol 1 and TE₀₋₁ and TE₀₁ for Pol 2. The maximum reflection of all higher modes together is 15.1% and 27.2% for Pol 1 and Pol 2, respectively. The average reflection in band from 230 GHz to 290 GHz of all higher modes is 6.3% and 13.0% for Pol 1 and Pol 2, respectively. A

large portion of the reflected higher modes is due to the reflected energy by impedance mismatch, 35.3% at peak calculated using Eqn. 3.5. We also find that the electric field distributions of these higher modes for both polarizations are consistent with the geometry of the Hilbert curve. This suggests that part of the higher modes is caused by the non-uniformity of the inductor geometry. Compared to the wavelength 1.15 mm, the segment length of 240 μm is quite large ($\approx \lambda/5$). Ideally the typical geometry should be much smaller than the wavelength to be treated as a uniform sheet ($< \lambda/10$) [71]. However, decreasing the segment length will also decrease the inductor width, resulting in a decrease of array yield and uniformity. For example, if we increase the third-order Hilbert inductor to a fourth order, the inductor width will be around 1 μm , and the total length of the inductor will be 27 cm. To fabricate such long and narrow line is a challenge for the yield of fabrication. Also, this might cause distributed resonating modes coming into the band of interest.

Using the surface loss method mentioned in Sec. 3.3.2, the absorption efficiency of the individual components are calculated. Fig. 3.2(b) shows the definition of the four different components. The absorption efficiency calculated from S11 of all modes is consistent with the sum of the surface losses of all components (Fig. 3.4). The maximum difference is 1.0% and 2.3% for Pol 1 and Pol 2, respectively. These small differences could be caused by numerical calculation error and by small overlaps of the surfaces of connections.

The average absorption of all components in the frequency band from 230 GHz to 290 GHz is 73.1% and 50.5% for Pol 1 and Pol 2, respectively. The average in band absorption of the inductor is 61.7% and 41.2% for Pol 1 and Pol 2, respectively. There is about 10% of the energy absorbed by other components than the inductor, for both polarizations. Compared with the calculation using Eqn. 3.5, the inductor absorbs 10% more energy for Pol 1 and 10% less energy for Pol 2. This 20% difference of the absorption efficiency in two polarizations was not expected from the transmission line model (Eqn. 3.5), and is mainly caused by the readout line and the frame, as we will show in Sec. 3.5.1. The simulated absorption efficiencies are summarized in Table 3.1.

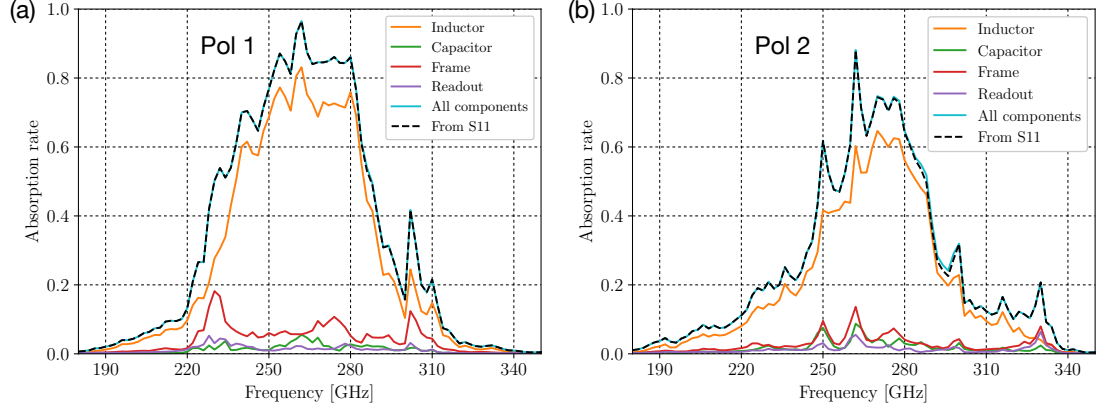


Figure 3.4: a) Absorption efficiency of each component and the sum of all components for Pol 1. The absorption efficiency calculated from S-parameter is consistent with the one calculated from the surface loss (same for (b)). b) Absorption efficiency of each component and the sum of all components for Pol 2.

3.4.2 FTS measurements

We compare the results of our simulations to measurements performed on the detector arrays fabricated for the NIKA2 project [76]. To measure the optical response, two arrays are cooled down at 150 mK in the NIKA2 cryostat. A polarizer is placed in front of two arrays to separate two polarizations, Pol 1 and Pol 2. The orientation of the two polarizations with respect to the array are shown in Fig. 3.2(a). The optical passband is defined by a 10.15 cm^{-1} (304 GHz) low-pass filter and a 6.55 cm^{-1} (196 GHz) high-pass filter¹, shown in Fig. 3.5. The detailed optical setup is introduced in [27].

The spectral response of the arrays has been characterized using a Fourier Transform Spectrometer (FTS) based on a Martin-Puplett Interferometer [77] (see Appendix B). The FTS uses two blackbody sources, at 77 K and 300 K respectively. The LEKID responses are measured using the NIKEL readout system [28]. The raw data is the response of each LEKID versus the position of the moving mirror. Using a Fourier transform, the position is converted to frequency.

We measured one readout line of pixels for each array. 86 and 112 pixels are

¹ Both filters are from Cardiff University

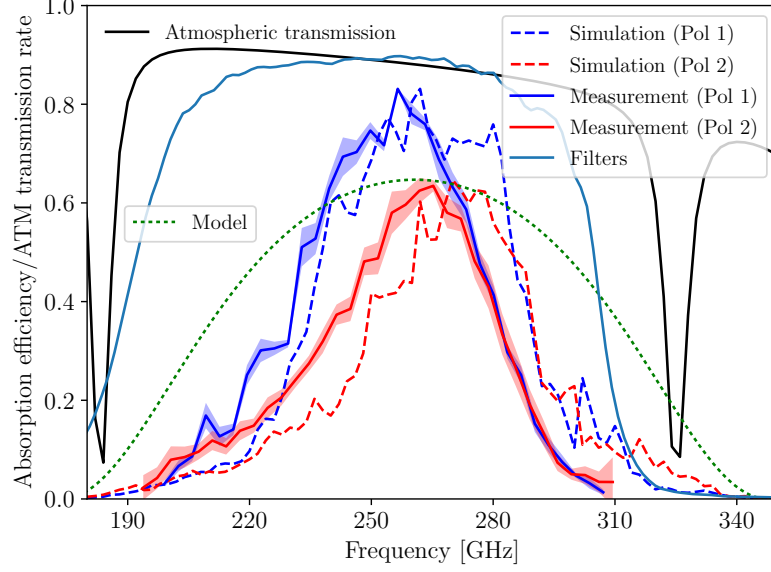


Figure 3.5: Simulated absorption efficiency of the inductor for both polarizations (dashed curves) and mean (solid line) and standard deviation (shadow) of the FTS measured responses of the KIDs. The responses are normalized to the maximum of the simulation. The passband of the optical system is defined by a low-pass filter and a high-pass filter together. The green dotted line is calculated from Eqn. 3.5, using $Z_{\text{KID}} = 96 \Omega$. The atmospheric transmission is calculated using a simplified model with precipitable water vapor of 1 mm.

analyzed for Pol 1 and Pol 2, respectively. For this measurement, the maximum displacement of the mirror from the Zero Path Difference position (ZPD) is 22 mm, resulting in a 3.4 GHz frequency resolution. To account for the different blackbody powers emitted by the sources at different frequencies, the results are rescaled applying a $1/\nu^2$ factor, derived from the Rayleigh-Jeans limit for constant optical throughput versus frequency. The results are then calibrated using the transmission spectra of the two band-defining filters. For simplicity, the data is normalized to the peak of the simulated absorption efficiency of the inductor for each polarization. Finally the mean and standard deviation are plotted in Fig. 3.5.

To make discussion simple, we directly compare the simulated absorption of the inductor to the FTS measured responses of LEKIDs. We assume that the different lengths of the capacitor fingers in the different pixels have no influence on the absorption efficiency, since the finger length is much smaller than the wavelength and the

Table 3.1: Absorption efficiency of the NIKA2 1mm arrays

Averaged from 230 GHz to 290 GHz	Pol 1	Pol 2
AE_{SL} of all components together	73.1%	50.5%
AE_{SL} of other components than the inductor	10.9%	9.3%
AE_{SL} of the inductor	61.7%	41.2%
Transmission line model (Eqn. 3.5)	61.5%	
FTS measurement (220 GHz to 280 GHz)	60.0%	42.2%

capacitor is not sensitive to the radiation. From the FTS measurements presented in Fig. 3.5, we could also conclude that the finger lengths have no obvious influence on the optical response. The quasi-particles generated in the capacitor could change the capacitance or diffuse into the inductor. However, these changes are negligible and we therefore assume that the energy absorbed by other parts than the inductor has no effect on the response of the pixels.

As shown in Fig. 3.5, the simulation matches well with the measurement, except for a small offset for both polarizations. This 10 GHz offset between the measurement and simulation can be explained by the measured 260 μm thickness of backshort for both arrays, instead of the 250 μm used in the simulation. The substrates are commercial products with a specification of $\pm 10 \mu\text{m}$. We calculated the average measured response from 220 GHz to 280 GHz (Table 3.1) and it matches well with the absorption efficiency of the inductor, discussed in Sec. 3.4.1. Using Eqn. 3.5, the calculated absorption from the simple model gives a similar maximum as mentioned for Pol 2, but overestimates the total in-band absorption efficiency. The small standard deviations of the measurement show that all pixels have a similar optical response.

3.5 Further analysis

3.5.1 Absorption efficiency by different components

To understand the results discussed in Fig. 3.4, we performed simulations for four configurations by removing individual components of the pixel while keeping every-

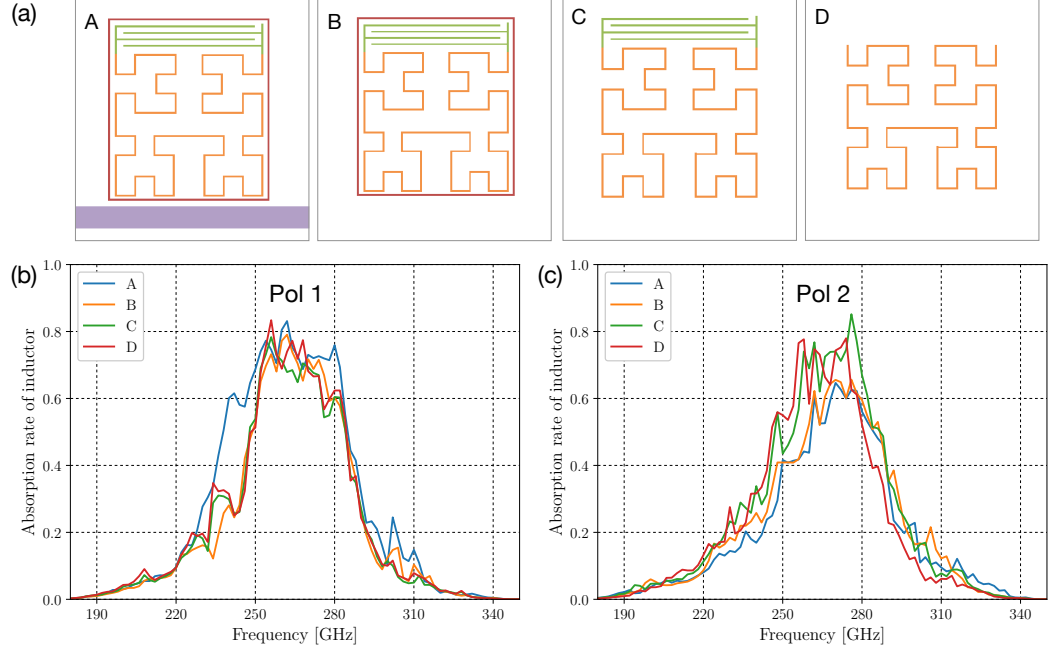


Figure 3.6: a) The four simulation configurations investigated in (b) and (c). b) Absorption efficiency of the inductor, with incident polarization Pol 1. c) Absorption efficiency of the inductor, with incident polarization Pol 2.

thing else the same. Fig. 3.6(a) shows how the readout line, frame and capacitor are removed step by step in the simulation models. The average in band absorption efficiency of the inductor only decreases 10% from A to B by removing the readout line for Pol 1. For Pol 2, the absorption efficiency increases 3% from A to B. This indicates that the readout line focuses the electric field to the inductor, when the directions of the readout line and E-field are perpendicular to each other. When the directions are parallel, it reflects a small part of energy, like a metal mesh polarizer.

From B to C, removing the frame does not change the absorption efficiency for Pol 1, but does increase it for Pol 2 by 9%. Also the energy reflected to the higher modes are decreased by 6%. This suggests that the frame, used to decrease the cross talk, give rises to an increase of generation of higher modes for Pol 2. The increased absorption of the inductor in B comes from the absorbed and reflected energy of the frame in C.

From C to D, the capacitor increases the absorption of Pol 1 by 2% and decreases

that of Pol 2 by 2%. Therefore, our compact capacitor design does not change the absorption efficiency significantly. For both C and D, the absorption efficiency for Pol 1 and Pol 2 are approximately the same, about 51%. This is consistent with the assumption that the Hilbert curve has similar sensitivity for dual polarizations.

3.5.2 Absorption efficiency with different materials

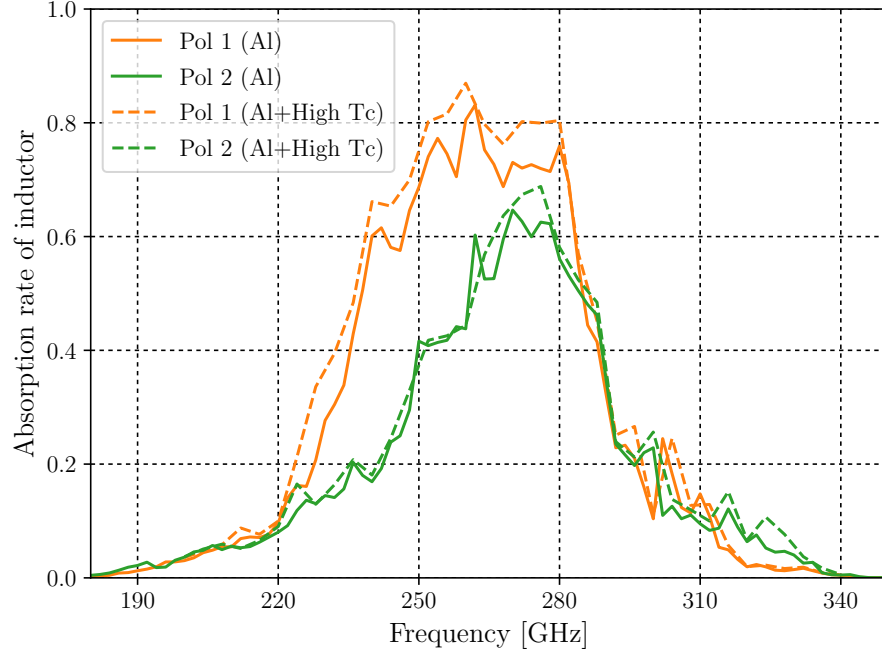


Figure 3.7: Absorption efficiency of inductor with two configurations for two polarizations. All surfaces of components are assigned as impedance boundaries (Al) in one configuration. In another configuration, the surfaces of the readout line and frame are assigned as PEC to mimic high- T_c material.

In Sec. 3.5.1, we have noticed that 10% of the energy is absorbed by other components than the inductor. To increase the absorption efficiency of the inductor, lossless materials, such as Nb, NbN, and NbTiN, could be used for the readout line and the frame. These materials have a high transition temperature corresponding to a high gap frequency (73 GHz/K). When the critical temperature T_c of the superconductor is higher than 4.5 K, it can be considered as a PEC in our frequency range.

In the simulation, the surfaces of the readout line and frame are assigned as PEC

while the inductor and the capacitor are still with the impedance boundary used before. It would also be possible to use a high- T_c material for the capacitor, but the connection of the inductor and capacitor could be a problem during fabrication. Using high- T_c material, the average absorption efficiency in band is increased by 7.4% and 2.6% for Pol 1 and Pol 2, respectively, shown in Fig.3.7. These increases are consistent with the absorption efficiency of the readout line and frame, shown in Fig. 3.4. We also simulated changing the readout line to high- T_c material only. The results have no larger than 2% difference compared with all-Al model. This is consistent with the prediction that the sheet impedance of the wide readout line is much smaller than Z_0 , so that it behaves as a PEC.

3.5.3 Absorption efficiency with different pitch sizes

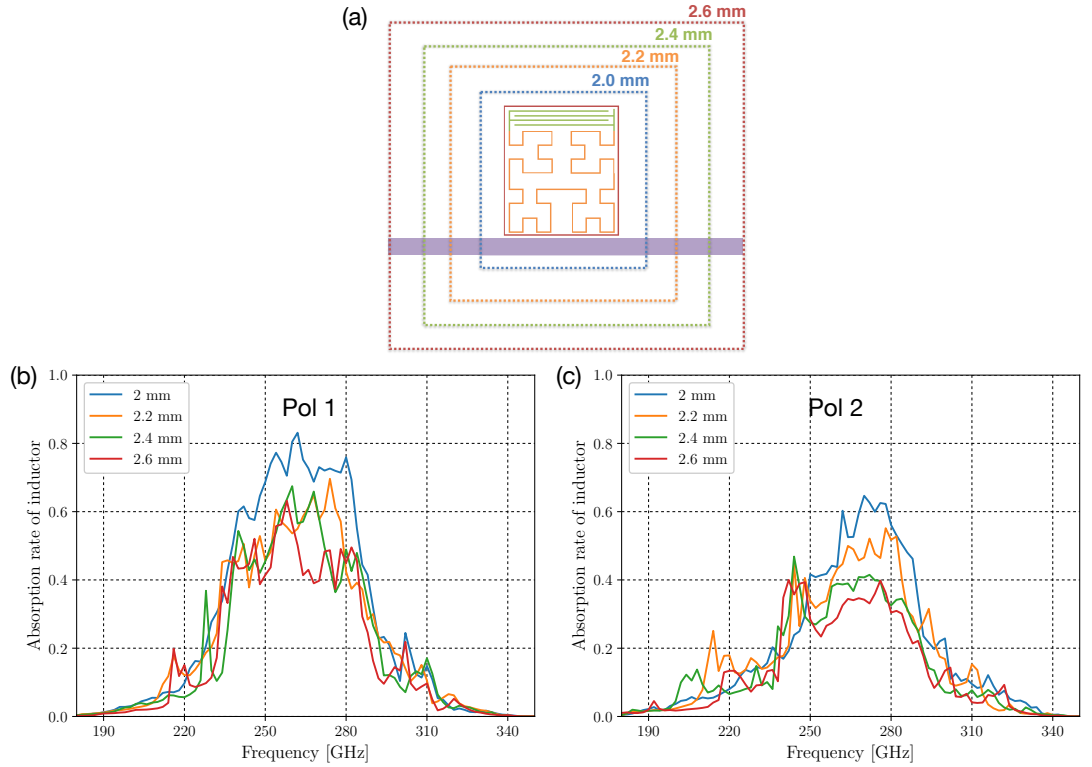


Figure 3.8: a) The dashed boxes present the pitch size in the simulation. b) Simulated absorption efficiency of inductor by changing pitch size for Pol 1. c) Same as (b) but for Pol 2.

Pitch size is one of the key parameters for filled array. It determines the number of pixels on focal plane and also the total observation efficiency. In our case, the absorbing area is considered as the inductor size, $1.5 \times 1.6 \text{ mm}^2$. With 2 mm pitch size, the filling factor $F = (1.5 \times 1.6)/2^2 = 0.6$. This results in a dilution factor, so that if the inductor is able to absorb $\eta_L = 100\%$ of the incident radiation, we expect our simulation to show an absorption efficiency of $\eta_{tot} = F\eta_L = 60\%$, from Eqn. 3.1 assuming $\eta_{opt}\eta_{qp} = 1$. To vary this, and to check the effect of the filling factor of the inductor area, we simulated this NIKA2 design with 4 different pitch sizes, shown in Fig. 3.8 (a). All components except the readout line are same for all models. The readout line is automatically extended to the boundaries to have a reasonable readout line design. For each model the calculated filling factors are listed in Table 3.2. The $\eta_L = \eta_{tot}/F$ is calculated for each pitch, listed in Table 3.2. For Pol 1, the inductor efficiency η_L is about 100% with 2 mm and 2.2 mm pitch sizes.

Table 3.2: Averaged absorption efficiency of the inductor

Pitch size	Filling factor	Pol 1		Pol 2	
		η_{tot}	η_L	η_{tot}	η_L
2.0 mm	0.60	62%	103%	41%	69%
2.2 mm	0.50	48%	97%	36%	72%
2.4 mm	0.42	45%	107%	31%	74%
2.6 mm	0.36	42%	118%	28%	80%

For Pol 1, when the pitch size keeps increasing, the η_L is much larger than 100%. Since the absorption efficiency itself cannot be larger than 100%, this suggests the filling factor is underestimated and the effective area is larger than the physical size of the inductor. Since η_L is calculated by averaging all points from 230 GHz to 290 GHz, the effective area may vary with frequency. For Pol 1 with 2 mm pitch size, the filling factor is 0.6 and we have $\eta_L > 100\%$ at the frequencies where $\eta_{tot} > 0.6$, giving the effective area larger than F . When $\eta_{tot} < 0.6$, it is hard to evaluate the size of the effective area since η_L is also unknown. We may assume the effective area is the physical size of the inductor and then $\eta_{tot} = \eta_L$. In the simulations, the periodic

boundaries are used, so the wave might be reflected by the resonator structure, go through the periodic boundary, re-enter from the other side and be absorbed by the resonator. This absorbed energy is a crosstalk and should not be counted in the η_{tot} . Estimation of this crosstalk in simulation is quite hard, but we could evaluate it from the measured beam profile. In Section 4.6, the measurements show that this reflected energy is below -15 dB (3.2%). Therefore, we still can conclude that for Pol 1 the absorption efficiency of the inductor is close to 100%.

For Pol 2, the η_{tot} follows the change of filling factor. The η_L is about 70% not as good as the 100% for Pol 1. This difference is due to the frame and the readout line, as discussed in Section 3.5.1. The η_L also increases as pitch size increases. The increase in η_L might be caused by the reflection due to the periodic readout line. The direction of the readout line is parallel to the incident polarization (Pol 2), so they may behave as wire grids reflecting energy. As pitch size increases, the distance between readout line is increased and the reflected energy is decreased. This could also explain why the Pol 1 is not affected by this effect.

3.6 Conclusions

In conclusion, we have presented a detailed analysis of the optical performance of lumped-element kinetic-inductance detector arrays, using the NIKA2 1mm array as a test case. Our analysis shows that whereas a transmission line model gives a reasonable estimate of the absorption at the frequency band center, it overestimates the band-integrated optical absorption. For a Hilbert-type pixel, numerical simulations using HFSS show a significant difference in the absorption efficiency for the two polarizations, due to the anisotropic scattering off the readout line, and stress the importance of scattering to higher-order reflection modes. The detailed frequency response is validated by FTS measurements performed on the actual NIKA2 detector arrays. A detailed analysis of the absorption in different elements of the pixels show that most radiation is absorbed in the sensitive inductor part, but an improvement of 7% can still be made by changing the frame of the pixel to a non-absorbing (high- T_c)

material. Also we find that for Pol 1, the absorption efficiency of the 3rd-order Hilbert inductor is close to 100 % and the effective area is larger than the physical size of the inductor. Further improvements can be made by increasing the sheet impedance of the inductor line by decreasing the linewidth or the filling factor. Finally, by changing the geometry to a $\lambda/4$ back short, the frequency bandwidth can be doubled. This way, a detector array that is fully optimized for continuum detection in the 1mm atmospheric window comes into reach.

Chapter 4

High angular resolution LEKID

4.1 Introduction

The resolution of a detector is determined by the size of the effective beam resulting from the convolution of the diffraction pattern, created by the instrument optics, with the pixel transfer function [79]. In millimeter wavelengths, the detectors can be separated, according to optical behavior, into antenna-coupled (single mode) detectors and filled-array (multimode) detectors. For antenna-coupled detectors, the optical behavior is determined by the beam pattern of the antenna, such as horn and planar antennas. The beam pattern can be calculated using electromagnetic simulation software. Single mode antenna follows the antenna theorem, which states that

$$A_e \Omega_a = \lambda^2 \quad (4.1)$$

where A_e is the effective area of aperture and Ω_a is the antenna solid angle. Given this theorem, increasing the antenna aperture gives smaller antenna solid angle, corresponding to a higher angular resolution.

In contrast, a filled array, made up of radiation absorbers, is sensitive to all light

This chapter is partially published as Shu, S., Calvo, M., Leclercq, S., Goupy, J., Monfardini, A. and Driessen, E.F.C., 2018. Prototype high angular resolution LEKIDs for NIKA2. *Journal of Low Temperature Physics*, 193(3-4), pp.141-148.[78]

from 2π steradians, but only if the impedance is matched. The antenna theorem is invalid for filled-array detectors, where the resolution increases with the effective area decreasing. In our case, since the inductors of LEKIDs are designed to match the free space impedance ($377\ \Omega$) acting as absorber, the calculation of the angular resolution is introduced in the following section.

4.2 Angular resolution of filled array

In this section, we present the calculation of one-dimension resolution. The diffraction pattern of a telescope with ideal circular aperture (without obscuration) is described by the Airy disk:

$$A(\theta) = \left(\frac{2J_1(ka \sin \theta)}{ka \sin \theta}\right)^2 = \left(\frac{2J_1(x)}{x}\right)^2, \quad (4.2)$$

where J_1 is the Bessel function of the first kind order one, $k = 2\pi/\lambda$ is the wavenumber, a is the radius of the aperture and θ , the angle of observation. Using the small angle approximation $\sin \theta \approx \tan \theta$, we have $\sin \theta \approx r/f$, where f is the focal length and r is the radial distance from the optics axis in the focal plane. Then we substitute the angle θ with r and have

$$x = ka \sin \theta = \frac{2\pi a}{\lambda} \frac{r}{f} = \frac{\pi D}{f\lambda} r = \frac{\pi r}{F\lambda}, \quad (4.3)$$

where $D = 2a$ is the diameter of the aperture and $F = f/D$ is the f-number. To simplify our discussion, we normalize the position r to the constant value $F\lambda$.

The detector response is considered as a rectangular function:

$$P(r) = \begin{cases} 1, & \text{if } |r| \leq s/2 \\ 0, & \text{otherwise,} \end{cases} \quad (4.4)$$

where s is the pixel size and f is the focal length. The optical response $R(r)$ of a pixel is the convolution [79] of the telescope diffraction pattern $A(r)$ and the pixel

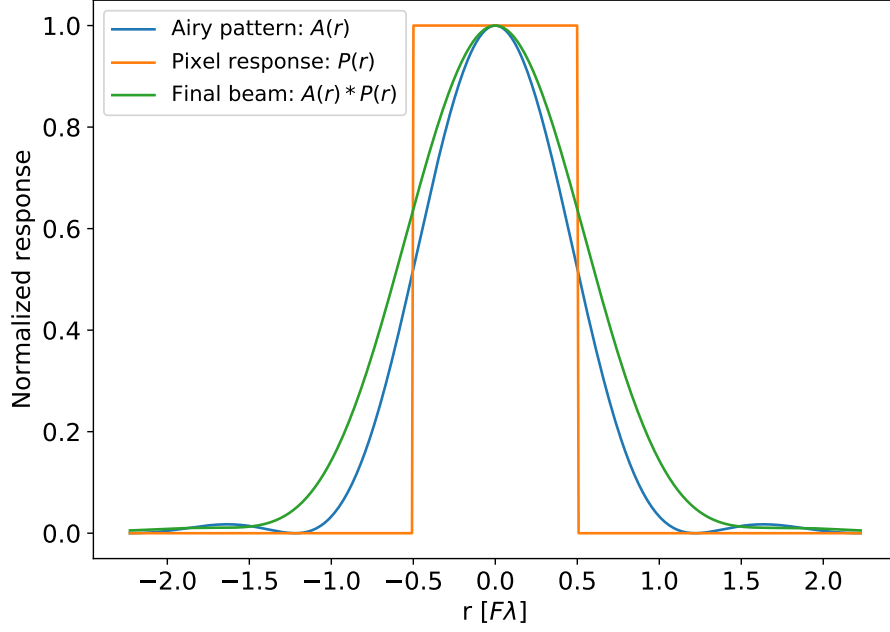


Figure 4.1: The final beam is the convolution of the diffraction pattern and the pixel response. For pixel size $1F\lambda$, the full-width half-maximum (FWHM) of the beam is increased by 21% from $1.029\lambda/D$ to $1.248\lambda/D$.

response function $P(r)$,

$$R(r) = A(r) * P(r). \quad (4.5)$$

After calculating $R(r)$, shown in Fig. 4.1, the angular resolution of a pixel is fitted with a Gaussian function. This suggests that we cannot reach but only approach the diffraction limit by decreasing the pixel size. Therefore, there are two ways to improve the resolution of a multi-mode pixel. One is to increase the $F\lambda$ by revising instrument optics; the other is to decrease the pixel size. Since λ is the observation wavelength, a constant in design, increasing $F\lambda$ results in a large f-number F which would need an increase of the focal plane size.

4.3 Angular resolution of NIKA2 instrument

The NIKA2 instrument has a diameter of $6.5'$ field-of-view on sky, corresponding to 80 mm diameter on focal plane. The equivalent focal length is calculated as

$$f = \frac{80 \text{ mm}/2}{\tan(6.5'/2)} \approx \frac{80 \text{ mm}}{6.5'},$$

using small-angle approximation $\tan \theta \approx \theta$. Unlike horned detectors for which the illumination of the primary mirror is apodized, filled arrays require the use of a cold pupil vignetting the edge of the primary mirror in order to minimize spill over from a warm background (diffraction on the mirror edge). For the current NIKA2 optics, the effective aperture size, 30 m, is decreased by the cold pupil to 27.5 m which gives $F\lambda = 1.77 \text{ mm}$. Taken this into account, the angular resolution of 1 mm wavelength pixel, shown in Fig. 4.2, is calculated using equations in Sec. 4.2. For this prototype design, we decrease the inductor size from 1.6 mm to 1 mm. With this small pixel design, theoretically a $9.4''$ FWHM angular resolution is expected, which is close to the diffraction limit $8.9''$ FWHM, as shown in Fig. 4.2. This resolution actually is calculated at the band center frequency of 260 GHz (1.15 mm wavelength) and the actually achieved resolution will be decreased by the long wavelength part in the band. Decreasing the pixel size also decreases the effective area if the pixel number is constant. To keep full focal plane coverage, a doubled number of pixels is necessary when decreasing the pitch distance from 2 mm to 1.4 mm.

4.4 Array Design

In this new pixel design we keep the order 3 Hilbert inductor design from the NIKA2 instrument [74]. The inductor width is scaled from $4 \mu\text{m}$ to $2.5 \mu\text{m}$ for keeping the same effective sheet impedance of the inductor part while decreasing inductor segment spacing. With the same film thickness, the inductor volume of the small pixels is 40 % of that of the big pixels. The Al film is assumed to be 20 nm thick with transition temperature $T_c = 1.4 \text{ K}$, sheet inductance $L_s = 2 \text{ pH}/\square$, and sheet resistance

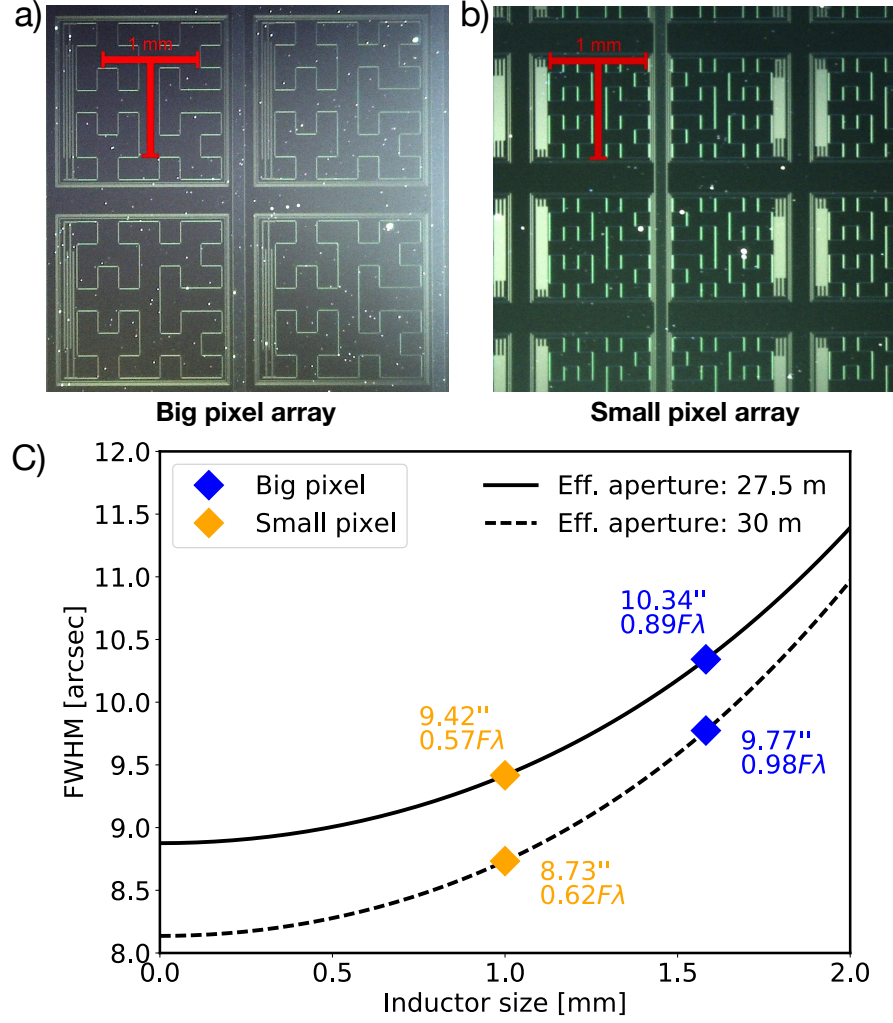


Figure 4.2: (a) and (b) are microscopic images of the current NIKA2 260 GHz design and our small pixel design. The red bars indicate 1 mm. (c) shows the calculated resolution as a function of inductor size, for 27.5 m (unvignetted part of the primary mirror defined by the cold pupil) and 30 m (full illumination of the primary mirror) effective telescope apertures.

$R_s = 1.6 \Omega/\square$. For the Hilbert curve, we have 63 line segments with $145 \mu\text{m}$ length. The interdigital capacitors are designed based on the readout 500 MHz bandwidth and the final resonances are tuned from 2.121 GHz to 2.621 GHz with simulations in Sonnet [80, 81]. The coupling quality factor Q_c to the $120 \mu\text{m}$ width microstrip feedline is designed from 1.3×10^4 to 1.6×10^4 to match the internal quality factor under typical background illumination at the IRAM 30-m telescope.

The focal plane layout of bare LEKIDs is mainly limited by the microwave crosstalk caused by the electromagnetic coupling between nearby resonances [82]. This crosstalk is quantified as the difference between single LEKID resonance frequency and the resonance frequency of the same LEKID simulated together with another LEKID in a specific configuration shown in Fig. 4.3. Three highest crosstalk configurations are simulated to find a most compact layout for this small pixel. Beyond a knee of 20 kHz shift of the intrinsic resonances the crosstalk becomes significant and increases extremely fast with decreasing distance between neighbouring pixels. As seen in our simulation (Fig. 4.3), to get as close as possible to this knee, the pitch between pixels along readout line Dx is set to 1.4 mm and pitch between two readout lines $2 \times \text{Dy}$ is set to $2 \times 1.4 \text{ mm}$. To decrease the effective surface occupied by the readout line, pixels are placed on both sides of the feedline, in contrast with the pixel design currently deployed in NIKA2. This design causes the crosstalk to become significant when the two resonances are too close to each other either in frequency or spatially. To minimize this crosstalk, we tune the frequency difference of two opposite pixels to the maximum frequency separation, 250 MHz for 500 MHz readout bandwidth. This decreases the crosstalk, which is caused the mutual capacitance, to a constant 35 kHz offset for both resonances.

4.5 Optical measurements

A sky simulator and cold optics setup with $F = 1.48$ are used to characterize the angular resolutions of both designs, shown in Fig. 4.4. The sky simulator consists of a high temperature point-like source mounted in front of a low temperature background

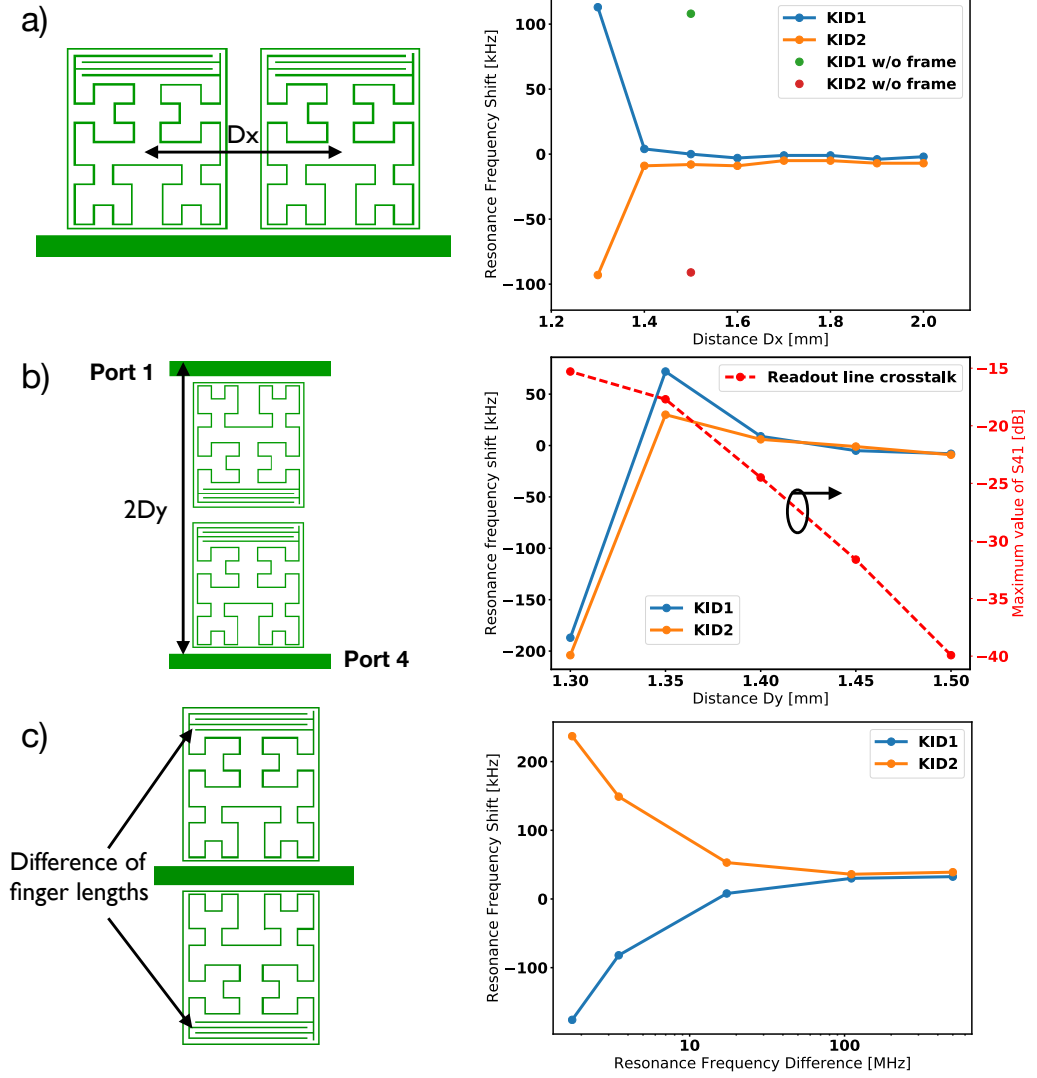


Figure 4.3: Simulated crosstalk in three different configurations. (a) shows the crosstalk with different horizontal pitch distance D_x . Two single *solid symbols* show the crosstalk without the frame outside the LEKID. (b) shows the crosstalk with different vertical pitch distance D_y and the maximum transmitted energy between two readout line. (c) shows the crosstalk with different resonance frequency by changing the capacitor finger length.

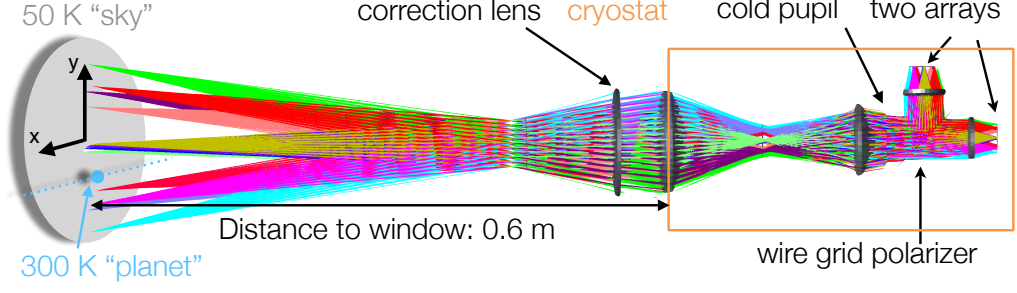


Figure 4.4: Optical setup of the measurement system. The sky simulator is located 0.6 m away from the cryostat window and the planet is scanned in the plane parallel to this window. Inside the cryostat two arrays are mounted on the 70 mK stage. The incident signal is split by a wire grid polarizer, and both arrays are oriented identically with respect to the incident polarization. With this setup, the image size of the planet on the two arrays is the same as the image size of a point source on the focal plane of NIKA2 at the IRAM 30-m telescope.

plate. The point-like source is a 4 mm diameter metal ball (planet) at 300 K, which is mounted with a transparent thin nylon line. The planet is placed at a distance of 60 cm to the entrance window of the test cryostat containing the optics and the detectors, and a 50 K blackbody, cooled down by a pulse tube cryocooler, is behind the planet acting as a sky background [74]. The two detector arrays are mounted on the 70 mK stage of the cryostat (which uses a ^3He - ^4He dilution refrigerator), in the focal plane of the optics after a polarizer, which allows us to measure both arrays simultaneously, and reduces measurement errors induced by the setup. The 260 GHz band is defined by a 10.15 cm^{-1} low pass filter and a 5.65 cm^{-1} high pass filter¹ and the incident polarization directions are parallel to the capacitor fingers for both arrays. With this setup, the image size of the planet on focal plane is the same as the image size of a point source on the 30-m telescope focal plane.

During the measurements, an x-y table moves the planet along the y-axis, as shown in Fig. 4.4, to perform a single scan. By changing the x-position of the planet after each scan, a complete mapping of the arrays is performed. The frequency responses of LEKIDs are measured with a NIKEL readout system [28], which is also used in the NIKA2 instrument.

¹ Both filters are from Cardiff University

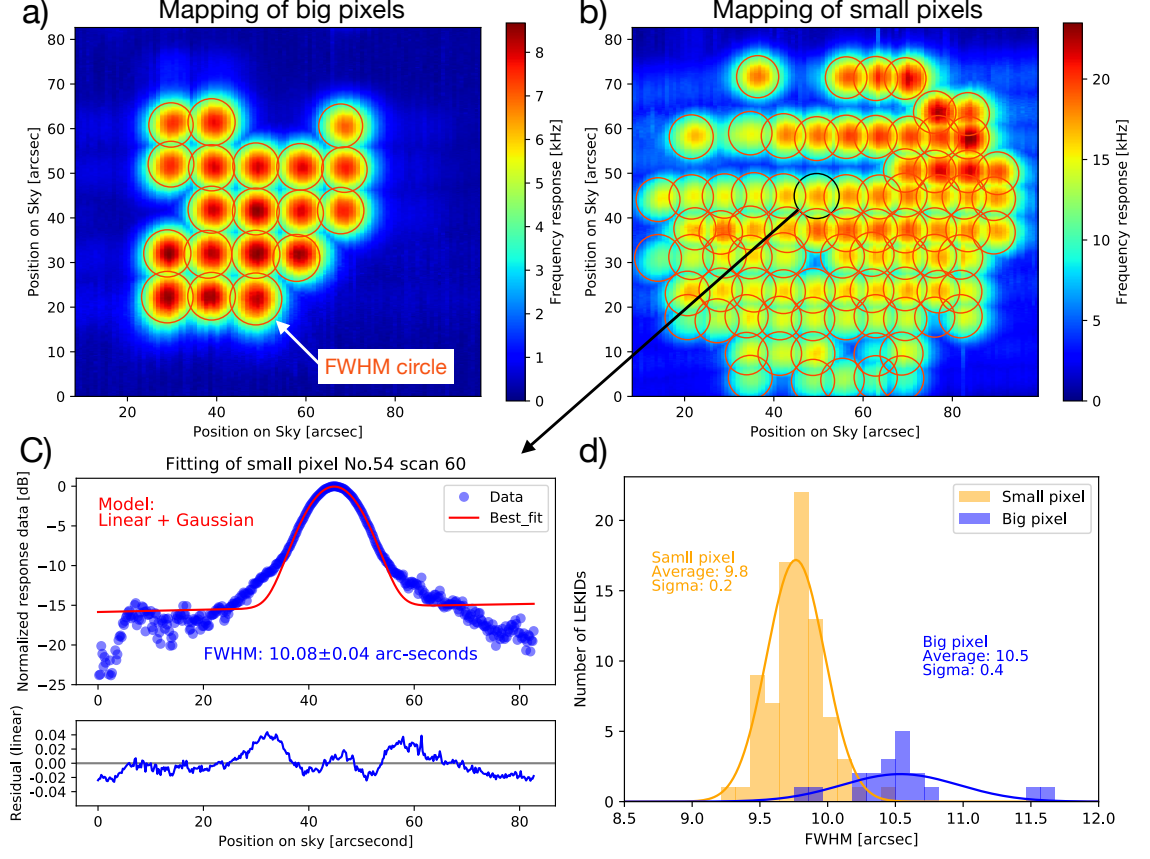


Figure 4.5: Optical measurement results of the two designs. (a) and (b) show the mappings of two arrays. The *red* circles indicate the FWHM of the different pixels. (c) shows the fitting of one small pixel indicated by the *black* FWHM circle. The data shown is a scan in vertical direction, passing through the peak response and normalized to the maximum. (d) shows the histogram of resolutions for two arrays with Gaussian fit.

4.6 Results and Discussion

Two array mappings, shown in Fig. 4.5, are generated by combining all pixel responses together. The big pixel array has 25 pixels in design, of which 19 are mapped. The missing pixels are caused by the overlap of two resonances. The small pixel array contains 112 pixels, of which 82 are mapped. This low yield for the small pixel array is mainly caused by the readout bandwidth of 500 MHz. Due to a slight overestimation of the film kinetic inductance, the actual frequency range of the array is 680 MHz instead of 500 MHz. The trimming process to relocate all resonances in the readout

bandwidth of 500 MHz is discussed in Chapter 5.

The coordinates of the planet in the sky simulator are transferred to an on-sky angle by measuring the observed distance between two adjacent pixels and using the focal-plane-to-sky factor of $4.875''/\text{mm}$ for NIKA2 at the 30-m telescope. This calibration is not perfect, but the ratio between the resolutions of the two arrays is not affected by eventual errors in this calculation.

We used a 1-D Gaussian to fit the individual images of the planet, as shown in Fig. 4.5. This fit yields an average resolution of $9.8 \pm 0.2''$ and $10.5 \pm 0.4''$ for the small and big pixels, respectively, as illustrated in the histogram in Fig. 4.5. The large spread in the big pixel resolution is attributed to the limited number of 19 samples, and several outliers attributed to stray light reflected from the sample holder. The found increase of resolution of a factor 1.08 ± 0.05 is consistent with the expected resolution increase of a factor 1.10. With the factor 1.08, we expect to achieve a resolution on sky of $10.2''$ compared to the current value of $10.9''$.

Table 4.1: Characterization of the two arrays

	Big pixel	Small pixel
Inductor size [mm^2]	1.6×1.5	1.0×1.0
Inductor volume [μm^3]	1149	449
Pitch [mm^2]	2.0×2.0	1.4×1.4
Resolution in-lab	$10.5 \pm 0.4''$	$9.8 \pm 0.2''$
Resolution on-sky	$10.9''$ [27]	$10.2''$ (expected)
Responsivity [kHz]	106 ± 6	202 ± 32

In Fig. 4.5, the nylon line, a point source, is transparent for big pixel design but our small pixels are quite sensitive to it, because of the 60 % decrease in inductor volume. The final responsivity, shown in Table 4.1 is extracted by the amplitude of the Gaussian fit showing the intensity of each response of the planet. The relative

responsivity could be estimated with equation

$$Responsivity \propto \frac{\alpha Q}{V}, \quad (4.6)$$

where α is the kinetic inductance ratio, Q is the loaded quality factor and V is the inductor volume [69]. In our case, the inductor volumes are $449 \mu\text{m}^3$ and $1149 \mu\text{m}^3$ and the loaded quality factors are about 8400 and 12500 for small and large pixel, respectively. Assuming the same kinetic inductance ratio, a factor of 1.7 is derived compared to the observed factor 2. The responsivities of pixels have a 25 % non-uniformity on both arrays, which are caused by the uniformity of the inductor width. This non-uniformity changes the volume and sheet impedance of the inductor and the optical response is changed as the result [83]. For both measured arrays, there is no obvious difference in noise spectrum at frequencies above 1 Hz from in-lab measurement, suggesting an improvement by a factor 2 of sensitivity using the new pixel design. When the array is installed on the telescope and the noise is dominated by the photon noise [84], then the sensitivity will keep the same.

4.7 Conclusion

Table 4.1 summarizes the results obtained in this study. We have successfully designed and characterized a compact pixel prototype for the 260 GHz band of the NIKA2 instrument, that is expected to decrease the on-sky resolution from the actual $10.9''$ to $10.2''$, while doubling the expected responsivity. This design can be used to fill the complete $6.5'$ field of view of the NIKA2 camera once the bandwidth of the readout electronics is increased as planned.

Chapter 5

Increased multiplexing of LEKID arrays by trimming the capacitors

5.1 Introduction

The ability of frequency multiplexing readout is one intrinsic advantage of MKID. As the multiplexing density increases, the non-uniformity of frequency spacing causes crosstalk when two resonances have a frequency collision. Compared with the design frequency, the measured resonance frequency can shift by tens of MHz. Usually the bandwidth of a feedline is limited, for example to 500 MHz for the NIKA2 instrument [27], and the frequency spacing between adjacent resonators is designed to be several MHz. The minimal spacing is limited by the width of the resonance, which is determined by the quality factor Q . For ground-based millimeter-wave continuum detection, the Q is limited by the high sky background load and is around 8×10^3 for NIKA2. Since the measured resonance frequency has the same or even larger shift compared with the spacing, crosstalk caused by the frequency collisions happens frequently and decreases the number of functional pixels. For photon detection application, currently this is the main limitation on MKID array yield [26, 66]. Besides

This chapter is partially published as Shu, S., Calvo, M., Goupy, J., Leclercq, S., Catalano, A., Bidaud, A., Monfardini, A. and Driessen, E.F., 2018. Increased multiplexing of superconducting microresonator arrays by post-characterization adaptation of the on-chip capacitors. *Applied Physics Letters*, 113(8), p.082603.[83]

the intrinsic deviation, there is also another crosstalk caused by the transmission of the energy in the array when the array is illuminated [85]. In this chapter we focus on the crosstalk caused by the intrinsic resonance frequency deviation.

There are various factors causing the intrinsic resonance frequency deviation, such as variation in the film properties [86, 87], fabrication process inhomogeneities [88] and resonator design [82, 89]. For titanium-nitride films the sheet resistance, superconducting critical temperature (T_c) and capacitor etching depth [86, 88] are the dominant factors. For thin Al films usually the film thickness variation is the dominant factor [87], however, we find that for our test array the variation in the inductor width is dominant. To decrease the deviations, several methods have been previously explored [82, 86, 90]. By performing post-characterization adaption, we do not necessarily need to know the causes of the frequency deviation. Liu et al. [91, 92] have demonstrated a capacitor trimming technique to tune the resonance frequencies accurately. They have used a LED mapper, deployed on the same stage as the sample inside their cryostat, to find the physical resonators corresponding to the measured resonances [91]. This LED mapper should be fabricated depending on the number and design of the array and cannot be easily used for a different array. Also the linear relation of capacitance and IDC finger length cannot be extended to quasi-lumped element IDC, of which the capacitance depends on frequency. In this chapter, we present a capacitor trimming technique for quasi-lumped element KIDs using a beam mapping system. Compared with the LED mapper, the beam mapping measurement is a necessary characterization for photon detectors and no extra parts or wires are needed inside the cryostat. Also this mapping system is universal for all detector arrays without limitation on pixel number or design. We also demonstrate a method to tune quasi-lumped element IDC based on electromagnetic simulation. Using a NIKA2 test array, the comparison before and after trimming is discussed including the optical properties of the array.

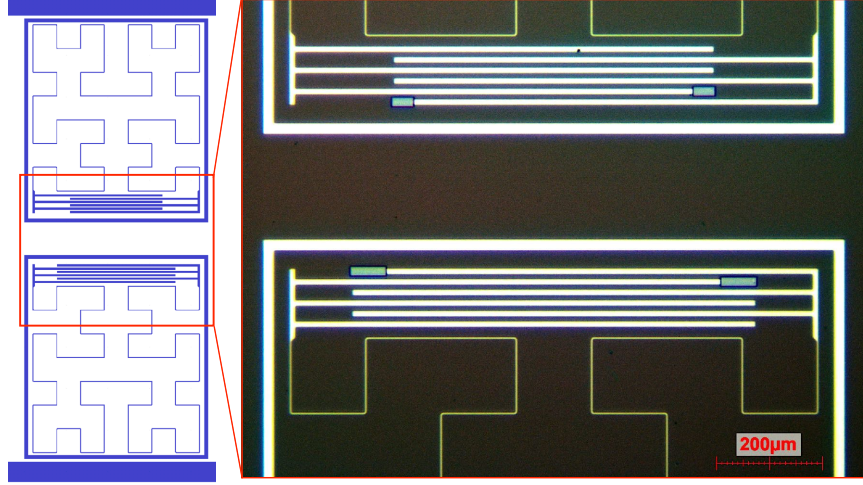


Figure 5.1: (Left) Schematic drawing of two MKID resonators. The resonance frequencies are tuned by the IDC finger lengths of different resonators. Inside a resonator all IDC fingers have the same length before trimming. (Right) The actual array covered with resist after the final etching step of the IDC trimming process. Only the outside pairs of IDC fingers were trimmed (less bright rectangles). The trimmed lengths are calculated based on the needed frequency shifts.

5.2 Characterization before trimming

5.2.1 Array design

We applied this technique on a prototype NIKA2 LEKID array, shown in Fig. 5.1, which was fabricated from a 21.6 nm thick Al film on a 250 μm thick, high-resistivity silicon substrate. There are 112 pixels on one feedline with pitch size of 1.4 mm. The design detail is discussed in Sec. 4.4. To get dual-polarization sensitivity the inductors are designed in a third-order Hilbert curve [74]. The capacitors are designed with 6 IDC fingers. The Al film properties are independently measured and give a thickness of 21.6 nm, a transition temperature of 1.46 K and a sheet resistance at 4.2 K of $1.14 \Omega/\square$. The sheet inductance of $1.09 \text{ pH}/\square$ is then estimated from Mattis-Bardeen theory [33, 34]. A 200 nm Al film was deposited on the backside of the wafer as a backshort to maximize the absorption in the 260 GHz band and serves, at the same time, as the ground plane of the microstrip readout line. With the measured

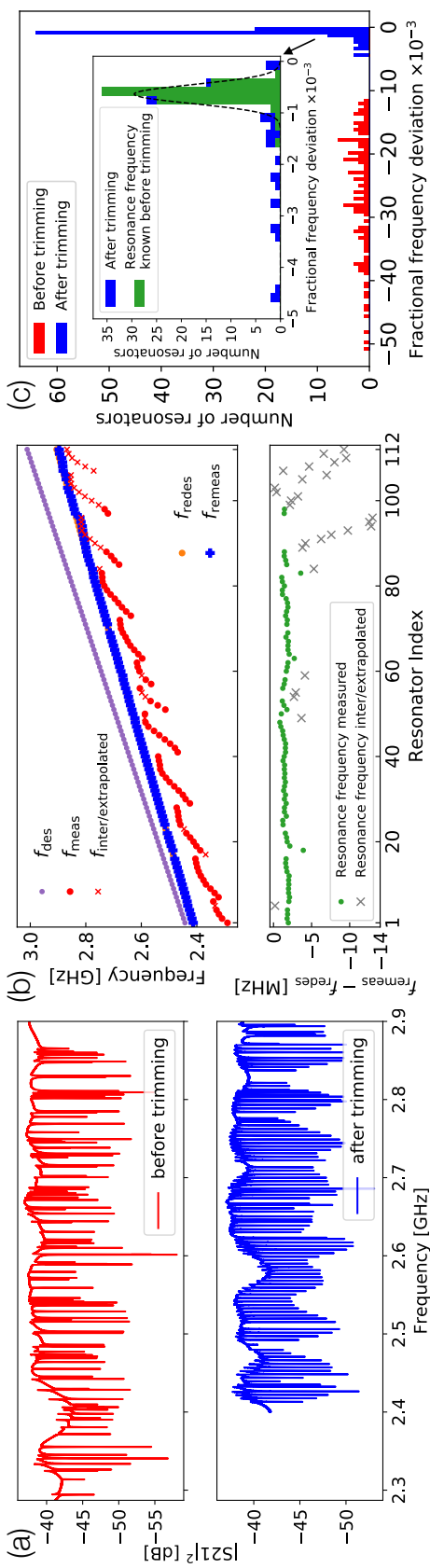


Figure 5.2: (a) Comparison of VNA measured feedline transmission S21 for the MKID array before (red) and after (blue) the trimming process. (b) Design (f_{des} , purple dot) and measured (f_{meas} , red dot) resonance frequencies before trimming, determined using the optical mapping system (upper panel). The resonance frequencies of unidentified resonators ($f_{inter/extrapolated}$, red cross) are inter/extrapolated based on the smooth variation of the frequency deviation (Fig. 5.3(a)). The re-designed resonance frequencies (f_{redes} , orange dot) for trimming and the re-measured resonance frequencies (f_{remeas} , blue dot) after trimming are plotted for comparison. The bottom panel shows the absolute frequency deviation between f_{remeas} and f_{redes} . The resonators with f_{meas} (green dots) have a mean value of 1.7 MHz and a standard deviation of 0.46 MHz. The resonators with $f_{inter/extrapolated}$ (gray crosses) show a larger deviation. (c) Histogram of the fractional resonance frequency deviation $\delta f/f$ before (red) and after (blue) the trimming process. After trimming the deviation is dramatically decreased, even for the inter/extrapolated resonators. In the inset, the green histogram shows the distribution of the resonators of which the exact frequency shift was known. The blue points show the resonators that were estimated using the inter/extrapolation described in the text. A Gaussian fit of the resonance frequencies of the identified resonators is plotted (dashed line), which gives a mean value of $\mu = -6.4 \times 10^{-4}$ and a standard deviation of $\sigma = 1.8 \times 10^{-4}$.

sheet inductance of $1.09 \text{ pH}/\square$, the resonance frequency range f_{des} is expected from 2.379 GHz to 2.941 GHz with 5.06 MHz frequency spacing. After the first fabrication the sample was cooled down to 80 mK in a ^3He - ^4He dilution refrigerator with an optical access. The transmitted optical band is defined by a 169 GHz high pass and 304 GHz low pass filters, but the detector is only sensitive in the range from 230 GHz to 270 GHz, as defined by the backshort distance.

In the first measurement, the feedline transmission S21, shown in Fig. 5.2(a), was measured using a vector network analyzer (VNA) with a mirror placed in front of the cryostat window, which gives an optical loading on the detectors equivalent to a 10 K black body. The measured resonance frequencies f_{meas} range from 2.289 GHz to 2.870 GHz and the central frequency is shifted by 80.5 MHz from the initial design f_{des} . This 3 % frequency deviation cannot be explained by the Al film thickness variation between 21.5 nm and 21.7 nm, which was independently measured by ellipsometry, and would correspond to a maximum 13 MHz deviation, nor by the resonator-to-resonator electrical crosstalk, which is estimated by simulation to be smaller than 20 kHz as discussed in Sec. 4.4.

5.2.2 Locating resonators using a beam mapper

The resonance frequencies are linked to the physical resonators using a beam mapping system presented in Sec. 4.5. The feedline transmission and the optical performances of the MKIDs are measured in the same cool-down. The beam mapping system consists of a movable 300 K small metal ball in front of a 50 K cold background. The responses of the MKIDs and the position of the metal ball are read out by the NIKEL system [28]. By pinning out the position of the maximum of the response of each MKID, the resonance frequencies are mapped to the physical position of the resonators. In this single measurement, only 79 out of 112 resonances were identified with physical resonators, because of the 500 MHz readout bandwidth limitation and crosstalk. We observed a smooth variation of the normalized fractional frequency deviation over the surface of the array (Fig. 5.3(a)).

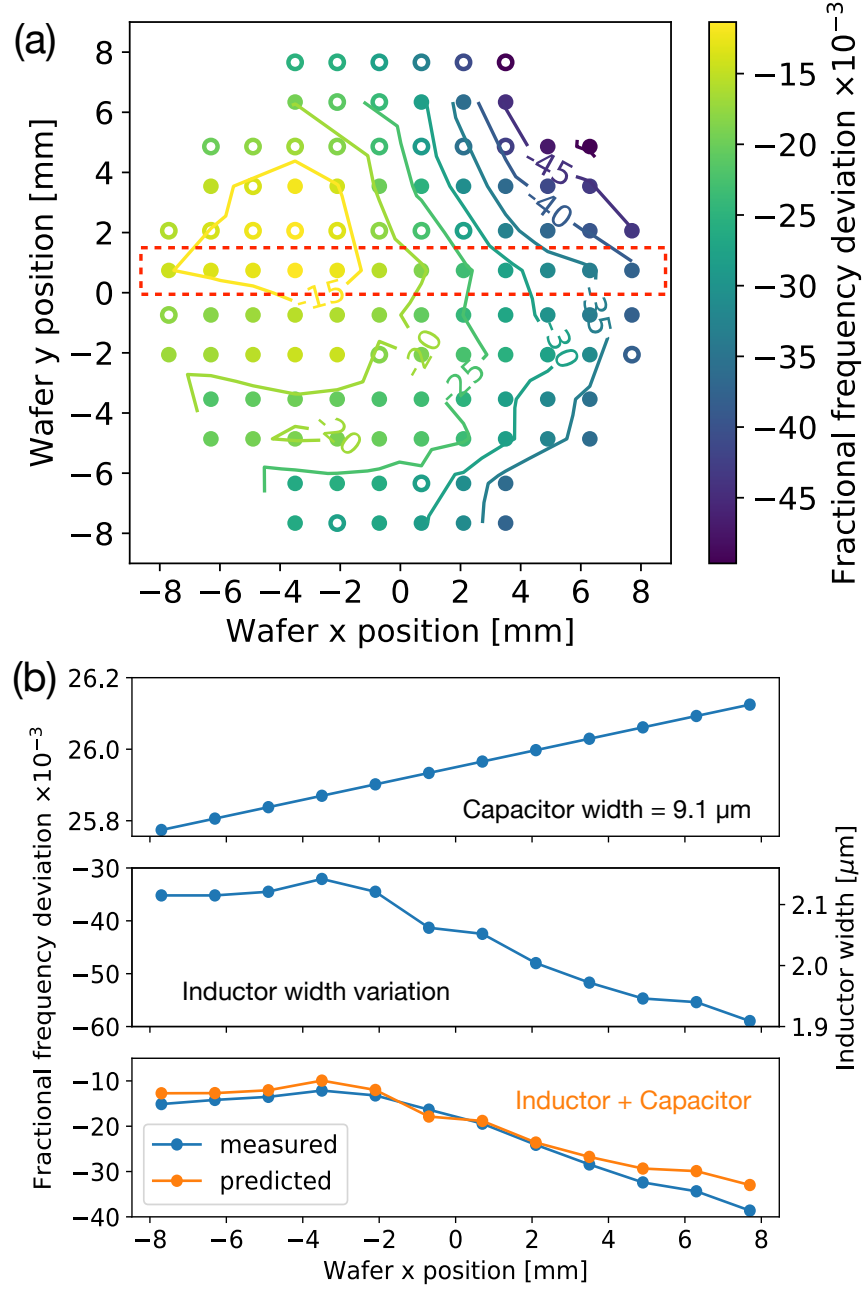


Figure 5.3: (a) Mapping of the fractional frequency deviation $\delta f/f$ with respect to the position of resonator on wafer. The resonance frequencies of unidentified resonators (unfilled circle) are inter/extrapolated using radial basis functions. (b) For selected resonators, shown in the red rectangle in (a), the fractional frequency deviations due to the decreased IDC finger width, estimated from simulation, and induced by the variation of the inductor width, measured with SEM, are plotted in the upper and middle panel respectively. The bottom panel shows the sum of both deviations from capacitor and inductor, consistent with the measured one. The maximum deviation between estimation and measurement is smaller than 6×10^{-3} .

5.2.3 Resonance frequency deviation

To evaluate the cause of the frequency deviations, we have measured the capacitor and inductor widths of a selected line of resonators, shown in Fig. 5.3(b), using a scanning electron microscope (SEM). These measurements show that the capacitor widths keep a constant value of $9.1\text{ }\mu\text{m}$ instead of the designed $10\text{ }\mu\text{m}$, however, the inductor widths w vary from $1.9\text{ }\mu\text{m}$ to $2.14\text{ }\mu\text{m}$ instead of $2.5\text{ }\mu\text{m}$ in the design. The fractional frequency deviation resulting from the $0.9\text{ }\mu\text{m}$ narrowed IDC fingers, shown in Fig. 5.3(b), are estimated using simulation. The small variation, as a function of frequency (position on wafer), is caused by the quasi-lumped element property. To understand the effect of the variation of the inductor width, we assume the capacitance C is constant and the frequency deviation is derived as

$$\frac{\delta f}{f} = \frac{1}{4} \frac{\delta w}{w}, \quad (5.1)$$

where $f = 1/(2\pi\sqrt{LC})$ and the inductance $L \propto 1/\sqrt{w}$, a good estimation for a narrow lumped-element inductor [93]. Using Eqn. 5.1, the fractional frequency deviation caused by the variation of the inductor width is calculated and shown in Fig. 5.3(b). The fractional frequency deviations obtained by adding these two deviations together, is consistent with the measurement and the small difference can be explained by the variation of the inductor width inside one resonator. In principle, this information could be used to adapt the resonance frequencies without the need of an optical measurement, to an accuracy of fractional frequency of 6×10^{-3} . We notice that the resonance frequency is very sensitive to the inductor width, around $250\text{ MHz}/\mu\text{m}$ at 2.5 GHz . This variation not only changes the resonance frequency but also the responsivity, which is determined by the quasi-particle density and inductor volume. For low-resistivity Al LEKIDs, to achieve optimal optical coupling, the inductor track is inevitably designed to be narrow with respect to the pixel size and wavelength. Therefore, to decrease the resonance frequency deviation, it is important to improve the Al pattern uniformity during the lithography, development and etching processes. We can also decrease the deviation using the trimming technique, when the physical

resonators are characterized.

5.3 Apply trimming on IDC fingers

The trimming process is performed as follows. For the resonances unidentified during the optical mapping, a inter/extrapolation method based on radial basis functions was used to estimate their frequencies. This is a simple estimation and the inter/extrapolated resonance frequencies are referred as $f_{\text{inter/extrapolated}}$. We did not compare the $f_{\text{inter/extrapolated}}$ to the resonance frequencies measured by VNA and this estimation can be improved in the future. Alternatively, the missing 33 resonances could be identified in a second optical run.

The second step is to find the relation between the resonance frequency shift and the trimming lengths. Since our MKIDs have a compact design, the total capacitance cannot be estimated accurately from the total IDC finger length with a linear relationship. We used Sonnet Suites [80] to simulate the frequency shifts with different trimmed lengths at selected resonance frequency configurations (Fig. 5.4(a)). To increase the precision of length definition during patterning, we only trim one pair of the IDC fingers. The alignment error of the contact lithography along the IDC finger direction is compensated by the symmetry of trimming, compared to trimming only a single IDC finger. Therefore, the total trimmed length on one resonator can be kept the same even with a few μm alignment error. The simulations were done with an arbitrary sheet inductance $2\text{ pH}/\square$. Since the capacitance is not affected by the sheet inductance, the fractional frequency shift caused by trimming is constant for any sheet inductance. Therefore, we could apply the simulation results to our sample without knowing the actual sheet inductance in advance.

Next, we determine the actual trimming length. By trimming the IDC finger shorter, the resonance frequency can only be shifted to a higher frequency. We keep the same frequency order as in the initial design. The largest fractional frequency deviation sets the lower limit of the re-designed resonance frequencies. Given the re-designed frequencies f_{redes} from 2.415 GHz to 2.905 GHz with spacing 4.4 MHz, the

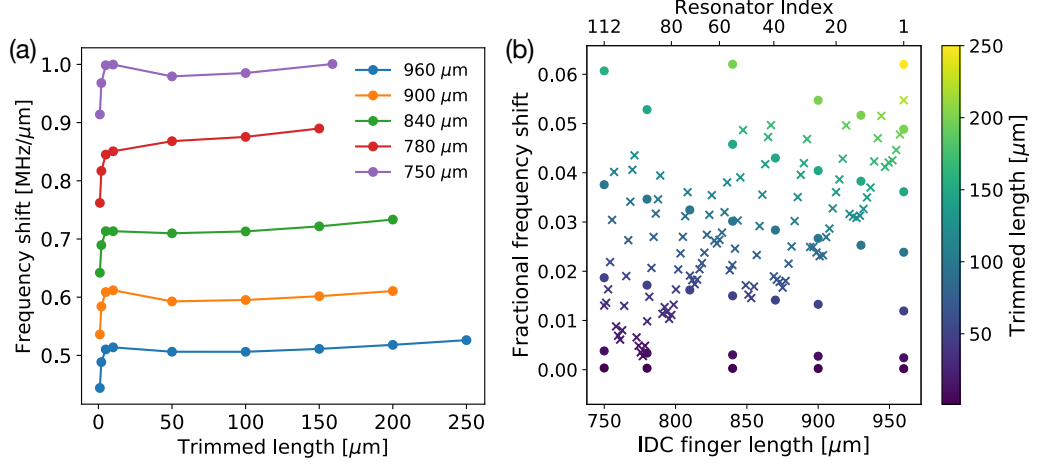


Figure 5.4: (a) Resonance frequency shifts per micrometer trimmed, simulated for different trimmed lengths. Different curves indicate different IDC fingers lengths. (b) Given the IDC finger length and the required frequency shift of a resonator, the length of IDC to be trimmed is interpolated from this plot.

needed fractional frequency shifts are calculated by $(f_{\text{redes}} - f_{\text{meas}})/f_{\text{meas}}$. Then the trimming lengths are determined by a cubic interpolation of the simulation results from the needed fractional frequency shifts, calculated based on Fig. 5.4(a).

Finally, the trimming was done using a conventional contact lithography patterning, followed by a wet etching process to trim the IDC fingers, as shown in Fig. 5.1. Considering the 365 nm exposure wavelength and the alignment accuracy, the length definition accuracy is about 0.5 μm and the trimmed frequency accuracy is estimated to be 0.4 MHz on average.

5.4 Results after trimming

5.4.1 Resonance frequency deviation

After the trimming process, the sample was cooled down again and the feedline transmission S21 was measured with the same setup used before trimming (see Fig. 5.2(a)). The resonances that were identified in the first characterization run were tuned with a standard deviation of $f_{\text{remeas}} - f_{\text{redes}}$ of only 0.46 MHz after trimming, which is con-

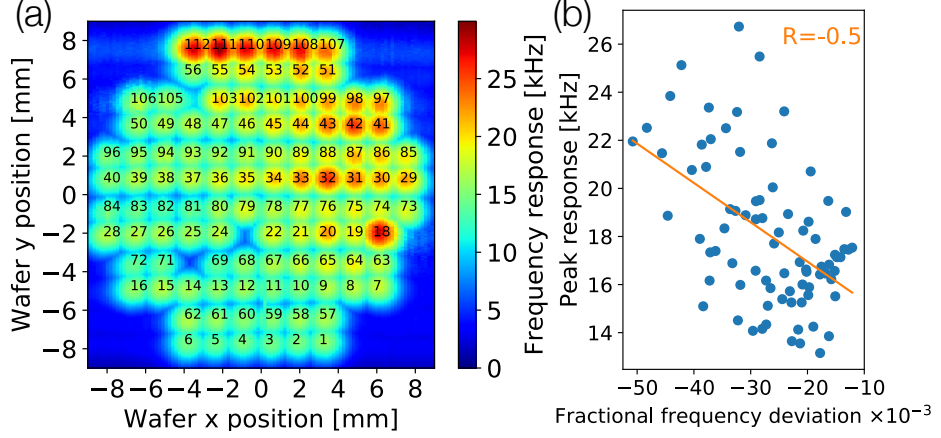


Figure 5.5: (a) Beam mapping of all measured pixels after trimming. 108 out of 112 pixels are mapped using the beam mapping system. The resonator indexes in the initial design are shown on each beam. (b) The peak response of each pixel is plotted against its fractional frequency deviation. From the data, a moderate correlation ($R = -0.5$) is found, which partly explains the variation of the optical response.

sistent with our fabrication accuracy. We notice that the f_{remeas} after trimming has a 1.7 MHz offset to the f_{redes} , an effect that is also observed in other experiments [92]. Since all resonators were trimmed and no resonator was left as reference, we cannot determine whether this offset is caused by the trimming process or by a change of the film properties. The fractional frequency deviation $(f_{\text{remeas}} - f_{\text{redes}})/f_{\text{redes}}$ of the resonators identified before trimming has a mean value of -6.4×10^{-4} and standard deviation of $\sigma = 1.8 \times 10^{-4}$ (Fig. 5.2(c)). This corresponds to a factor of 3 improvement in terms of fractional frequency deviation compared with previous results [92]. We also notice that the absolute frequency deviation after trimming is constant and does not increase with increasing resonance frequency in our 490 MHz bandwidth. This indicates that the σ of absolute frequency deviation stays constant and the fractional frequency deviation can be extremely small for high frequency resonances. For the inter/extrapolated resonances, the standard deviation of $f_{\text{remeas}} - f_{\text{redes}}$ is 3.7 MHz, because of the inaccuracy of the inter/extrapolation. The maximum deviation of all resonators is 11.3 MHz from the mean deviation.

5.4.2 Optical property

The optical beam mapping, shown in Fig. 5.5, was measured using the beam mapping system. 108 out of 112 pixels (96.7%) are measured. No pixel-to-pixel crosstalk is observed down to the noise level (-15 dB). This confirms that we have eliminated the problem of frequency collision. This improvement is obtained by a reduction of the frequency span, making it smaller than the readout bandwidth, and an increase of the homogeneity of the resonance frequency spacing. The missing 4 pixels were identified in the optical microscope and showed fabrication defects. Only one of these pixels was damaged during the trimming fabrication step. The variation of the response of each pixel has a moderate correlation ($R = -0.5$) with the resonance frequency deviation, which is mainly caused by the variation of the inductor width. The responsivity also depends on the quality factor and absorption efficiency by impedance matching, but both these two quantities depend on the inductor width, which makes it hard to do a thorough analysis. The measured noise around the readout frequency (23 Hz) stays the same after trimming.

5.4.3 Quality factor

Before trimming the Q_i spreads in a large range, shown in Fig. 5.6. After trimming Q_i slightly decreased from 2.1×10^4 to 1.8×10^4 and the coupling quality factor Q_c stayed unchanged. From Fig. 5.6(c), the Q_i of the resonators, which have the lowest Q_i , increased after trimming and the Q_i is decreased for the other resonators. Also the Q_i is more regular in the plot having high Q_i in the central part on the wafer, shown in (d). We also measured the Q_i in dark, which is much higher than the loaded Q_i as shown in Fig. 5.6(e), so the loaded Q_i is dominated by the background radiation. Therefore, the measured change of Q_i might be caused by the change of optical properties. From Fig. 5.6(b), the angular resolution is decreased from $9.8''$ to $10.2''$. This suggests that the array was placed at a worse position with respect to the focal surface, so the array should receive less power than before, meaning a higher Q_i in contrast to the results. Since in the Q_i measurements the detectors are

under the inside-cryostat background radiation, the change of cryostat temperature may explain this contradiction.

5.5 Conclusion

The multiplexing factor and the array optical yield is increased from 79 to 108 and from 70.5% to 96.7%, respectively. Before trimming the resonance frequency deviation is mainly caused by our fabrication process. After trimming, the trimming accuracy, in terms of fractional resonance frequency deviation, is $\sigma = 1.8 \times 10^{-4}$, limited by the fabrication process. A minimal resonance frequency spacing 1.66 MHz is calculated using the 5-linewidth frequency collision criterion $5f/Q$, allowing 300 resonators to be placed within a 500 MHz readout bandwidth, while the design in this chapter only holds 112 resonators. The current NIKA2 1mm array has 1140 LEKID pixels [27] on 8 feedlines. Using the trimming technique described in this Chapter, this number could be increased to about 2400 pixels with high yield.

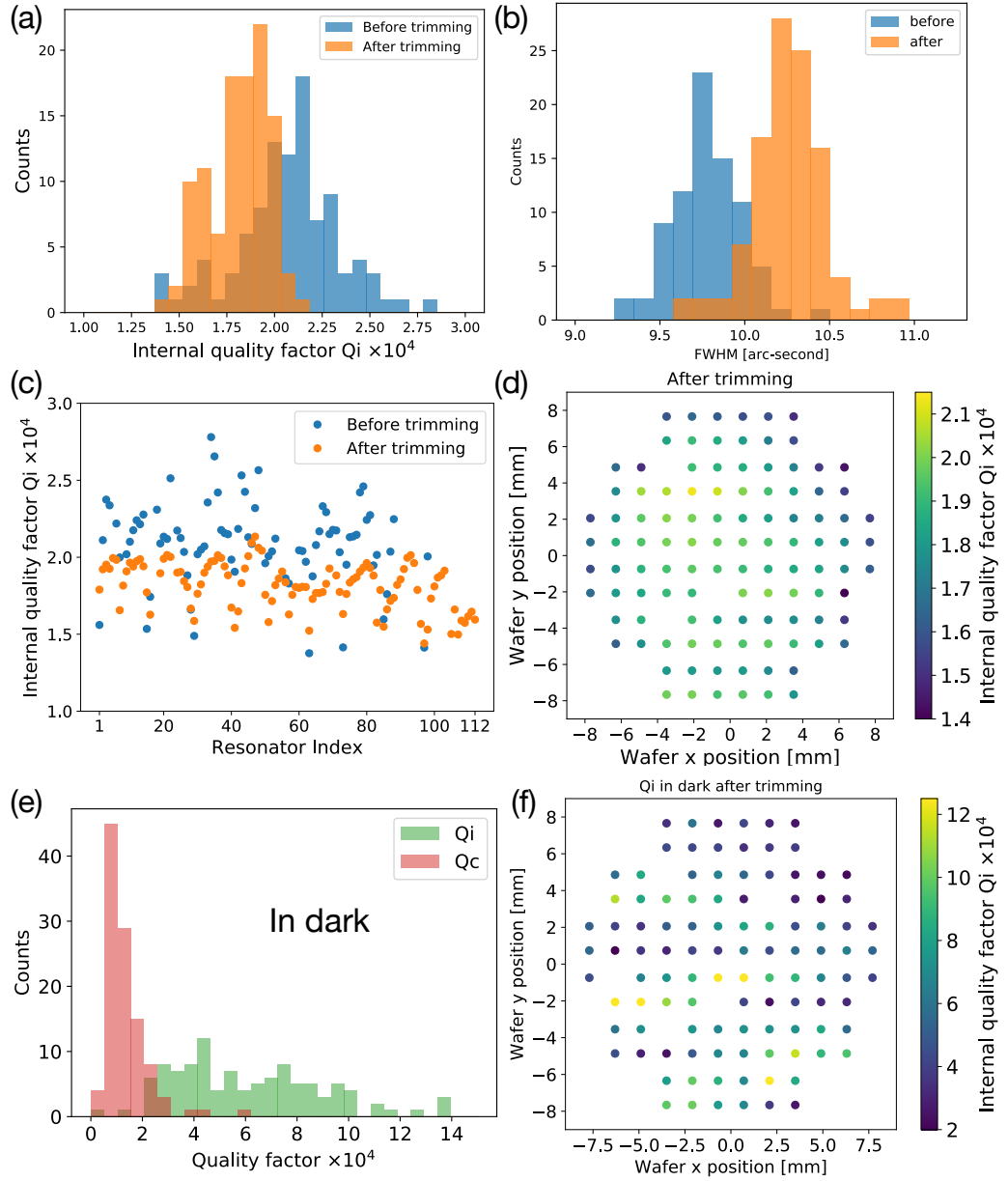


Figure 5.6: (a) Histogram of Q_i before and after trimming. (b) Histogram of angular resolution before and after trimming. (c) Comparison of Q_i on each resonator. (d) Mapping of Q_i on wafer under optical loaded. (e) Histogram of Q_i after trimming in dark. (f) Mapping of Q_i on wafer in dark.

Chapter 6

Applying capacitor trimming technique on 4-inch LEKID arrays

6.1 Introduction

In Chapter 4, we demonstrated a high-angular resolution pixel design suitable for the future upgrade of the NIKA2 instrument. In the Chapter 5, we have successfully applied the trimming technique on a hundred-pixel array with a 96.7% yield. Based on these two works, we demonstrate a new 4-inch array design with 2392 high angular resolution pixels and 8 feedlines within 500 MHz readout bandwidth. We first characterized and mapped half of the array, which contains ~ 1000 pixels, due to the limitation of 4 readout feedlines available in the cryostat. After the characterization, we applied the trimming technique on the array by etching part of the capacitor fingers. Then a second characterization was done to evaluate the array performance after trimming.

6.2 Array design

This array is designed for 260 GHz band, so a 250 μm high-resistivity silicon substrate is used. The material is Al with thickness of 18 nm, $R_s = 1.6 \Omega/\square$ and $L_s = 2 \text{ pH}/\square$. This LEKID design is based on the design introduced in Section 4.4. The inductor parts keeps the same 3rd-order Hilbert curve, which has been shown a 100% absorption efficiency in Sec. 3.5.3. For the capacitor, the number of fingers is increased

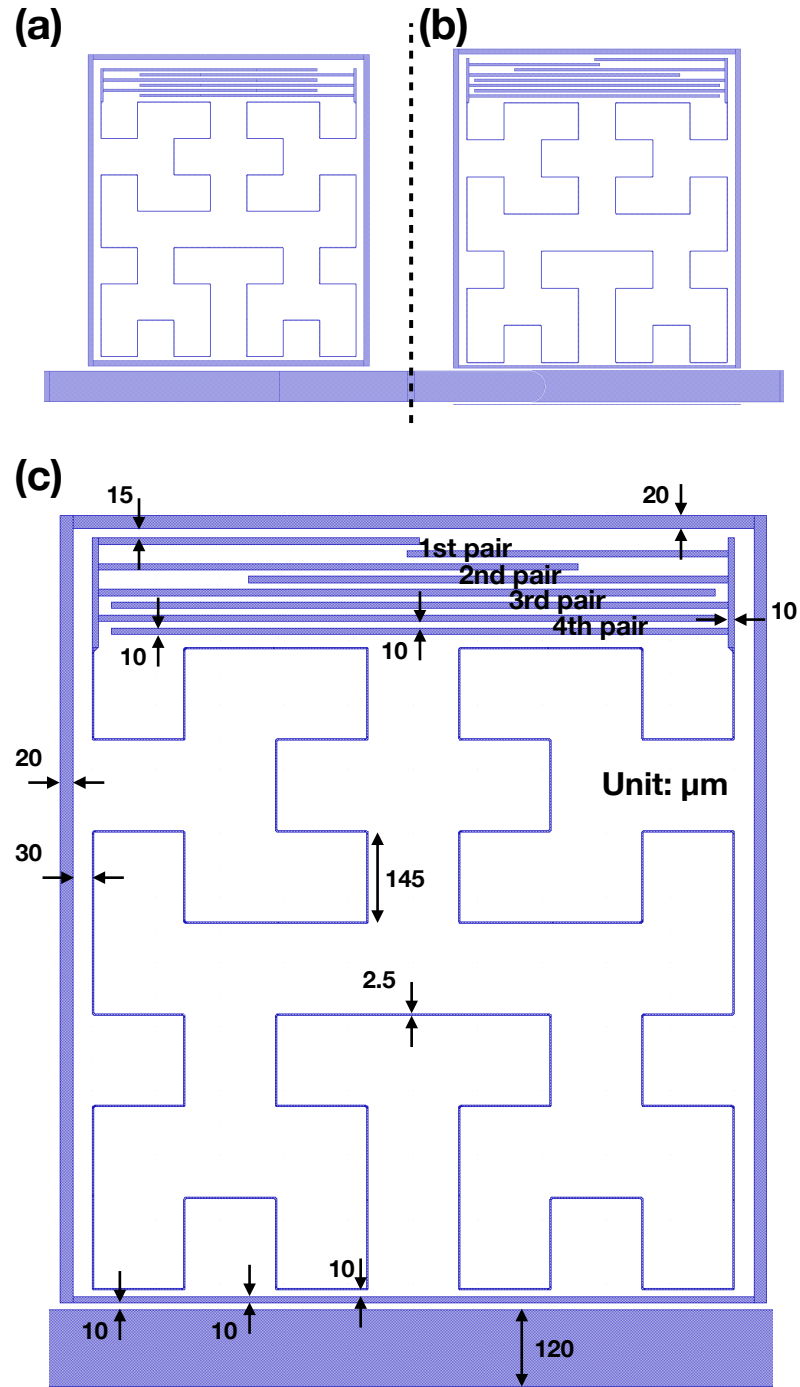


Figure 6.1: (a) The old LEKID design with all capacitor fingers having the same length, described in Section 4.4. (b) The new LEKID design has the same inductor design in (a), but the number of capacitor fingers is increased and the whole pixel is slightly larger. (c) The design parameters of LEKID.

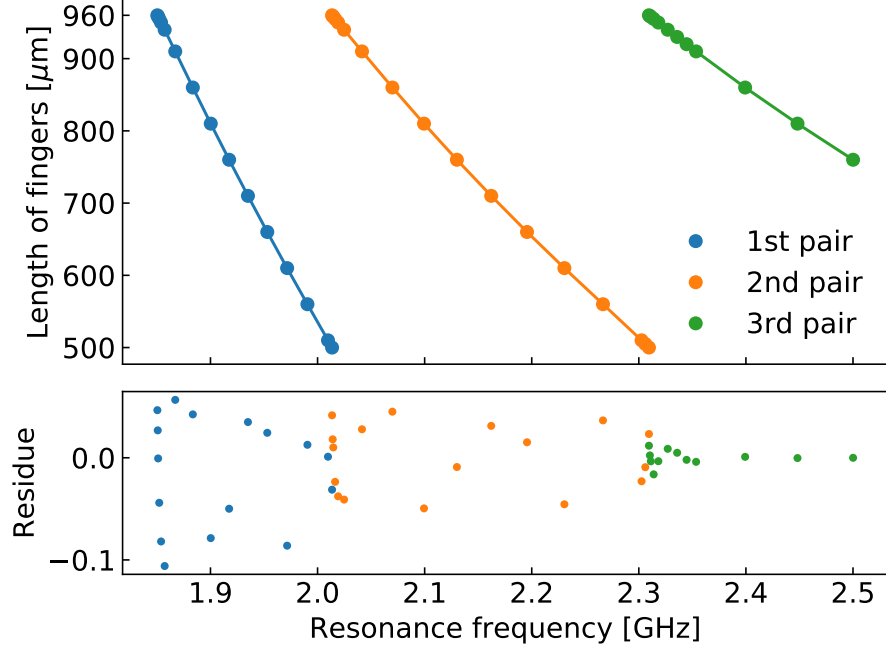


Figure 6.2: (a) Design of the resonance frequency by changing the length of capacitor fingers. Selected configurations are simulated to cover the full bandwidth. The simulated data is fitted using polynomial functions. The residue is within 100 nm, much smaller than the fabrication accuracy.

from 6 to 8. This increases the capacitance and decreases the resonance frequencies. The trimming accuracy is then increased since the ratio between the frequency shift and trimmed finger length is decreased. Also the capacitor is tuned by changing the length of fingers pair by pair instead of changing the lengths of all fingers together. This difference is well shown in Fig. 6.1. For the trimming step, we follow the same trimming process, as presented in Chapter 5, that one or maximum two pairs of fingers are wet-etched symmetrically to shift all the resonance frequencies. Also the shifts of resonance frequencies are based on the initial designed resonance frequencies, shown in Fig. 6.1, so no extra simulation is needed to have the resonance frequencies after trimming. In total, the trimming accuracy could be increased from 0.22 MHz–0.50 MHz to 0.18 MHz–0.44 MHz in this new design, assuming only one pair of fingers is trimmed, 0.5 μm lithography resolution and $L_s = 2 \text{ pH}/\square$.

The resonance frequency is tuned by changing the length of fingers pair by pair.

Table 6.1: Feedline configuration

Feedline	1/8	2/7	3/6	4/5
Number of pixels	276	276	312	332
Frequency spacing [MHz]	1.82	1.82	1.61	1.51

We defined the longest finger length to be $960\text{ }\mu\text{m}$ and the shortest length to be $500\text{ }\mu\text{m}$. When the frequency is higher than the frequency range of the first pair of fingers, we keep the first pair with the shortest length and then decrease the lengths of the second pair, and so on. To obtain the lengths for a given frequency, the resonance frequencies are simulated in Sonnet and then fitted using a polynomial function, shown in Fig. 6.2. The fitting result yields a $< 100\text{ nm}$ uncertainty on the finger length needed for a given resonance frequency. The designed resonance frequencies are from 1.8505 GHz to 2.3505 GHz . To cover the frequency range after trimming, the frequency is simulated up to 2.5 GHz . The electric crosstalk between pixels are estimated to be at maximum 55 kHz , using the method discussed in Section 4.4. The crosstalk between feedlines has a maximum value of -21 dB at the resonance position, evaluated in Sonnet. To minimize electrical crosstalk, pixels on opposite sides of the feedline are spaced 250 MHz apart. The Q_c is optimized to 0.85×10^4 – 1.2×10^4 to match the expected internal quality factor $Q_i = 1 \times 10^4$ under 50 K background radiation.

To cover a 80 mm diameter circle, 8 feedlines are used, with a total of 2392 pixels. The pixel positions and feedlines are left-right symmetric, but the resonance frequency always starts at the bottom-left pixel and ends at the top-right pixel. The number of pixels and the frequency spacing for each feedline are listed in Table 6.1.

6.3 Characterization before trimming

The array was fabricated using the fabrication recipe described in Appendix A. After dicing, the array is placed in the NIKA2 holder, shown in Fig. 6.3, and cooled down to 100 mK in the cryostat NIKA1.5. Due to the limited number of readout lines, we can only measure four feedlines in one cool-down. During the measurements, we found

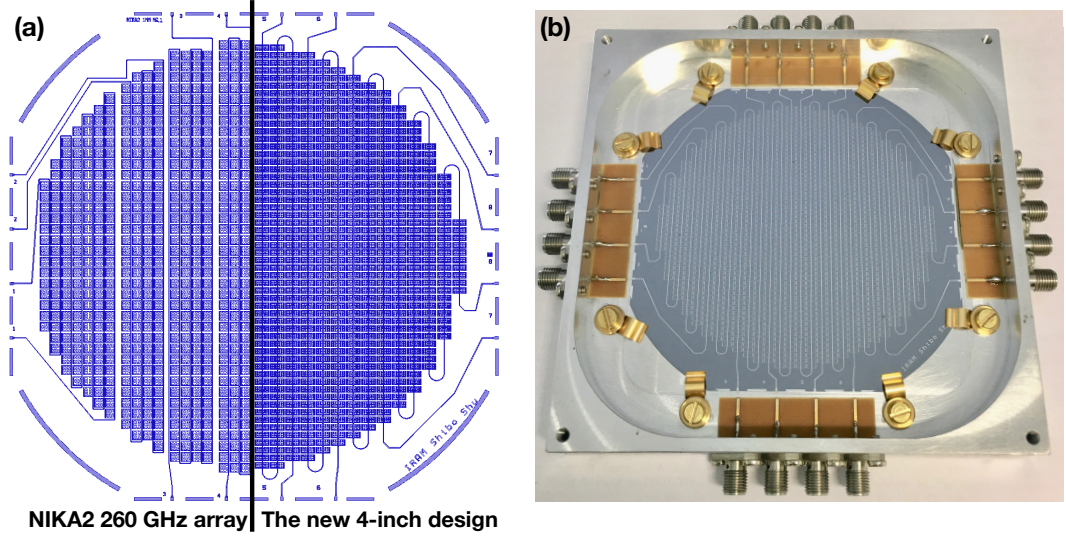


Figure 6.3: (a) The comparison of the current NIKA2 260 GHz and the new 4-inch array design. (b) Photo of the new 4-inch array in a sample holder.

the feedline 2 is disconnected, probably due to a fabrication defect on the feedline. We performed the S21 and optical mapping measurements on the other three feedlines, feedline 1, 3 and 4. The S21 is measured from 1.8 GHz to 2.5 GHz using VNA, shown in Fig. 6.4, 6.5 and 6.6. In total 721 out of 920 resonances are successfully fitted from S21 measured from VNA. The details are listed in Table 6.2.

To locate the positions of resonances, we performed optical mapping on feedline 1, 3 and 4 using the sky simulator introduced in Sec. 4.5. The optics of this cryostat is similar to the one used in Sec. 4.5, but only the magnification factor is 2.5 instead of 5.9, due to an extra lens used to increase the focal plane size from 2 to 4 inches. The transmitted optical band is defined by a 169 GHz high pass and 304 GHz low pass filters, but the detector is only sensitive in the range from 230 GHz to 270 GHz, as defined by the 250 μm backshort distance. The optical mapping is performed by scanning y-axis at fixed x position. The x step is 1 mm, corresponding to 0.4 mm on the focal plane. The scanning speed is about 4 mm/s, corresponding to 1.6 mm/s on the focal plane. Compared with the designed 1.4 mm pitch size, this configuration

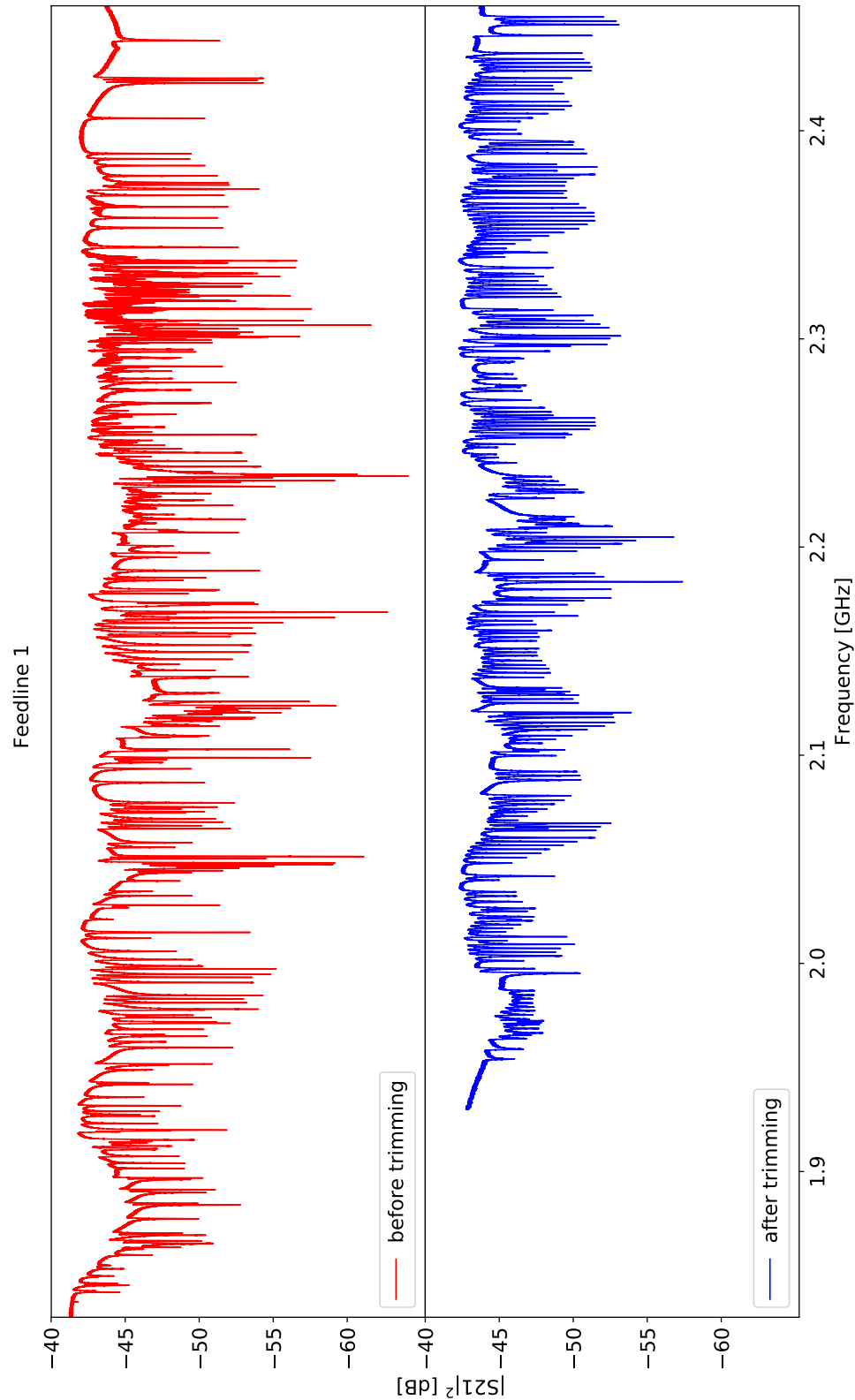


Figure 6.4: The measured S21 of feedline 1 before and after trimming.

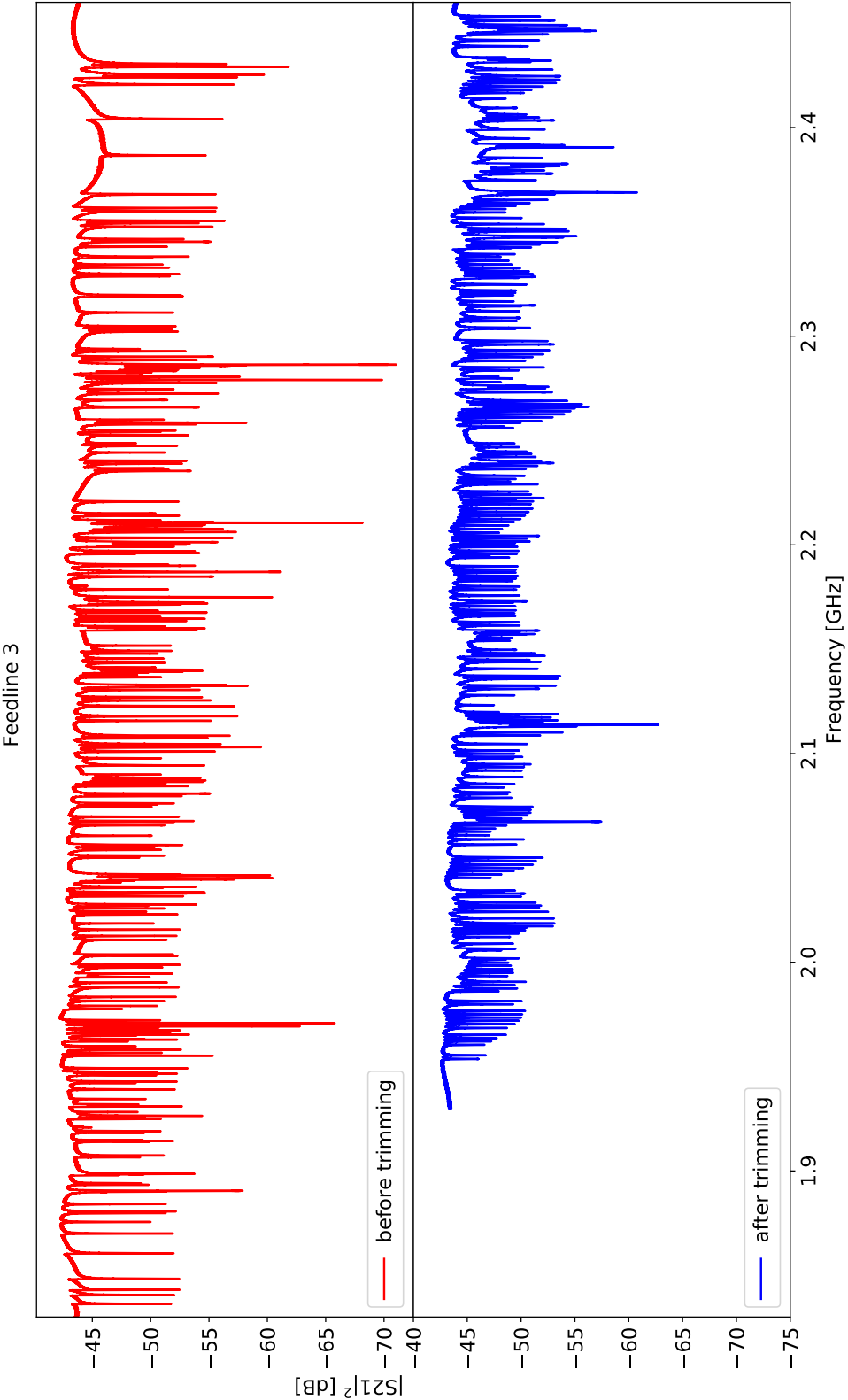


Figure 6.5: The measured S21 of feedline 3 before and after trimming.

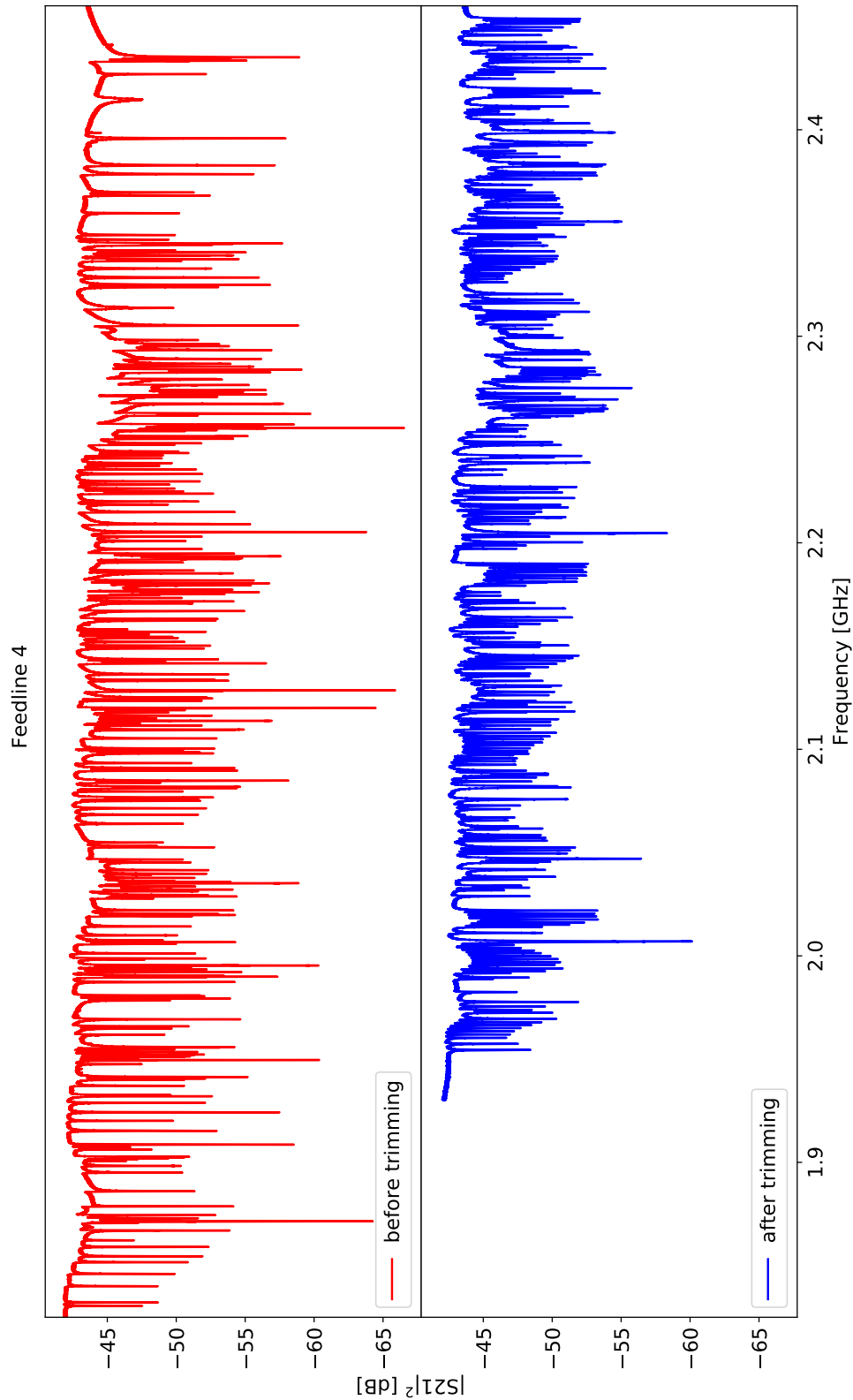


Figure 6.6: The measured S21 of feedline 4 before and after trimming.

Table 6.2: Numbers of resonators before and after trimming

Feedline			1	3	4	Total
Number of resonators in design			276	312	332	920
Fabrication yield ¹			230	263	276	769
			83 %	84 %	83 %	84 %
Before trimming	fitted from S21		217	242	262	721
	optically mapped		182	228	225	635
			66 %	73 %	68 %	69 %
After trimming	fitted from S21		220	259	270	749
	optically mapped		210	242	249	701
			76 %	78 %	75 %	76 %
	missing resonators	hardware ²	9	15	21	45
		damaged	11	6	6	23

¹This is counted as the resonators optically mapped before and after trimming.

²The number of readout tones is limited to 50 in each 100 MHz.

is accurate enough to locate the positions of resonators. To avoid the complexity of using three readout boards simultaneously, the feedlines are mapped one by one using a single board. Each feedline data is analyzed individually and then they are combined together in the final step. Since the resonance bandwidth is larger than 500 MHz, we performed twice optical mapping for each feedline to cover all 700 MHz bandwidth. The duplicate resonances measured in both mappings are removed from the second mapping.

The mapping results are shown in Fig. 6.7(c). The fractional frequency deviation spans from 0.04 to -0.04 with an obvious slope. This slope mainly follows the Al thickness variation, shown in Fig. 6.7(a), measured using ellipsometer just after the Al deposition. To understand the effect of the thickness variation, we assume the capacitance C is constant and the frequency deviation is derived as

$$\frac{\Delta f}{f} = -\frac{1}{2} \frac{\Delta L}{L} \quad (6.1)$$

from $f = 1/(2\pi\sqrt{LC})$. Since the thickness of Al is only 18 nm, much smaller than the penetration depth λ , the film is in the thin film limit and the surface impedance

can be simplified to [53]

$$Z_s = R_s + i\omega L_s = \frac{1}{\sigma t} = \frac{1}{(\sigma_1 - i\sigma_2)t}, \quad (6.2)$$

where t is the Al thickness. Since $\sigma_2 \gg \sigma_1$, the R_s and σ_1 are negligible and we have

$$L \propto \frac{1}{\sigma_2 t} \propto \frac{1}{\sigma_n t} = \frac{\rho}{t}, \quad (6.3)$$

where ρ is the resistivity and $\sigma_1 \propto \sigma_n$ assuming this small variation of thickness only changes the normal conductivity. For thin metal film, ρ varies with thickness. From the resistivity data measured from Al films with different thickness using the same deposition method, the relation $\rho \propto 1/t$ is fitted from the data presented in Appendix A. Then we have

$$\frac{\Delta L}{L} = -2 \frac{\Delta t}{t} \quad (6.4)$$

and from Eqn. 6.1 we have

$$\frac{\Delta f}{f} = -\frac{1}{2} \frac{\Delta L}{L} = \frac{\Delta t}{t}. \quad (6.5)$$

In Fig. 6.7(f), $\Delta f/f$ and $\Delta t/t$ are plotted to compare with this equation. For $t < 17.8 \text{ nm}$, the frequency deviation is dominated by the Al thickness variation and the dispersion is smaller than 0.01. From Eqn. 6.5, 100 nm variation on the inductor width gives 0.01 variation on fractional frequency deviation, so this dispersion of 0.01 could be explained by the $\pm 50 \text{ nm}$ pattern accuracy on the optical mask used for the contact photolithography of the array. This is improved from the $\pm 150 \text{ nm}$ mask accuracy in Chapter 5, which shows a larger frequency deviation.

Besides the Al thickness variation, other factors may give the extra deviation. For $t > 17.8 \text{ nm}$, a large part of the deviation is not dominated by the thickness variation. These resonances are located on top and central parts of the array, as shown in Fig. 6.7(d). The fractional deviation is from -0.01 to 0.04 , of the same order of magnitude as the deviation observed in Chapter 5. It is possible that this deviation is also dominated by inductor width variation, which has a similar level

discussed in Sec. 5. This could be a combined effect between the pattern on the mask and the pattern definition process.

In Fig. 6.7(d), the top and central parts may not have the same causes. The central pattern might be caused by the inductor width variation due to the non-uniformity of photoresist thickness. In the pattern definition process, the photoresist should contact the mask, but there could be a gap if the thickness of photoresist is not uniform. Then the gap will change the pattern accuracy, which give the inductor width variation. This could be improved by increasing the resist uniformity. For the top part, the frequency deviation might be explained by the film property, since we observed similar patterns both on the AlOx thickness map and the frequency deviation map before trimming, as shown in Fig. 6.7.

In general, most part of the frequency deviation could be decreased by improving the film properties and pattern definition process. The fabrication yield should be improved first, since it limits the final yield after trimming. Then we should control the thickness variation less than 5 %, compared with the current 8 %, by aligning the material thickness center with the substrate center during deposition. To further improve the frequency deviation, we should improve on the pattern accuracy on the mask the the pattern definition process.

6.4 Trimming process

In the first characterization, we have measured f_{meas} and the resonance frequencies of the unmeasured resonances are inter/extrapolated using radial basis function. We re-designed the resonance frequencies f_{redes} from 1.955 GHz to 2.455 GHz for each feedline after trimming. All resonances have $f_{\text{redes}} > f_{\text{meas}}$ meaning all resonators are trimmed. The relation between the designed and measured resonance frequencies is given by

$$\frac{\Delta f}{f} = \frac{f_{\text{meas}} - f_{\text{des}}}{f_{\text{des}}} = \frac{f_{\text{redes}} - f_{\text{trim}}}{f_{\text{trim}}} \quad (6.6)$$

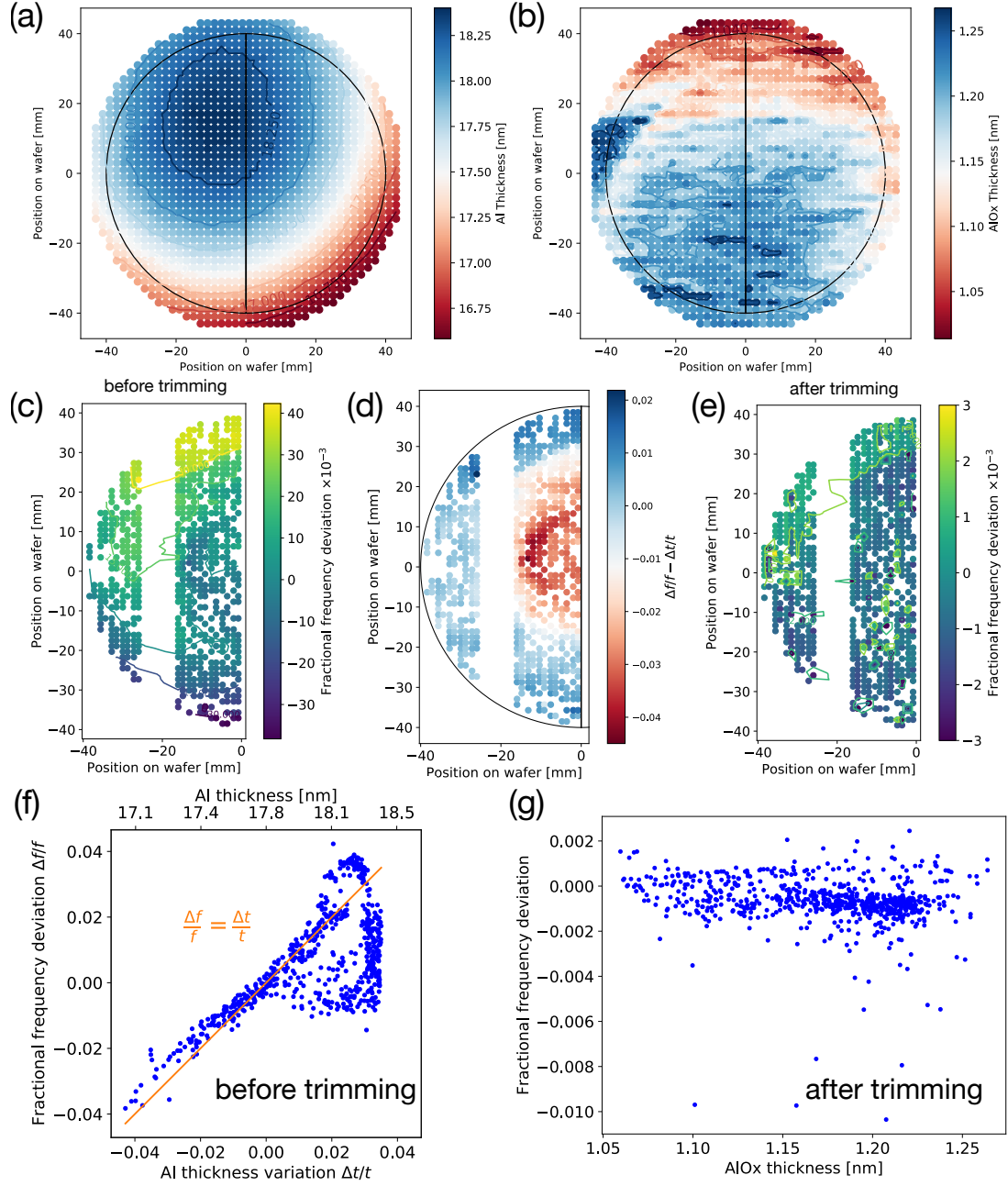


Figure 6.7: (a) Mapping of Al thickness using ellipsometer. The left black semicircle corresponds to the three measured feedlines. The thickness at the resonator positions is interpolated from this map. (b) Mapping of AlOx thickness using ellipsometer. (c) Mapping of the fractional frequency deviation before trimming. (d) The difference between fractional frequency deviation and Al thickness variation. From Eqn. 6.5, the frequency deviation is dominated by thickness variation if the value is close to zero. (e) Mapping of the fractional frequency deviation after trimming. (f) $\Delta f/f$ before trimming versus $\Delta t/t$. The reference thickness 17.8 nm is determined by where $\Delta f/f = 0$. (g) $\Delta f/f$ after trimming versus the AlOx thickness.

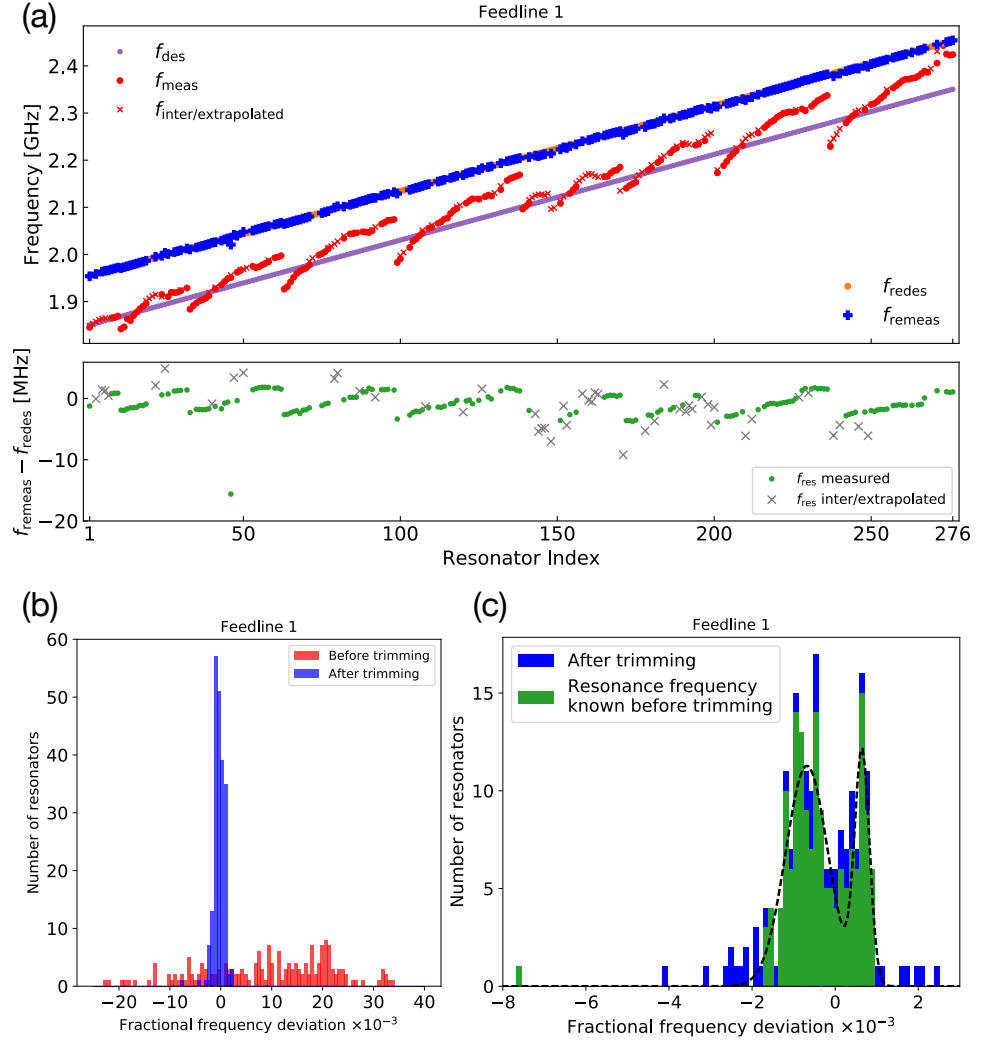


Figure 6.8: (a) Designed (f_{des} , purple dot) and measured (f_{meas} , red dot) resonance frequencies before trimming. The resonance frequencies of unidentified resonators ($f_{\text{inter/extrapolated}}$, red cross) are inter/extrapolated based on the smooth variation of the frequency deviation (Fig. 6.7(a)). The re-designed resonance frequencies (f_{redes} , orange dot) for trimming and the re-measured resonance frequencies (f_{remeas} , blue dot) after trimming are plotted for comparison. The bottom panel shows the absolute frequency deviation between f_{remeas} and f_{redes} . The resonators with f_{meas} (green dots) have $\mu_1 = -1.48$ MHz and $\sigma_1 = 1.09$ MHz and $\mu_2 = 1.45$ MHz and $\sigma_2 = 0.34$ MHz. The resonators with $f_{\text{inter/extrapolated}}$ (gray crosses) show a larger deviation. (b) Histogram of $\Delta f/f$ before (red) and after (blue) the trimming process. After trimming the deviation is dramatically decreased, even for the inter/extrapolated resonators. (c) The green histogram shows the distribution of the resonators of which the exact frequency shift was known. The blue points show the resonators that were estimated using the inter/extrapolation described in the text. A two Gaussian fit of $\Delta f/f$ of the identified resonators is plotted (dashed line), which gives $\mu_1 = -6.8 \times 10^{-4}$ and $\sigma_1 = 5.1 \times 10^{-4}$ and $\mu_2 = 6.5 \times 10^{-4}$ and $\sigma_2 = 1.8 \times 10^{-4}$.

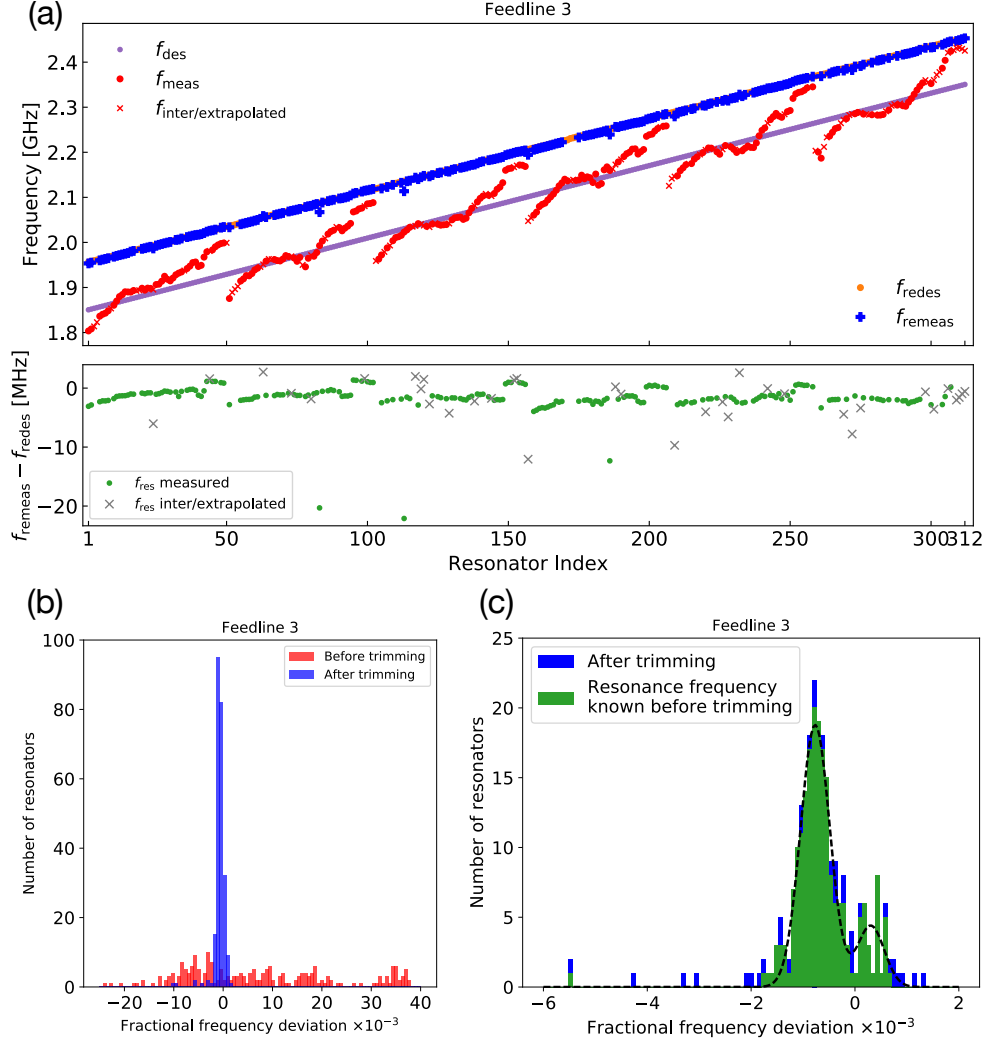


Figure 6.9: Results for feedline 3, same with Fig. 6.8. The resonators with f_{meas} (green dots) have $\mu_1 = -1.48$ MHz and $\sigma_1 = 1.09$ MHz and $\mu_2 = 1.45$ MHz and $\sigma_2 = 0.34$ MHz. A two Gaussian fit of $\Delta f/f$ of the identified resonators is plotted (dashed line), which gives $\mu_1 = -7.7 \times 10^{-4}$ and $\sigma_1 = 2.8 \times 10^{-4}$ and $\mu_2 = 3.0 \times 10^{-4}$ and $\sigma_2 = 2.6 \times 10^{-4}$.

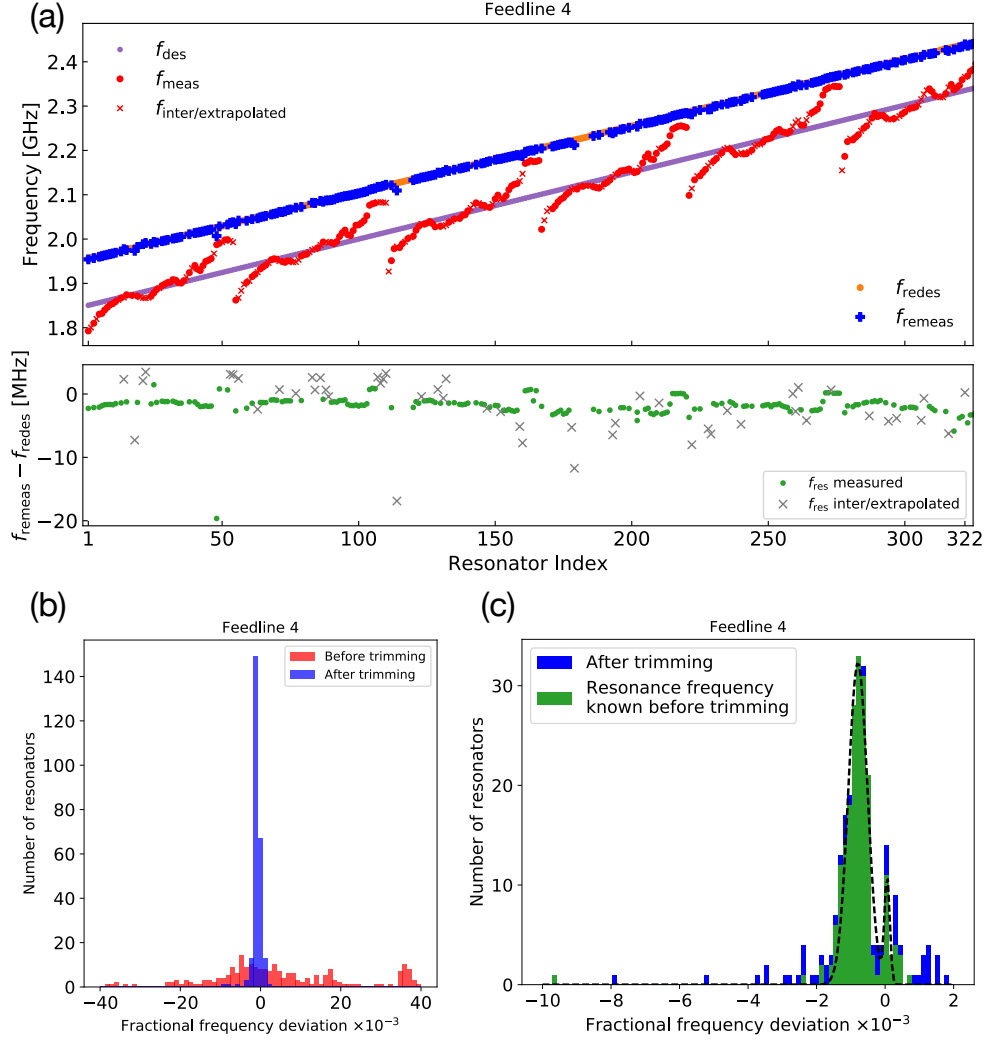


Figure 6.10: Results for feedline 4, same with Fig. 6.8. The resonators with f_{meas} (green dots) have $\mu_1 = -1.73$ MHz and $\sigma_1 = 0.66$ MHz and $\mu_2 = 0.16$ MHz and $\sigma_2 = 0.19$ MHz. A two Gaussian fit of $\Delta f/f$ of the identified resonators is plotted (dashed line), which gives $\mu_1 = -7.9 \times 10^{-4}$ and $\sigma_1 = 2.8 \times 10^{-4}$ and $\mu_2 = 0.6 \times 10^{-4}$ and $\sigma_2 = 0.8 \times 10^{-4}$.

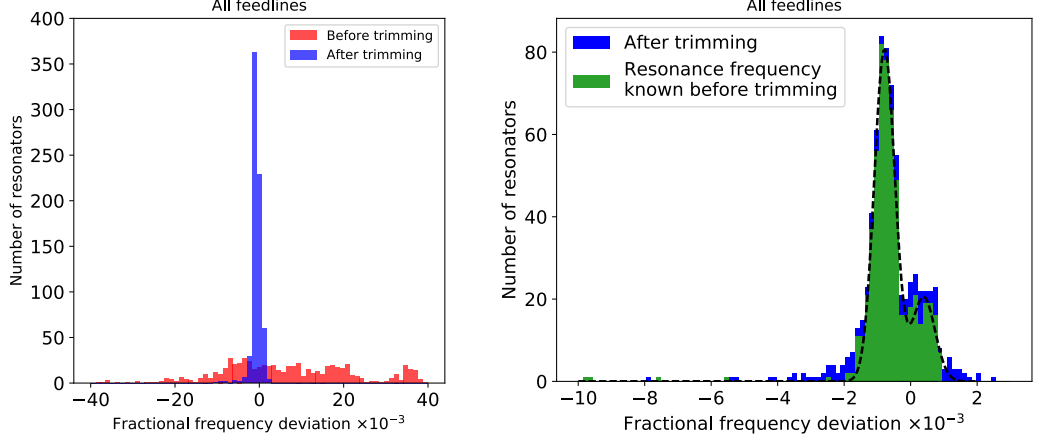


Figure 6.11: Results for all feedlines, same with Fig. 6.8. The absolute frequency deviation after trimming has $\mu_1 = -1.71$ MHz and $\sigma_1 = 0.72$ MHz and $\mu_2 = 0.88$ MHz and $\sigma_2 = 0.71$ MHz. A two Gaussian fit of $\Delta f/f$ of the identified resonators is plotted (dashed line), which gives $\mu_1 = -7.8 \times 10^{-4}$ and $\sigma_1 = 3.1 \times 10^{-4}$ and $\mu_2 = 3.9 \times 10^{-4}$ and $\sigma_2 = 3.4 \times 10^{-4}$.

where f_{trim} is the frequency we use to define the trimming mask. Then we have $f_{\text{trim}} = f_{\text{des}} f_{\text{redes}} / f_{\text{meas}}$. Since the trimming happens on the fingers pair by pair following exactly the same behaviour of the design of the resonance frequency, the capacitor finger lengths for the trimming mask can be directly calculated using the relation shown in Fig. 6.2. In this way, there is no need to do extra simulations to determine the frequency after trimming, such as done in Sec.5.4. This not only simplifies the trimming procedure but also increases the trimming accuracy. The final trimming mask is defined by the difference of the capacitor finger lengths between f_{des} and f_{trim} . Then the array is re-fabricated as described in Appendix A.

6.5 Characterization after trimming

After trimming the array is re-bonded and cooled down to 100 mK using the same setup in the first characterization. The S21 measured using VNA is shown in Fig. 6.4, 6.5 and 6.6. 23 resonators are damaged after trimming. The yield in detail is listed in Table 6.2. The resonance frequencies after trimming f_{remeas} are well ranged from

1.955 GHz to 2.455 GHz and correspond to the re-designed resonance frequencies. The resonance dips are found not as deep as before trimming, indicating a systematic degradation on the internal quality factor. For all feedlines, 749 resonances are fitted from S21. The frequency deviations for each feedline are shown in Fig. 6.8, 6.9 and 6.10. Fig. 6.11 summaries the result for all feedlines combined.

6.5.1 Resonance frequency deviation

Table 6.3: Fitting results of resonance frequency deviation after trimming

Feedline	Δf [MHz]				$\Delta f/f$ [$\times 10^{-4}$]			
	μ_1	σ_1	μ_2	σ_2	μ_1	σ_1	μ_2	σ_2
1	-1.48	1.09	1.45	0.34	-6.8	5.1	6.5	1.8
3	-1.71	0.74	0.74	0.42	-7.7	2.8	3.0	2.6
4	-1.73	0.66	0.16	0.19	-7.9	2.8	0.6	0.8
All	-1.71	0.72	0.88	0.71	-7.8	3.1	3.9	3.4

After trimming, the frequency deviation ranges from -0.01 to 0.003 , 5 times smaller than before trimming. For resonators of which the resonance frequencies are not measured before trimming, the distribution is flat, as observed before. For the resonators with resonance frequencies measured before trimming, most of them have $\Delta f/f < 0$ (group 1) and some distribute in the $\Delta f/f > 0$ range (group 2). This happens for all feedlines and especially for feedline 1, which sits on the most left part of the array. We suggest the group 1 is caused by the pattern definition accuracy and the reason for group 2 will be discussed later. To estimate the distribution, two Gaussian functions are used to fit these two groups and the results are shown in Table 6.3. We found that both the σ_1 (group 1) and σ_2 (group 2) decrease from feedline 1 to 4, which means the trimming accuracy increases from the edge ($\sigma_1 = 1.09$ MHz) to the center ($\sigma_1 = 0.66$ MHz) of the array. Also the σ_1 of $\Delta f/f$ on feedline 1 is two times higher than on feedline 3 and 4. The measured trimming accuracy of 3.1×10^{-4} is larger than the trimming accuracy of 1.8×10^{-4} in Chapter 5. This might be caused by trimming of one or two pairs of fingers instead of previous trimming of only one

pair.

The two groups of trimming results suggest that there is another factor, besides the pattern definition accuracy, limiting the trimming accuracy at least in feedline 1. One hypothesis is that the aging speeds of the Al film between the regions of group 1 and 2 are different. The aging effect has been observed during the NIKA2 runs on telescope, as well as by other groups, but this effect has not been thoroughly studied. In [92] the measured resonance frequency after trimming is found to be $\sim 2 \times 10^{-3}$ (1.5 to 1.9 MHz) lower than before trimming with TiN/Ti/TiN multilayer. In Chapter 5, we observed a similar 1.7 MHz shift and also here the $\mu_1 = -1.71$ MHz from all feedlines. Since in our cases all resonators were trimmed and no resonator was left as reference, we cannot determine whether this offset is caused by the trimming process or by a change of the film properties. For Al films, we have observed that the thickness of AlOx increases until ~ 60 h after deposition, when the film is exposed in the air. In our fabrication process, the pattern is defined less than 3 h after deposition and then protected using resist until bonding wires and cooling down. The AlOx layer may continue grow after the first measurement and for some reasons the regions of group 1 and 2 have different AlOx thickness. Then the two regions have different Al thickness, so the mean deviations μ_1 and μ_2 give different values.

The difference of aging speed may be caused by the nonuniformity of Ar cleaning. We have observed that increasing Ar cleaning time can increase the thickness of AlOx estimated from ellipsometer measurement. Although the frequency deviation after trimming has no obvious relation with the AlOx thickness from Fig. 6.7(g), we could still see that the pattern on the left top part in (b) is similar to the pattern in (e) at the same position. During Ar cleaning the uniformity of the plasma may be affected by the Al sputtering target positioned close to the left top part of the substrate. Further experiments are needed to verify the cause.

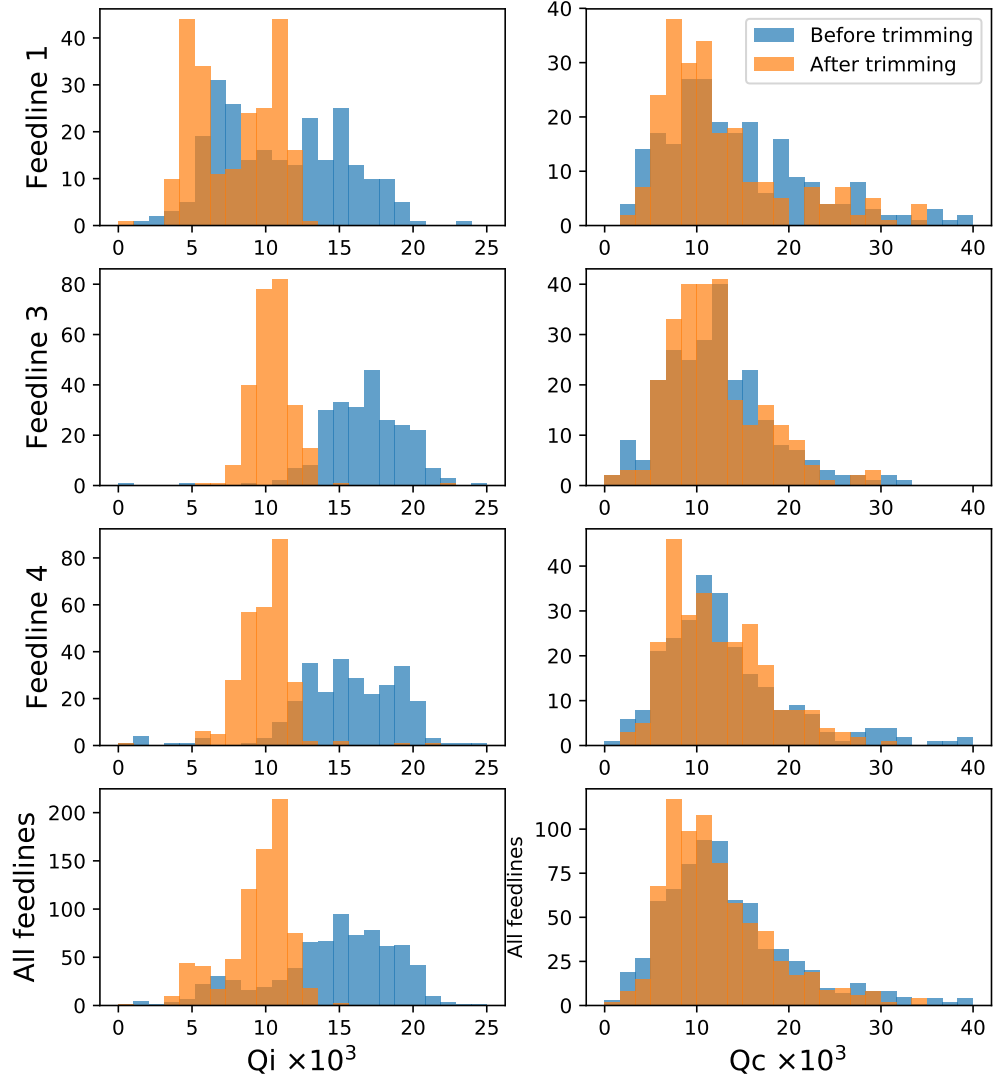


Figure 6.12: Histograms of Q_i and Q_c for all feedlines before and after trimming. Before trimming, the Q_i of feedline 1, 3 and 4 are $11.6 \pm 4.9 \times 10^3$, $17.0 \pm 3.2 \times 10^3$ and $16.0 \pm 4.3 \times 10^3$, respectively. After trimming, the Q_i of feedline 1, 3 and 4 are $7.9 \pm 2.7 \times 10^3$, $10.5 \pm 1.4 \times 10^3$ and $10.1 \pm 1.7 \times 10^3$, respectively. Q_c does not change much before and after trimming.

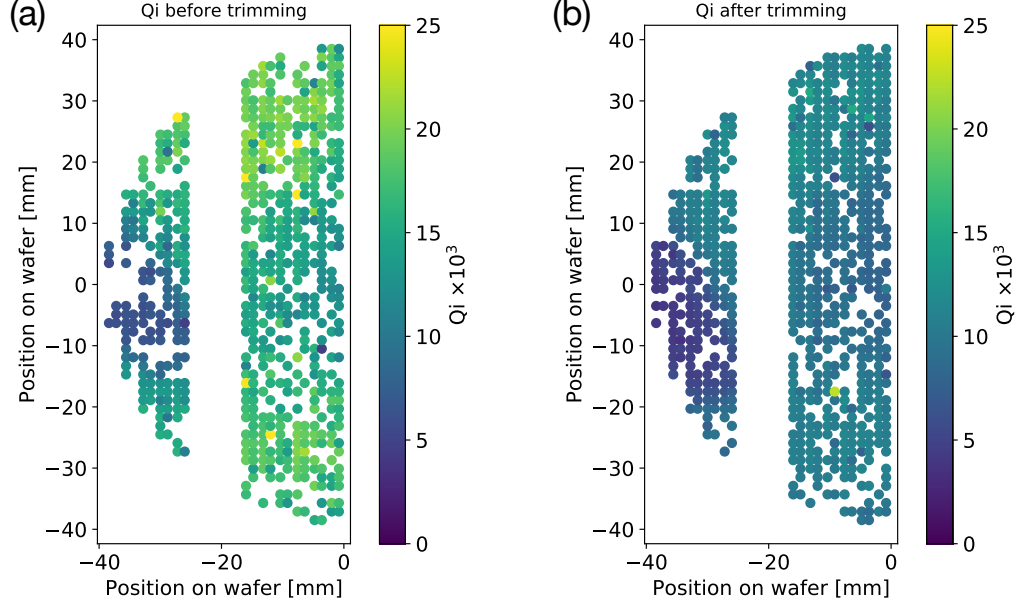


Figure 6.13: Mapping of Q_i before and after trimming.

6.5.2 Quality factor and peak response

In our experiments, the Q_i is not measured in dark and is therefore limited by the quasiparticles created by radiation. Before trimming, Q_i is about 16×10^3 for all feedlines but for feedline 1 the Q_i has a second peak with $Q_i = 7 \times 10^3$ as seen in Fig. 6.12. In the mapping of Q_i , shown in Fig. 6.13(a), we locate these low- Q_i resonators to the most-left part on the array. For this region, the resonance frequency deviation was found to be dominated by Al thickness variation, so the material parameters could not explain this. If this is caused by the difference in the optical field, the power should be two times higher to explain this 50 % lower Q_i . For feedline 3 and 4, the low- Q_i of the central resonators could be explained by optical field, which has a better beam containing more power in the center of the optical field.

After trimming the Q_i has an obvious decrease and the Q_c does not change, shown in Fig. 6.12. The Q_i decreases about 40 % from 16×10^3 to 10×10^3 . The low- Q_i resonators also decrease about 30 % from 7×10^3 to 5×10^3 . Since the Q_i is limited by radiation and the trimming result $\sigma_1 = 5 \times 10^{-4}$ shows that the changes on material

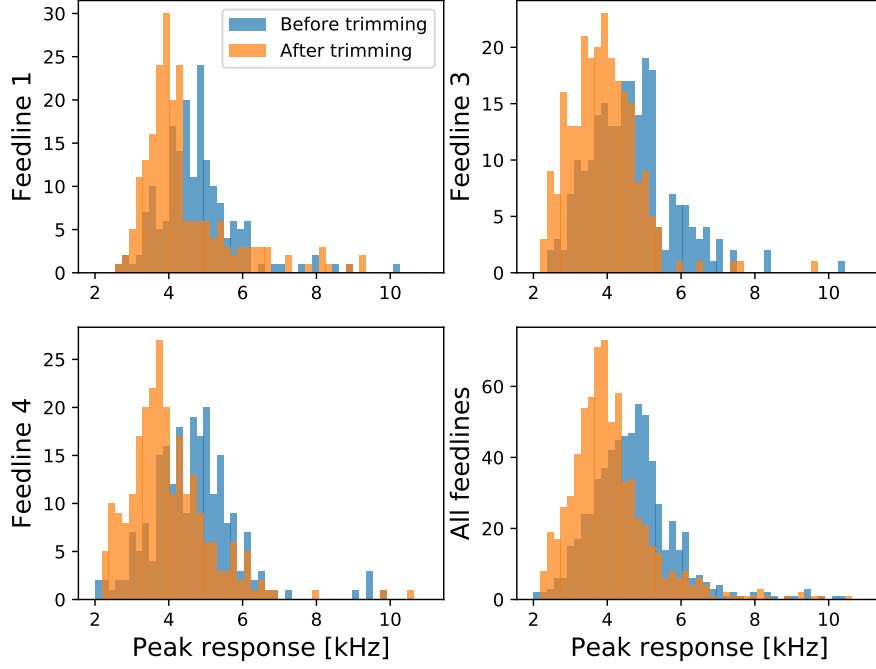


Figure 6.14: Histogram of peak responses of pixels before and after trimming.

properties after trimming is quite small, the decrease of Q_i cannot be explained by the change of optical properties of Al. Since the array was dominated by the blackbody radiation from other temperature stages, which depends on when the measurement is performed, we suggest this change of Q_i is mainly caused by the change of stage temperature between two cool-downs.

The peak response of resonators to the metal ball is also decreased from 5 kHz to 4 kHz after trimming, as shown in Fig. 6.14. This is consistent with the decrease of Q_i after trimming. Since this is measured in a different optical condition compared to the Q_i measurement, it is hard to evaluate the relation between the optical response and the Q_i quantitative.

6.6 Conclusion

We applied capacitor trimming technique on a 4-inch kilo-pixel array. The standard deviation of the resonance frequency difference between the measurement and design is decreased from 33 MHz to 2.5 MHz after trimming. The mapping yield is increased from 69 % to 76 %. Including the missing resonances due to readout board, the final yield is expected to be larger than 80 % compared to the initial fabrication yield 84 %. 23 resonances were broken during trimming process, which gives the trimming fabrication yield of 97 %. For the resonators measured before trimming, the trimming accuracy is $\sigma = 3.1 \times 10^{-4}$ ignoring the resonators which give anomalous responses. The loaded internal quality factor is decreased by 40 % after trimming, which cannot be explained by the change of film property. This decrease of Q_i might be caused by the temperature variation inside the cryostat and not directly related to the intrinsic Q_i . The final mapping yield is expected to be larger than 95 %, after improving the fabrication process and the film properties. The trimming process is proved to be scalable to telescope-ready arrays.

Chapter 7

Locating superconducting micro-resonators in darkness

7.1 Introduction

In Chapter 5 and 6, we used an optical mapping system, the sky simulator, to find the physical positions of resonators on the array. There are some limitations to apply this technique. First, all optical components like lenses and filters should be installed in the cryostat. This setup is not often available since people often test devices in dark, which is the easiest setup. Second, an optical mapping system is necessary. Such systems consist of a background and a source. To detect the source, the power of the source must be higher than the background. In our case this is realized using a cooled 50 K blackbody and a 300 K room temperature metal ball. Also it is necessary to synchronize the x-y stage data with the resonance response in the readout software, which increases the complexity. The NIST group used a LED mapper [91] inside the cryostat to find the resonance. Each LED is corresponding to each resonator. When the design is changed, the mapper should also be changed and re-fabricated. Therefore, the ideal method should be fitted in the dark measurement and can be easily extended to different designs. In this chapter, we introduce a method to reconstruct the focal plane in darkness. The basic idea of the method is to use the reflected phase information of the resonances, which encodes their relative position on the microwave feedline.

7.2 Reflected phase of a resonator

7.2.1 Theory

Compared to the transmission S21 in Eqn. 2.19, the reflected response of a resonator is expressed as

$$S_{11} = Ae^{-j2\pi\tau f} \frac{S_{11}^{max}}{1 + 2jQ_r(f - f_r)/f_r}, \quad (7.1)$$

where S_{11}^{max} is the maximum reflection coefficient. At the resonance point, where $f = f_r$, we have

$$S_{11} = Ae^{-j2\pi\tau f_r} S_{11}^{max} = Ce^{-j2\pi\tau f_r}, \quad (7.2)$$

where C is a complex scale factor. Therefore the effect of the delay time τ is just rotating the resonance point by an angle of $-2\pi\tau f_r$. For S21, this τ is constant for all resonators, since all the signals pass through the same length of cable. For S11, ideally only the resonant signals are reflected and the reflection happens at the physical positions of resonator. If there are only two resonators, as shown in Fig. 7.1(a), the two reflected signal should have a different microwave path $2d$. The corresponding phase difference is given by

$$\begin{aligned} \Delta\phi &= \angle(C_2 e^{-j2\pi\tau_2 f_{r2}}) - \angle(C_1 e^{-j2\pi\tau_1 f_{r1}}) \\ &= \angle C_2 - 2\pi\tau_2 f_{r2} - \angle C_1 + 2\pi\tau_1 f_{r1} \\ &= 2\pi(\tau_1 f_{r1} - \tau_2 f_{r2}) \\ &= 2\pi\left(\frac{D_1}{\lambda_1} - \frac{D_2}{\lambda_2}\right) \\ &= 2\pi\left(\frac{D_1}{\lambda_1} - \frac{D_1 + D_{12}}{\lambda_2}\right), \end{aligned} \quad (7.3)$$

where $D_{12} = 2d$ is the path difference between two resonators, d is the distance between two resonators and $\angle C_1 = \angle C_2$ is assumed. Considering a simple case that the two resonator have similar resonance frequency $f_{r1} = f_{r2}$ and the cable delay is

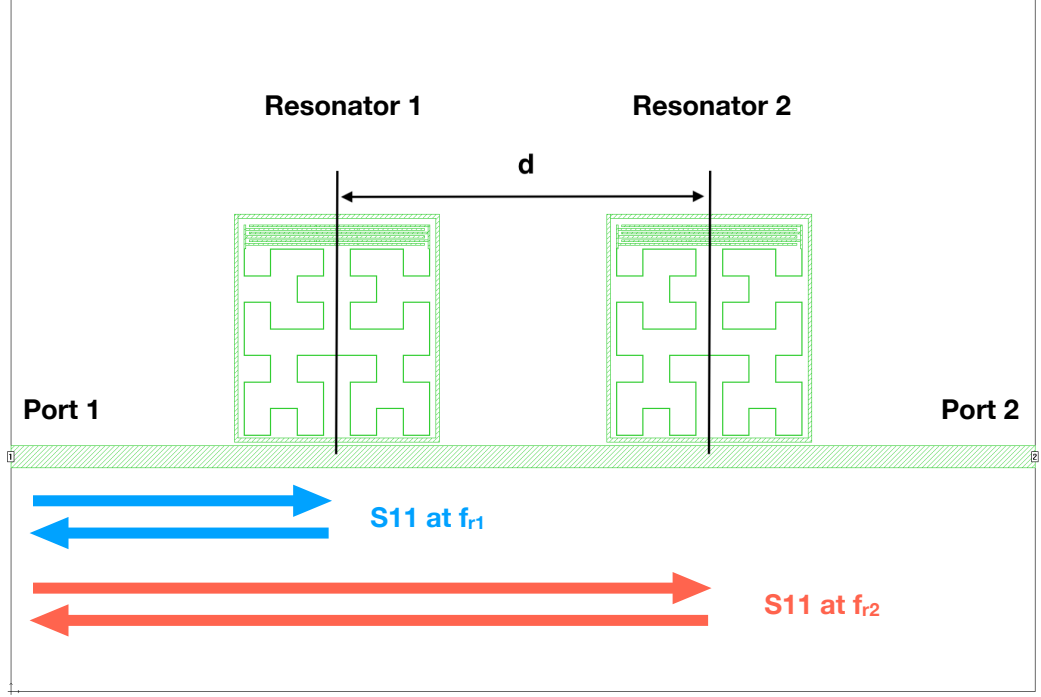


Figure 7.1: Configuration of simulation in Sonnet.

calibrated at resonator 1, this can be simplified to

$$\Delta\phi = 2\pi(\tau_1 - \tau_2)f_{r2} = 2\pi(\tau_1 - \tau_2)\frac{v}{\lambda} = 2\pi\frac{2d}{\lambda}, \quad (7.4)$$

where v is the speed of electromagnetic wave and λ is the wavelength at the resonance frequency.

7.3 Simulation

We performed several simulations in Sonnet to test Eqn. 7.4. Two resonators are placed with a distance d along a microstrip feedline, shown in Fig. 7.1. The resonance frequencies are 1.779 GHz and 1.785 GHz, which satisfies $f_{r1} \approx f_{r2}$. The distance d is simulated from 1.4 mm to 92.4 mm. The S11 of resonance 2 travelled $2d$ more than of resonance 1. Although the resonator has a size of 1 mm, the microwave path difference is still $2d$ assuming the reflection happens at the same position relative to

the resonator. In the simulation, we take the minimum point of S21 as the resonance point. Then the phase difference of this two resonances is calculated. The simulation results, shown in Fig. 7.2, exactly follows Eqn. 7.4. The fitted wavelength is 58.6 mm, compared with the calculated 60 mm. The simulation results suggest the using phase difference to determine the relative position is possible.

7.4 Measurement on resonators with known positions

First we test this method using the trimmed array mentioned in Chapter 5. After trimming, the resonance frequencies are well placed in the frequency domain and the positions of the resonances are already measured. The array has 112 resonators two-sided along the microstrip feedline. The array configuration is shown in Fig. 7.3. The pixel index is from 1 to 112 meaning the resonance frequency ranges from 2.415 GHz to 2.905 GHz.

The array is cooled down in dark to avoid the possible change of phase due to radiation. In the setup, attenuator, amplifier and isolator are all removed, so there is only coaxial cable connecting the array. Removing the attenuator increases the power of the reflected signal, which makes it easier to measure the reflected phase. To avoid the nonlinear effect, the input power should be decreased and therefore the signal-to-noise ratio is also decreased. The setup is shown in Fig. 7.3 and a VNA is used to measure the S-parameters.

The S11 and S21 are measured with -80 dBm readout power from VNA. The measured data are corrected using the cable delay correction function on the VNA. Therefore, we have a relative flat phase baseline shown in Fig. 7.5(b). Based on the transmission and reflection spectrum shown in Fig. 7.4, we could estimate that the cable loss is 3 dB for port 1 and 4 dB for port 2. The resonance frequencies are determined by the minimum points from S21, shown in 7.4. From the array configuration shown in Fig. 7.3, the calculated distance is shown in Fig. 7.5(a), where

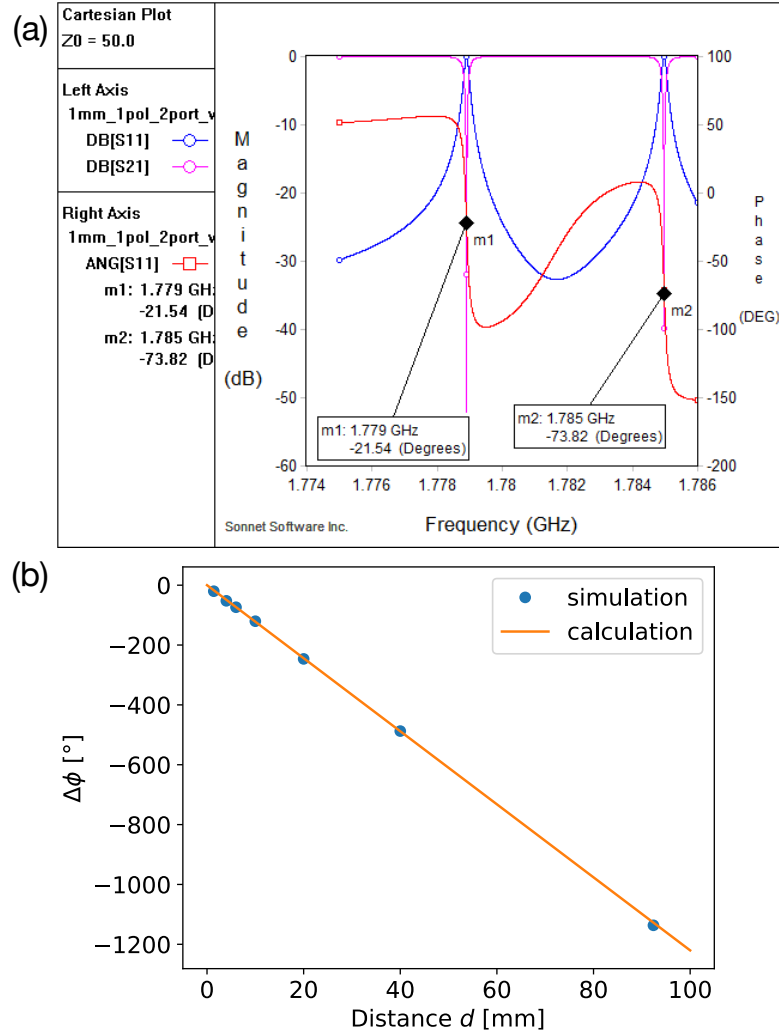


Figure 7.2: (a) Plot of the S11, S21 and the phase of S11 with $d = 4$ mm in Sonnet. The resonance point is determined by the minimum point of S21. The phase of S11 is plotted with the right axis. The two markers show the phase results at two resonance points. (b) The simulated phase difference is plotted as points by changing d . The line is fitted using Eqn. 7.4 with $\lambda = 58.6$ mm.

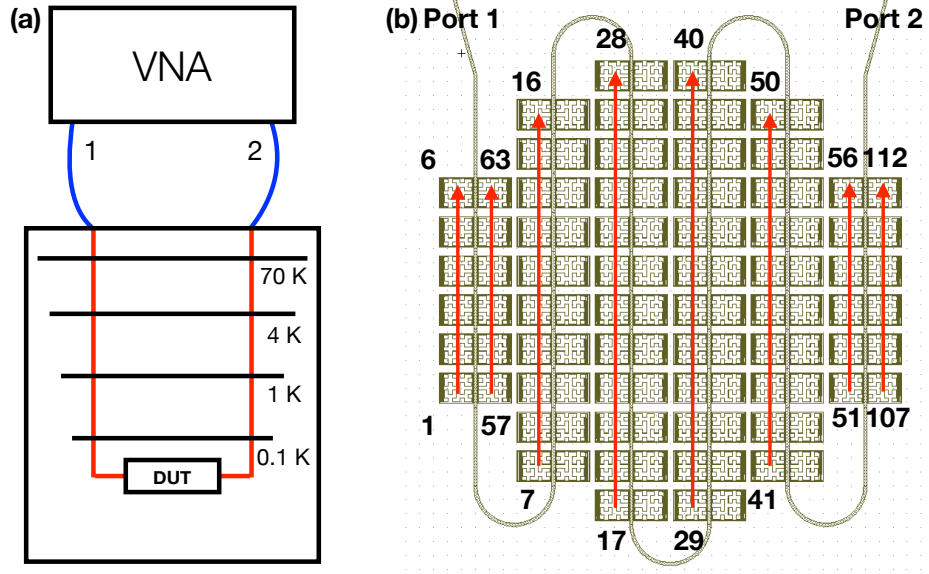


Figure 7.3: (a) The measurement setup. There is only coaxial cable between the device under test and the VNA. (b) The configuration of the array.

the first two pixels are set as 0 positions. The wavelength is given as 55 mm at 2 GHz. After removing the missing resonators, the phase difference is shown in Fig. 7.5(c). The on-resonances phase values are taken from the minimum points on S_{21} . We also fitted the resonances using I and Q data with the **Scraps** package [94]. The fitted resonance frequencies are almost the same with the ones determined from the S_{21} minimum except two resonators. The comparison between the calculated and measured phase are shown in Fig. 7.5.

In general, the measured phase values follow the calculated phase order. However, the current result cannot be used to determine the resonator positions. There are several problems. The first is that the expected phase difference between the resonator No.1 and No.7 are not the same as the calculation. This difference might be related with the curved microstrip line. The length between resonator No.1 and No.7 is about 15 mm, corresponding to $> 100^\circ$ phase difference in calculation. However, the measured phase difference is only 20° . The second problem is that the resonators No.6

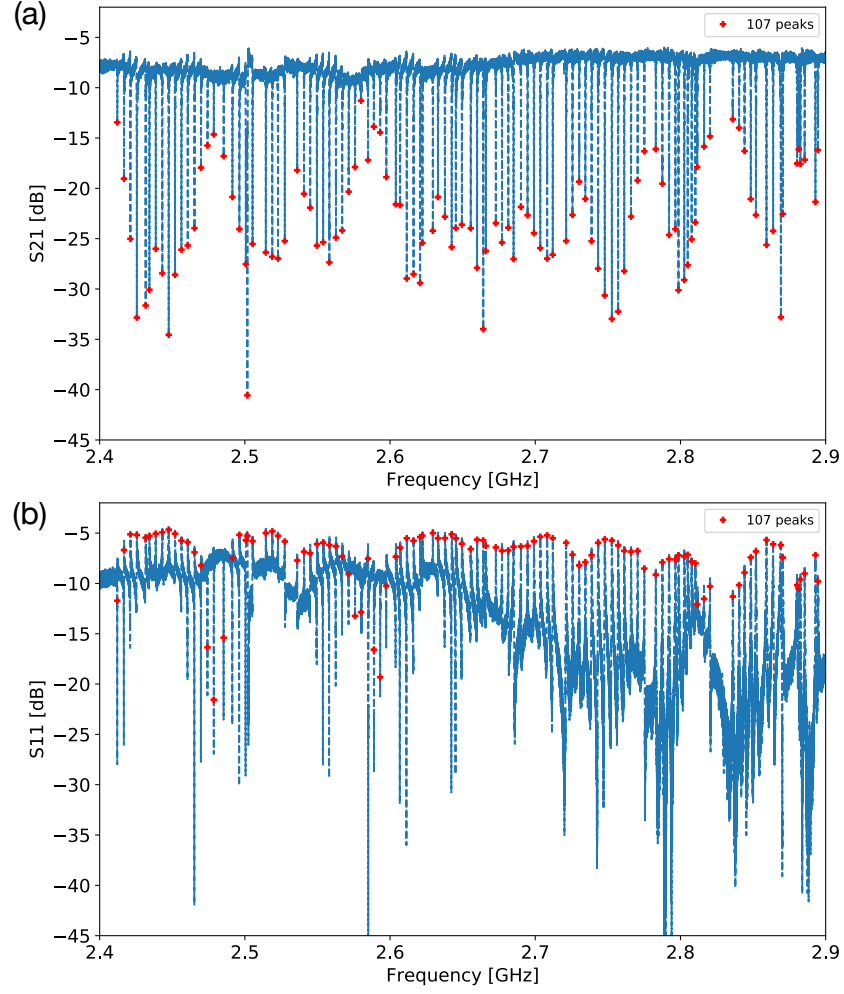


Figure 7.4: (a) The S21 result of the trimmed array. 107 peaks are found and shown in red points. (b) The S11 result of the trimmed array. The red points are the corresponding data where S21 has the minimum.

and No.63 do not have the same reflected phase value although they have the same physical position. This is caused by the frequency dependant phase delay and the resonance frequencies of the two resonators have a difference of 250 MHz. To evaluate the accurate physical position, a more accurate cable delay calibration should be considered for this two-sided design in the further experiment.

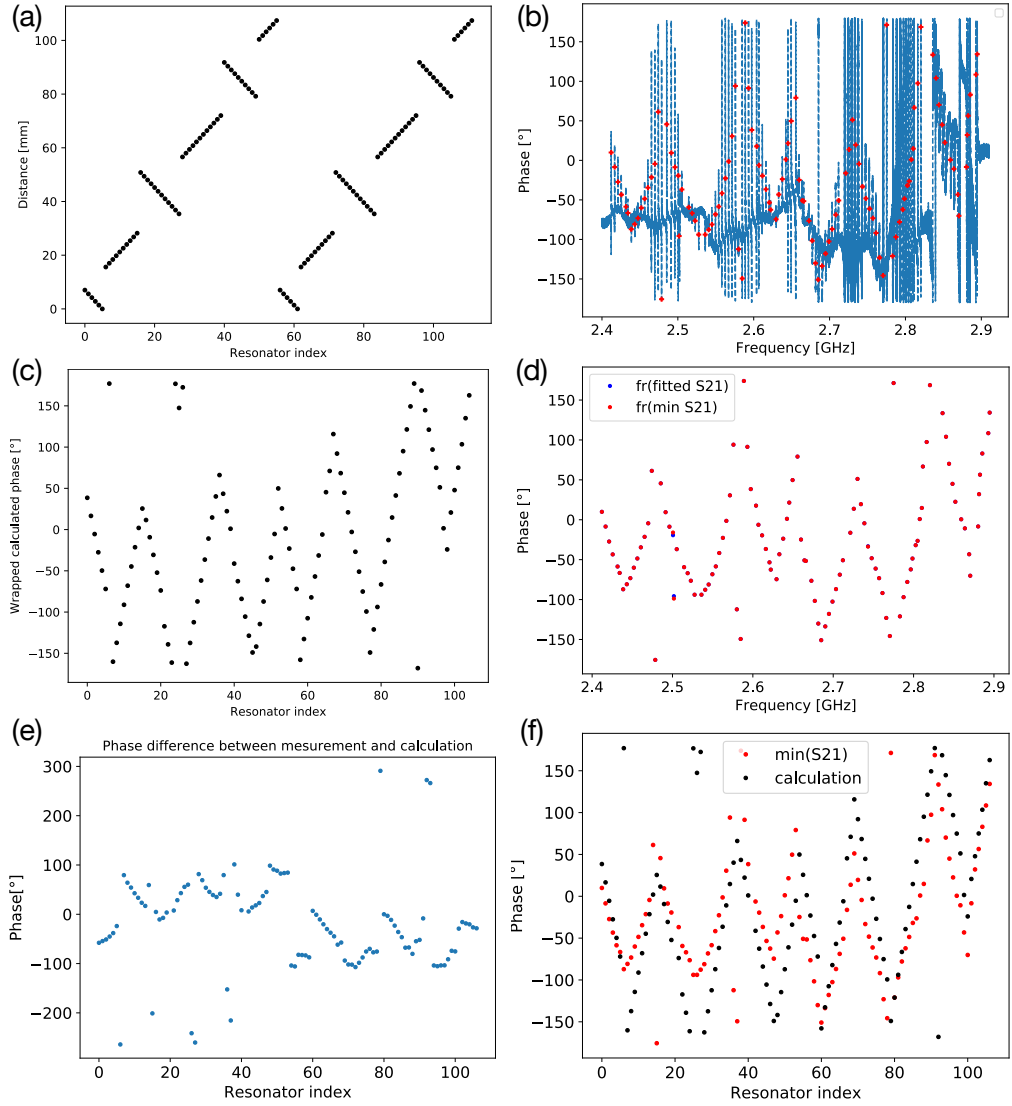


Figure 7.5: (a) The calculated distances of resonators relative to the first resonators, No.6 and No.63, shown in Fig. 7.3(b). (b) The phase of S11 with cable delay corrected. The red points are at the resonance frequencies, determined from the minimum points of S21, shown in Fig. 7.4. (c) The calculated phases from (a) using resonance frequencies derived from (b) with an offset. The wavelength used here is calculated as 55 mm at 2 GHz. (d) The phases at the resonance frequencies determined by the minimum values of S21 and fitting of the resonance curve. (e) The difference between the calculated and measured phases in (f). (f) Comparison of the calculation from (c) and measurement from (d).

7.5 Measurement on resonators with unknown positions

7.5.1 Array design

In the last section, we have seen the potential of this method to locate resonators, but to use the method we need to understand some other factors. Therefore we performed a measurement on a simple design. The design has a line of 16 resonators with pitch size 1.4 mm and frequency spacing 1.6 MHz, as shown in Fig. 7.6(c). The design frequency is from 1.9 GHz to 1.924 GHz. The resonator has the same design with as described in Chapter 4.

7.5.2 Measurement

The array is cooled down in dark. The full S-parameters are measured at 0.1 K. To have an accurate baseline calibration, we also measured the S-parameters at half T_c , about 0.6 K. The low temperature S11 and S22 are then normalized to the half T_c data. The frequency resolution is 5 kHz. Ideally there should be no reflection for the baseline when the impedance is perfectly matched. In our measurements, the reflected power is about -20 dB. When the measurement data are normalized to the half T_c data, the phase positions are normalized to where the reflection happened. The resonance frequencies are determined by the minimum points on S21. The S11 and S22 phases are plotted together with the on-resonance points, as shown in Fig. 7.6. The symmetry of on-resonance phases can be clearly seen but the average values of phases are not constant. The relation between S11 and S22 on-resonance phases should be a straight line if the positions are accurate. However, the points in Fig. 7.6 does not show a simple linear relation.

We first calculated the distances and phases for all resonators. Then we sorted the measured phase assuming the values are corresponding to the resonator positions. Since 15 out of 16 resonators are measured, we assume the second resonator is missing from the S11 phase. Therefore, we could calculate the resonance frequency deviation

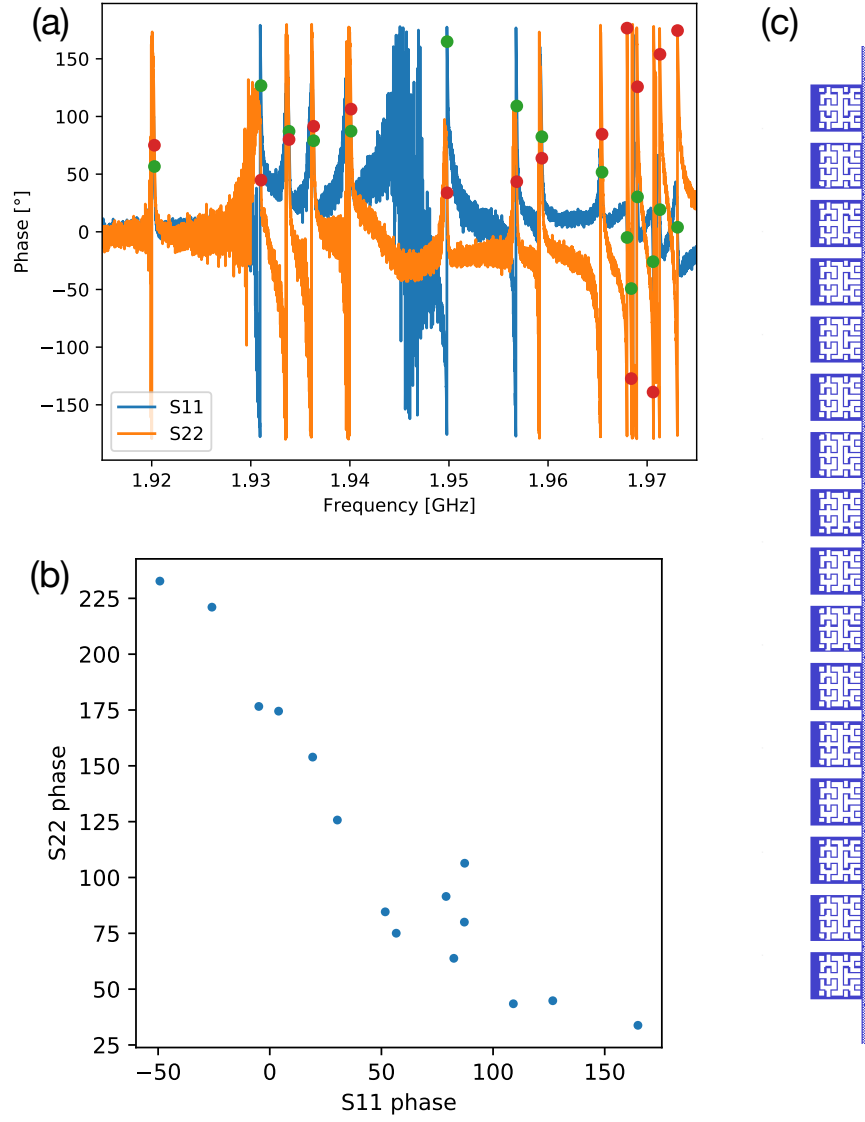


Figure 7.6: (a) The measured and calibrated phase results of S11 and S22. The dots show the phases at resonance frequencies. (b) The plot show S11 phase versus S22 phase at same resonance frequencies. (c) Design of 16 resonators.

for each resonator to test if the calculated positions are correct. The results in Fig. 7.7 show that the positions determined by sorted phase are not the same for S11 and S22, but the positions with the estimated resonator index from 10 to 15 are the same for both S11 and S22, which suggests the positions are consistent. For other resonators, the resonance frequency deviation does not have a smooth profile, which suggests the positions are not all precise.

From Eqn. 7.3, the measured phase difference reflects the relative distance difference between resonators. Therefore, it is crucial to determine the start position D_1 . In our analysis, the S-parameters are calibrated from the half- T_c data, so the D_1 is determined from the baseline of half- T_c S-parameters. Since we do not know where the baseline of S-parameter is reflected, the current phase data may include extra length instead of the pure distance $2d$ between resonators. To locate resonators precisely, the position of where D_1 is determined is necessary.

Also we suggest that currently the results are limited by the phase accuracy. Compared to simulation, the measured phase is much more sensitive to frequency, with a maximum value of $12^\circ/\text{kHz}$. Since the measured frequency spacing is 5 kHz and the calculated phase difference is only 17.5° , a higher frequency resolution is needed to determine the reflected phase.

To have the resonator positions precisely, we also need the wavelength information. From the measurement, we could add two extra resonators: one at the beginning and the other one the end of the resonators. These two resonators have unique resonance frequencies, which could be identified directly and the positions are known. From the resonance data and the distance between two resonators, we could estimate the wavelength in the feedline using Eqn. 7.3. This measured wavelength could also help to determine where the calibration of phase happens.

7.6 Conclusion

We measured the reflected phases for two designs. One has 112 resonators with known positions and the other one has 16 resonators with unknown positions. Both results

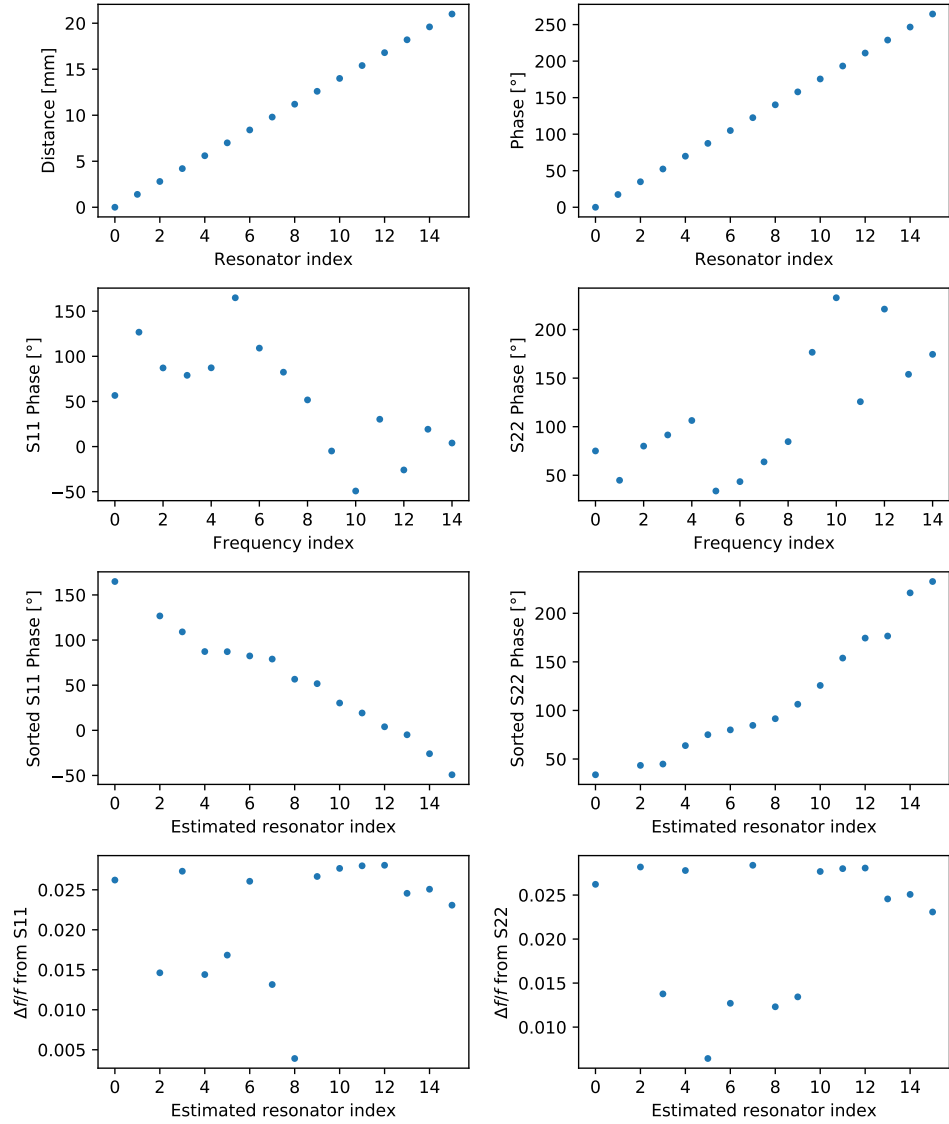


Figure 7.7: (a) The designed distance relative to the first resonator, which has the lowest resonance frequency in design. (b) The corresponding phase difference calculated from (a). (c) The S11 on-resonance phases. (d) The S22 on-resonance phases. (e) The sorted S11 on-resonance phases. (f) The sorted S22 on-resonance phases. (g) The calculated resonance frequency deviation with positions determined from S11 phase. (g) The calculated resonance frequency deviation with positions determined from S22 phase.

show the possibility to locate resonators using reflected phase. Since the phase is very sensitive to frequency around resonance points, the current 5 kHz frequency accuracy is not enough. A measurement with 1 kHz frequency accuracy should improve the result. Also it would be possible to achieve a high accurate phase by fitting S_{11} and S_{22} .

Chapter 8

Conclusions

In this chapter, I present a brief summary of the research presented in this thesis and discuss possible future developments.

Chapter 3 presented a detailed analysis of the optical performance of LEKID arrays, using the NIKA2 260 GHz band array as a test case. This analysis directly connects the simulations with the measured optical response of LEKIDs. The FTS measurements match with simulations. Although the Hilbert shape inductor is designed for dual-polarization detection, the simulation shows that the current design has a 30 % difference in absorption efficiency for the two polarizations. The NIKA2 260 GHz band is not affected by this since we use this design for single polarization only. We also found that, for Pol 1, the absorption efficiency of the inductor is close to 100 %, normalized to its physical size. This suggests that simplifying the inductor as a pure resistive sheet is not accurate. The capacitance of the Hilbert curve should also be considered. By using high- T_c superconductors as frame and feedline, the absorption efficiency could be further improved. This analysis could be used to optimize the focal plane layout in terms of optical response. Further study on the relation between the effective absorbing area and the inductor size by experiments could benefit high-angular resolution pixel design.

To achieve the diffraction limit of the 30-m telescope, we studied a small pixel design for 260 GHz band in Chapter 4. The inductor size is decreased from 1.6 mm to 1 mm, increasing the angular resolution from 10.3'' to 9.4'' from calculation. The optical measurements show that this small pixel design could increase the on-telescope

resolution from 10.9" to 10.2". Also we developed a compact layout with ~ 2400 pixels on the NIKA2 focal plane using this small-pixel design. The electric crosstalk is well simulated and limited to 20 kHz. Future developments may focus on decreasing the inductor size while keeping the filling factor.

In Chapter 5 and 6, we studied the capacitor trimming technique on our bare LEKIDs design. We first applied trimming on a 1-inch test array. The yield is increased from 71 % to 97 % determined by optical mapping. The final yield is limited by fabrication defects. Before trimming the resonance frequency deviation is caused by the variation of the inductor width and capacitor finger width. Then we designed a new 4-inch array for NIKA2 260 GHz band and applied trimming on it. The optical yield is increased from 69 % to 76 %, and is mainly limited by the initial fabrication process and the readout system. Only 3 % of resonators were broken during trimming process. This suggests that the final yield after trimming could easily achieve 90 %. For this 4-inch array, the resonance frequency deviation is mainly caused by the variation of film thickness and mask accuracy. However, there is also another factor causing extra deviation. This might be related with the thickness variation of photoresist in the initial fabrication, since the gap between the mask and the resist can introduce width variation during contact lithography. Further studies on the changes of internal quality factor, noise and film properties before and after trimming would benefit future balloon and space projects.

In the trimming process, we used a optical beam mapper to located the resonances to resonators. This requires not only a beam mapper but also a cryostat with well established optical system, which are necessary for millimeter-wave detectors. However, with a beam mapper, we need multiple cool-downs to characterize the effect of trimming on resonators in dark. In Chapter 6 we study a novel method to locate resonators in darkness based on the reflected phase information. We established the method and confirmed it through simulation. The measurements show a possibility to locate resonators using this method. The current difficulty is to determine the on-resonance phase, which is highly sensitive to resonance frequency. Further developments including directly fitting the reflected I and Q data and improving

measurement accuracy should be considered.

In conclusion, we have a better understanding of the optical response of bare LEKID arrays and we also studied the improvement of angular resolution and resonator yield. Based on these developments, a high-angular resolution LEKID array with $> 90\%$ optical yield and ~ 2400 pixels could be achievable for NIKA2 260 GHz band.

Appendix A

Fabrication procedure

All the fabrication work in this thesis has been done in the IRAM cleanroom.

A.1 Wafer preparation

We used high-resistivity ($> 5 \text{ k}\Omega \text{ cm}$) $250 \mu\text{m}$ thick silicon substrates for all fabrications. The thickness variation of our substrate is $\pm 10 \mu\text{m}$. Before fabrication, substrates are cleaned in acetone and isopropyl alcohol using ultrasonic cleaner for 5 min each.

A.2 Deposition of Al device layer

The PLASSYS MP500S system is used for plasma cleaning and electron-beam evaporation. Before Al deposition, we first clean our substrate using RF plasma cleaning with Ar pressure of 1.5 Pa and power of 100 W for 1 min. This process etches part of the oxidation layer on the surface of substrate. We have found that a strong Ar plasma cleaning process can decrease the internal quality factor of LEKID in dark, which could be caused by the increased surface roughness. After cleaning, the chamber is pumped down to a base pressure of 3×10^{-8} Torr, after which 18 nm of Al is evaporated using e-beam evaporation from a high purity target at a speed of 0.5 nm/s. Film thickness and evaporation speed are monitored with a quartz crystal oscillator. The film properties are listed in Table A.1.

Table A.1: Properties of evaporated Al film. Credit: Gregoire Coiffard

Thickness	ρ_{4K} [$\mu\Omega$ cm]	R_{\square} at 4 K	RRR
10 nm	9.9	9.91	1.5
20 nm	3.9	1.95	2.0
25 nm	3.8	1.52	2.2
40 nm	2.1	0.52	2.8
60 nm	2.0	0.33	2.9
100 nm	1.3	0.13	3.9
150 nm	1.0	0.07	4.7
300 nm	0.7	0.02	6.3

A.3 Deposition of backside aluminum

After the front-side deposition, a layer of 200 nm Al is deposited on the backside of substrate after Ar plasma cleaning. For cleaning, we use Ar pressure of 2 Pa and power of 140 W for 1 min. The DC magnetron sputtering process is done in the PLASSYS SCM450 system with a speed of 25 nm/min.

A.4 Pattern definition

Patterning of the front side is done using contact mask alignment. AZ5214 is used as a positive resist. The resist is spun on the substrate with thickness of 1.6 μ m and then pre-baked for 60 s at 90 °C. The exposure is done by illuminating 444 nm UV light for 4 s. Then the resist is developed in MF26 for 30 s. After blow-drying, we use wet-etching to pattern the design in the Al film using Al Etchant Type-D. The etching speed is 20 nm/min, however, the Al oxidation layer can significantly increase the etching time. Usually the etching time is about 2 min.

A.5 Pattern re-definition for trimming

We modified the process in A.4 for our trimming process. The problem with developer MF26 is that it attacks the aluminum film during development. To minimize

this effect, we used AR-U4040 positive resist together with developer AR300-35 for trimming. Compared with MF26, AR300-35 etches aluminum quite slowly and during 30 s development this can be negligible. After development, there is a thin layer of resist residue on the surface of wafer. This thin layer can protect the aluminum from etching, so we used O_2 plasma ashing for 30 s at power of 100 W and pressure of 40 Pa to remove this resist residue. Then the wafer is wet-etched in Al Etchant Type-D for 2 min.

Appendix B

Martin-Puplett Interferometer

The Martin-Puplett Interferometer (MPI) working principle is analogue to that of the Michelson interferometer: an input optical signal is split in two arms, one fixed and one of variable length. This introduces an optical path difference between the light travelling on the two arms that, once recombined, will undergo an interference, which depends on its frequency and on the length of the moving arm. This effect forms our interferogram, whose Fourier Transform makes it possible to measure the absorbed power as a function of frequency.

In practice, an MPI is based on wire grid polarizers, shown in Fig. B.1. At the input, a first polarizer is mounted at 45° inclination between two blackbody sources at different temperatures, T_1 and T_2 . This signal then reaches the central polarizer, where it is split in the two different arms. The mirrors at the end of the arms are roof top mirrors, introducing a 90° shift in the polarization of the signal. Thus, when reaching once more the central polarizer, the polarization that was reflected at the first interaction is now transmitted, and vice versa. The output signal is the sum of this two polarizations. A last wire grid on the output of the MPI makes it possible to detect the interferogram. One can show that, using the appropriate inclination of the various wire grids, the expected signal after the output wire grid is given by

$$P_\nu(\delta x) = \frac{1}{2} (B_\nu(T_1) + B_\nu(T_2)) + \frac{1}{2} (B_\nu(T_1) - B_\nu(T_2)) \cos(2\pi\nu \cdot 2\delta x/c). \quad (\text{B.1})$$

$P_\nu(\delta x)$ is the amount of output power at frequency ν when the moving mirror is at a distance δx from the ZPD position, and $B_\nu(T)$ is the brilliance of a blackbody at temperature T . The first term can be removed by making the first wire grid rotate around its axis and applying a lock-in technique to get the LEKID signal. The observed interferogram, $I(\delta x)$, will be given by

$$I(\delta x) = \int_{\nu_{min}}^{\nu_{max}} P_\nu(\delta x) A_\nu d\nu \quad (\text{B.2})$$

where A_ν is the absorption of the considered LEKID. The Fourier Transform is applied to the interferogram to finally get A_ν .

The maximum displacement of the moving arm, Δx , determines the resolution of the measured spectrum, whereas the smallest step by which the moving mirror can be controlled impacts the maximum detectable frequency. In our system we usually span about 20 mm around the ZPD position, so the resolution is of ~ 3 GHz. The resolution of the stepper motor is $\sim 20 \mu\text{m}$, meaning that the spectrum can be measured in principle up to a few THz.

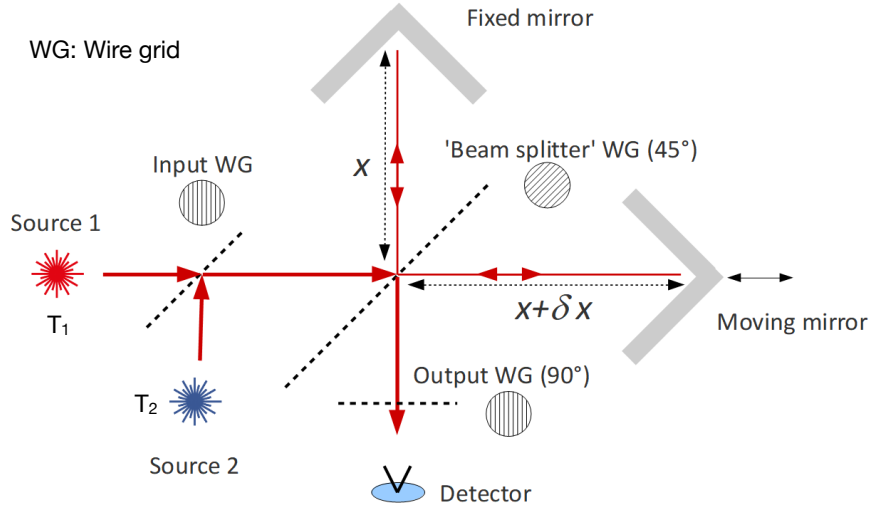


Figure B.1: The setup of our MPI. 300 K and 77 K blackbodies are used as hot and cold sources, respectively. Two polarizations can be measured by changing the direction of the input and output wire grids.

Appendix C

Data readout

We used the NIKEL readout system for our in-lab measurements[28]. The FPGA chip samples the data at ~ 1000 Hz and then averages the data. The raw data I and Q after averaging is generated and saved by the NIKEL system at ~ 23.8 Hz. A detail discussion of the readout scheme is included in [26].

For a pixel with resonance frequency f_0 , two frequency tones f_+ and f_- , are generated for each resonance. These two tones are separated by δf , so we have

$$f_+ = f_0 + \frac{\delta f}{2} \quad (\text{C.1})$$

$$f_- = f_0 - \frac{\delta f}{2}. \quad (\text{C.2})$$

The δf can be set manually depending on the width of resonances and in our case we have $\delta f = 5$ kHz. The raw data we have at time point t_0 are the IQ values at f_+ and f_- , $(I_{t_0}(f_+), Q_{t_0}(f_+))$ and $(I_{t_0}(f_-), Q_{t_0}(f_-))$. Then we use these two data to calculated the IQ values (I_{t_0}, Q_{t_0}) at f_0 :

$$(I_{t_0}, Q_{t_0}) = \left(\frac{I_{t_0}(f_+) + I_{t_0}(f_-)}{2}, \frac{Q_{t_0}(f_+) + Q_{t_0}(f_-)}{2} \right). \quad (\text{C.3})$$

The difference of IQ between f_+ and f_- is given by

$$(dI_{t_0}, dQ_{t_0}) = (I_{t_0}(f_+) - I_{t_0}(f_-), Q_{t_0}(f_+) - Q_{t_0}(f_-)). \quad (\text{C.4})$$

The relation between the difference of IQ and frequency can be calculated as

$$\left(\frac{dI_{t_0}}{df}, \frac{dQ_{t_0}}{df} \right) = \left(\frac{I_{t_0}(f_+) - I_{t_0}(f_-)}{f_+ - f_-}, \frac{Q_{t_0}(f_+) - Q_{t_0}(f_-)}{f_+ - f_-} \right) = \frac{(dI_{t_0}, dQ_{t_0})}{\delta f}. \quad (\text{C.5})$$

The response of pixel is recorded as

$$(\Delta I_{t_0}, \Delta Q_{t_0}) = (I_{t_0} - I_{t_0-1}, Q_{t_0} - Q_{t_0-1}) \quad (\text{C.6})$$

Since $(\Delta I_{t_0}, \Delta Q_{t_0})$ is not always parallel to the reference vector $|(dI_{t_0}, dQ_{t_0})|$, we project the vector $(\Delta I_{t_0}, \Delta Q_{t_0})$ to (dI_{t_0}, dQ_{t_0})

$$\text{RFdIdQ} = \frac{(\Delta I_{t_0}, \Delta Q_{t_0}) (dI_{t_0}, dQ_{t_0})}{|(dI_{t_0}, dQ_{t_0})|^2} \delta f. \quad (\text{C.7})$$

Typically this difference is smaller than 10° , so the error caused by this projection method is less than 2% for faint sources [95]. This is valid for our in-lab test, which has a maximum response of 50 kHz. For bright sources, a polynomial relation is assumed between $(\Delta I_{t_0}, \Delta Q_{t_0})$ and frequency shift.

Bibliography

- [1] Arno A Penzias and Robert Woodrow Wilson. A Measurement of excess antenna temperature at 4080-Mc/s. *Astrophys.J.*, 142:419–421, 1965.
- [2] Robert H Dicke, P James E Peebles, Peter G Roll, and David T Wilkinson. Cosmic black-body radiation. *The Astrophysical Journal*, 142:414–419, 1965.
- [3] DJ Fixsen, ES Cheng, JM Gales, John C Mather, RA Shafer, and EL Wright. The cosmic microwave background spectrum from the full coBE* FIRAS data set. *The Astrophysical Journal*, 473(2):576, 1996.
- [4] George F Smoot, Charles L Bennett, A Kogut, EL Wright, J Aymon, NW Boggess, ES Cheng, G De Amici, S Gulkis, MG Hauser, et al. Structure in the COBE differential microwave radiometer first-year maps. *The Astrophysical Journal*, 396:L1–L5, 1992.
- [5] Gary Hinshaw, D Larson, Eiichiro Komatsu, David N Spergel, CLaa Bennett, Joanna Dunkley, MR Nolte, M Halpern, RS Hill, N Odegard, et al. Nine-year Wilkinson Microwave Anisotropy Probe (WMAP) observations: cosmological parameter results. *The Astrophysical Journal Supplement Series*, 208(2):19, 2013.
- [6] John Michael Kovac, EM Leitch, C Pryke, JE Carlstrom, NW Halverson, and WL Holzappel. Detection of polarization in the cosmic microwave background using DASI. *Nature*, 420(6917):772, 2002.
- [7] P Ade and others. Detection of B-Mode Polarization at Degree Angular Scales by BICEP2. *Physical Review Letters*, 112(24):241101, 2014.

- [8] D Hanson, S Hoover, A Crites, PAR Ade, KA Aird, JE Austermann, JA Beall, AN Bender, BA Benson, LE Bleem, et al. Detection of b-mode polarization in the cosmic microwave background with data from the south pole telescope. *Physical Review Letters*, 111(14):141301, 2013.
- [9] PAR Ade, Y Akiba, AE Anthony, K Arnold, M Atlas, D Barron, D Boettger, J Borrill, S Chapman, Y Chinone, et al. A measurement of the cosmic microwave background b-mode polarization power spectrum at sub-degree scales with polarbear. *The Astrophysical Journal*, 794(2):171, 2014.
- [10] Tomotake Matsumura, Yoshiki Akiba, K Arnold, J Borrill, R Chendra, Yuji Chinone, A Cukierman, T de Haan, M Dobbs, A Dominjon, et al. Litebird: mission overview and focal plane layout. *Journal of Low Temperature Physics*, 184(3-4):824–831, 2016.
- [11] Howard Hui, PAR Ade, Z Ahmed, RW Aikin, KD Alexander, D Barkats, SJ Benton, CA Bischoff, JJ Bock, R Bowens-Rubin, et al. Bicep array: a multi-frequency degree-scale cmb polarimeter. In *Millimeter, Submillimeter, and Far-Infrared Detectors and Instrumentation for Astronomy IX*, volume 10708, page 1070807. International Society for Optics and Photonics, 2018.
- [12] BA Benson, PAR Ade, Z Ahmed, SW Allen, K Arnold, JE Austermann, AN Bender, LE Bleem, JE Carlstrom, CL Chang, et al. Spt-3g: a next-generation cosmic microwave background polarization experiment on the south pole telescope. In *Millimeter, Submillimeter, and Far-Infrared Detectors and Instrumentation for Astronomy VII*, volume 9153, page 91531P. International Society for Optics and Photonics, 2014.
- [13] Peter Ade, James Aguirre, Zeeshan Ahmed, Simone Aiola, Aamir Ali, David Alonso, Marcelo A Alvarez, Kam Arnold, Peter Ashton, Jason Austermann, et al. The simons observatory: science goals and forecasts. *Journal of Cosmology and Astroparticle Physics*, 2019(02):056, 2019.

- [14] Maximilian H Abitbol, Zeeshan Ahmed, Darcy Barron, Ritoban Basu Thakur, Amy N Bender, Bradford A Benson, Colin A Bischoff, Sean A Bryan, John E Carlstrom, Clarence L Chang, et al. Cmb-s4 technology book. *arXiv preprint arXiv:1706.02464*, 2017.
- [15] Ya B Zeldovich and RA Sunyaev. The interaction of matter and radiation in a hot-model universe. *Astrophysics and Space Science*, 4(3):301–316, 1969.
- [16] Rashid A Sunyaev and Ya B Zeldovich. Small-scale fluctuations of relic radiation. *Astrophysics and Space Science*, 7(1):3–19, 1970.
- [17] John E Carlstrom, Gilbert P Holder, and Erik D Reese. Cosmology with the sunyaev-zel’dovich effect. *Annual Review of Astronomy and Astrophysics*, 40(1):643–680, 2002.
- [18] PAR Ade, N Aghanim, M Arnaud, M Ashdown, J Aumont, C Baccigalupi, AJ Banday, RB Barreiro, R Barrena, JG Bartlett, et al. Planck 2015 results-xxvii. the second planck catalogue of sunyaev-zeldovich sources. *Astronomy & Astrophysics*, 594:A27, 2016.
- [19] Jonathan L Sievers, Renée A Hlozek, Michael R Nolta, Viviana Acquaviva, Graeme E Addison, Peter AR Ade, Paula Aguirre, Mandana Amiri, John William Appel, L Felipe Barrientos, et al. The atacama cosmology telescope: Cosmological parameters from three seasons of data. *Journal of Cosmology and Astroparticle Physics*, 2013(10):060, 2013.
- [20] LE Bleem, B Stalder, T De Haan, KA Aird, SW Allen, DE Applegate, Matthew LN Ashby, Mea Bautz, Matthew Bayliss, BA Benson, et al. Galaxy clusters discovered via the sunyaev-zel’dovich effect in the 2500-square-degree spt-sz survey. *The Astrophysical Journal Supplement Series*, 216(2):27, 2015.
- [21] R Adam, B Comis, JF Macías-Pérez, A Adane, P Ade, P André, A Beelen, B Belier, A Benoît, Aurelien Bideaud, et al. First observation of the thermal

- sunyaev-zel'dovich effect with kinetic inductance detectors. *Astronomy & Astrophysics*, 569:A66, 2014.
- [22] F Ruppin, F Mayet, GW Pratt, R Adam, P Ade, P André, M Arnaud, H Aussel, I Bartalucci, A Beelen, et al. First sunyaev–zel'dovich mapping with the nika2 camera: Implication of cluster substructures for the pressure profile and mass estimate. *Astronomy & Astrophysics*, 615:A112, 2018.
- [23] Suzanne Staggs, Jo Dunkley, and Lyman Page. Recent discoveries from the cosmic microwave background: a review of recent progress. *Reports on Progress in Physics*, 81(4):044901, 2018.
- [24] Daniel J Eisenstein, David H Weinberg, Eric Agol, Hiroaki Aihara, Carlos Allende Prieto, Scott F Anderson, James A Arns, Éric Aubourg, Stephen Bailey, Eduardo Balbinot, et al. Sdss-iii: Massive spectroscopic surveys of the distant universe, the milky way, and extra-solar planetary systems. *The Astronomical Journal*, 142(3):72, 2011.
- [25] A Bracco, P Palmeirim, Ph André, R Adam, P Ade, A Bacmann, A Beelen, A Benoît, A Bideaud, N Billot, et al. Probing changes of dust properties along a chain of solar-type prestellar and protostellar cores in taurus with nika. *Astronomy & Astrophysics*, 604:A52, 2017.
- [26] M Calvo, A Benoît, A Catalano, J Goupy, A Monfardini, N Ponthieu, E Barria, G Bres, M Grollier, G Garde, J P Leggeri, G Pont, S Triqueneaux, R Adam, O Bourrion, J F Macías-Pérez, M Rebolo, J P Scordilis, D Tourres, A Adane, G Coiffard, S Leclercq, F X Désert, S Doyle, P Mauskopf, C Tucker, P Ade, P André, A Beelen, B Belier, A Bideaud, N Billot, B Comis, A D'Addabbo, C Kramer, J Martino, F Mayet, F Pajot, E Pascale, L Perotto, V Revéret, A Ritacco, L Rodriguez, G Savini, K Schuster, A Sievers, and R Zylka. The NIKA2 Instrument, A Dual-Band Kilopixel KID Array for Millimetric Astronomy. *Journal of Low Temperature Physics*, 184(3-4):816–823, March 2016.

- [27] Remi Adam, Amar Adane, PAR Ade, Philippe André, Aina Andrianasolo, Herve Aussel, Alexandre Beelen, Alain Benoit, Aurelien Bideaud, Nicolas Billot, et al. The nika2 large-field-of-view millimetre continuum camera for the 30 m iram telescope. *Astronomy & Astrophysics*, 609:A115, 2018.
- [28] O Bourrion, A Benoit, JL Bouly, J Bouvier, G Bosson, M Calvo, A Catalano, J Goupy, C Li, JF Macías-Pérez, et al. Nikel_lamc: readout electronics for the nika2 experiment. *Journal of Instrumentation*, 11(11):P11001, 2016.
- [29] Heike Kamerlingh Onnes. The disappearance of the resistivity of mercury. *Comm. Leiden*, 122:2, 1911.
- [30] John Bardeen, Leon N Cooper, and John Robert Schrieffer. Theory of superconductivity. *Physical review*, 108(5):1175, 1957.
- [31] Michael Tinkham. *Introduction to superconductivity*. Courier Corporation, 2004.
- [32] P J De Visser, J J A Baselmans, J Bueno, N Llombart, and T M Klapwijk. Fluctuations in the electron system of a superconductor exposed to a photon flux. *Nature Communications*, 5:3130–3130, December 2013.
- [33] D C Mattis and J Bardeen. Theory of the Anomalous Skin Effect in Normal and Superconducting Metals. *Physical Review*, 111(2):412–417, July 1958.
- [34] Rami BARENDS. *Photon-detecting Superconducting Resonators*. PhD thesis, 2009.
- [35] Richard L Kautz. Picosecond pulses on superconducting striplines. *Journal of Applied Physics*, 49(1):308–314, 1978.
- [36] Henry G Leduc, Bruce Bumble, Peter K Day, Byeong Ho Eom, Jiansong Gao, Sunil Golwala, Benjamin A Mazin, Sean McHugh, Andrew Merrill, David C Moore, Omid Noroozian, Anthony D Turner, and Jonas Zmuidzinas. Titanium nitride films for ultrasensitive microresonator detectors. *Applied Physics Letters*, 97(1):102509, September 2010.

- [37] Peter K Day, Henry G LeDuc, Benjamin A Mazin, Anastasios Vayonakis, and Jonas Zmuidzinas. A broadband superconducting detector suitable for use in large arrays. *Nature*, 425(6960):817, 2003.
- [38] J J A Baselmans. Kinetic Inductance Detectors. *Journal of Low Temperature Physics*, 167(3-4):292–304, May 2012.
- [39] Jonas Zmuidzinas. Superconducting Microresonators: Physics and Applications. *Annual Review of Condensed Matter Physics*, 3(1):169–214, 2012.
- [40] S Doyle, P Mauskopf, J Naylor, A Porch, and C Duncombe. Lumped Element Kinetic Inductance Detectors. *Journal of Low Temperature Physics*, 151(1):530–536, April 2008.
- [41] R Barends, S van Vliet, J J A Baselmans, S J C Yates, J R Gao, and T M Klapwijk. Enhancement of quasiparticle recombination in Ta and Al superconductors by implantation of magnetic and nonmagnetic atoms. *Physical Review B*, 79(2):020509, January 2009.
- [42] Anthony Megrant, Charles Neill, Rami Barends, Ben Chiaro, Yu Chen, Ludwig Feigl, Julian Kelly, Erik Lucero, Matteo Mariantoni, Peter JJ O’Malley, et al. Planar superconducting resonators with internal quality factors above one million. *Applied Physics Letters*, 100(11):113510, 2012.
- [43] Agnes Dominjon, Masakazu Sekine, Kenichi Karatsu, Takashi Noguchi, Yutaro Sekimoto, Shibo Shu, Shigeyuchi Sekiguchi, and Tom Nitta. Study of Superconducting Bilayer for Microwave Kinetic Inductance Detectors for Astrophysics. *IEEE Transactions on Applied Superconductivity*, 26(3):1–6, 2016.
- [44] Carolyn T Earnest, Jérémy H Béjanin, Thomas G McConkey, Evan A Peters, Andreas Korinek, Hui Yuan, and Matteo Mariantoni. Substrate surface engineering for high-quality silicon/aluminum superconducting resonators. *Superconductor Science and Technology*, 31(12):125013, 2018.

- [45] Jiansong Gao, Miguel Daal, Anastasios Vayonakis, Shwetank Kumar, Jonas Zmuidzinas, Bernard Sadoulet, Benjamin A Mazin, Peter K Day, and Henry G Leduc. Experimental evidence for a surface distribution of two-level systems in superconducting lithographed microwave resonators. *Applied Physics Letters*, 92(1):152505, April 2008.
- [46] H Wang, M Hofheinz, J Wenner, M Ansmann, R C Bialczak, M Lenander, Erik Lucero, M Neeley, A D O’Connell, D Sank, M Weides, A N Cleland, and John M Martinis. Improving the coherence time of superconducting coplanar resonators. *Applied Physics Letters*, 95(23):233508, December 2009.
- [47] Omid Noroozian. Superconducting Microwave Resonator Arrays for Submillimeter/Far-Infrared Imaging. pages 1–189, October 2013.
- [48] P J De Visser. *Quasiparticle dynamics in aluminium superconducting microwave resonators*. PhD thesis, TU Delft, 2014.
- [49] T Guruswamy, DJ Goldie, and S Withington. Quasiparticle generation efficiency in superconducting thin films. *Superconductor Science and Technology*, 27(5):055012, 2014.
- [50] A V Sergeev, V V Mitin, and B S Karasik. Ultrasensitive hot-electron kinetic-inductance detectors operating well below the superconducting transition. *Applied Physics Letters*, 80(5):817, February 2002.
- [51] Daniel Flanigan, Heather McCarrick, Glenn Jones, Bradley R Johnson, Maximilian H Abitbol, Peter Ade, Derek Araujo, Kristi Bradford, Robin Cantor, George Che, et al. Photon noise from chaotic and coherent millimeter-wave sources measured with horn-coupled, aluminum lumped-element kinetic inductance detectors. *Applied Physics Letters*, 108(8):083504, 2016.
- [52] Heather McCarrick. *Design and performance of kinetic inductance detectors for cosmic microwave background polarimetry*. PhD thesis, Columbia University, 2018.

- [53] Jiansong Gao. The Physics of Superconducting Microwave Resonators. pages 1–197, May 2008.
- [54] S J C Yates, J J A Baselmans, A Endo, R M J Janssen, L Ferrari, P Diener, and A M Baryshev. Photon noise limited radiation detection with lens-antenna coupled microwave kinetic inductance detectors. *Applied Physics Letters*, 99(7):073505, August 2011.
- [55] H McCarrick, D Flanigan, G Jones, BR Johnson, P Ade, D Araujo, K Bradford, R Cantor, G Che, P Day, et al. Horn-coupled, commercially-fabricated aluminum lumped-element kinetic inductance detectors for millimeter wavelengths. *Review of Scientific Instruments*, 85(12):123117, 2014.
- [56] Y Sekimoto, T Nitta, K Karatsu, M Sekine, S Sekiguchi, T Okada, S Shu, T Noguchi, M Naruse, K Mitsui, et al. Developments of wide field submillimeter optics and lens antenna-coupled mkid cameras. In *Millimeter, Submillimeter, and Far-Infrared Detectors and Instrumentation for Astronomy VII*, volume 9153, page 91532P. International Society for Optics and Photonics, 2014.
- [57] Sunil R Golwala, Clint Bockstiegel, Spencer Brugger, Nicole G Czakon, Peter K Day, Thomas P Downes, Ran Duan, Jiansong Gao, Amandeep K Gill, Jason Glenn, Matthew I Hollister, Henry G Leduc, P R Maloney, Benjamin A Mazin, Sean G McHugh, David Miller, Omid Noroozian, Hien T Nguyen, Jack Sayers, James A Schlaerth, Seth Siegel, Anastasios K Vayonakis, Philip R Wilson, and Jonas Zmuidzinas. Status of MUSIC, the MUltiwavelength Sub/millimeter Inductance Camera. In Wayne S Holland, editor, *SPIE Astronomical Telescopes + Instrumentation*, page 845205. SPIE, September 2012.
- [58] Lorenza Ferrari, Ozan Yurduseven, Nuria Llombart, Stephen JC Yates, Juan Bueno, Vignesh Murugesan, David J Thoen, Akira Endo, Andrey M Baryshev, and Jochem JA Baselmans. Antenna coupled mkid performance verification at 850 ghz for large format astrophysics arrays. *IEEE Transactions on Terahertz Science and Technology*, 8(1):127–139, 2018.

- [59] Tom Nitta, Kenichi Karatsu, Yutaro Sekimoto, Masato Naruse, Masakazu Sekine, Shigeyuki Sekiguchi, Hiroshi Matsuo, Takashi Noguchi, Kenji Mitsui, Norio Okada, Masumichi Seta, and Naomasa Nakai. Close-Packed Silicon Lens Antennas for Millimeter-Wave MKID Camera. *Journal of Low Temperature Physics*, 176(5-6):684–690, December 2013.
- [60] Chenguang Ji, A Beyer, S Golwala, and J Sayers. Design of antenna-coupled lumped-element titanium nitride kids for long-wavelength multi-band continuum imaging. In *Millimeter, Submillimeter, and Far-Infrared Detectors and Instrumentation for Astronomy VII*, volume 9153, page 915321. International Society for Optics and Photonics, 2014.
- [61] J Hubmayr, J Beall, Daniel Becker, Hyeonwoo Cho, B Dober, M Devlin, A M Fox, J Gao, G C Hilton, K D Irwin, Di-Jie Li, M Niemack, D P Pappas, L Vale, and M Vissers. Dual-Polarization Sensitive MKIDs for Far Infrared Astrophysics. *IEEE Transactions on Applied Superconductivity*, 23(3):2400304–2400304, June 2013.
- [62] H McCarrick, G Jones, BR Johnson, MH Abitbol, PAR Ade, S Bryan, P Day, T Essinger-Hileman, D Flanigan, HG Leduc, et al. Design and performance of dual-polarization lumped-element kinetic inductance detectors for millimeter-wave polarimetry. *Astronomy & Astrophysics*, 610:A45, 2018.
- [63] J McMahon, J Beall, D Becker, H M Cho, R Datta, A Fox, N Halverson, J Hubmayr, K Irwin, J Nibarger, M Niemack, and H Smith. Multi-chroic Feed-Horn Coupled TES Polarimeters. *Journal of Low Temperature Physics*, 167(5):879–884, June 2012.
- [64] Shibo Shu, Shigeyuki Sekiguchi, Masakazu Sekine, Yutaro Sekimoto, Tom Nitta, Agnes Dominjon, Takashi Noguchi, Masato Naruse, and Wenlei Shan. Development of octave-band planar ortho-mode transducer with kinetic inductance detector for LiteBIRD. *SPIE Astronomical Telescopes + Instrumentation*, 9914:99142C–99142C–6, July 2016.

- [65] Bradley R Johnson, Daniel Flanigan, Maximilian H Abitbol, Peter A R Ade, Sean Bryan, Hsiao-Mei Cho, Rahul Datta, Peter Day, Simon Doyle, Kent Irwin, Glenn Jones, Sarah Kernasovskiy, Dale Li, Philip Mauskopf, Heather McCarrick, Jeff McMahon, Amber Miller, Giampaolo Pisano, Yanru Song, Harshad Surdi, and Carole Tucker. Polarization sensitive Multi-Chroic MKIDs. In Wayne S Holland and Jonas Zmuidzinas, editors, *SPIE Astronomical Telescopes + Instrumentation*, page 99140X. SPIE, July 2016.
- [66] B A Mazin, S R Meeker, M J Strader, P Szypryt, D Marsden, J C van Eyken, G E Duggan, A B Walter, G Ulbricht, M Johnson, B Bumble, K O’Brien, and C Stoughton. ARCONS: A 2024 Pixel Optical through Near-IR Cryogenic Imaging Spectrophotometer. *Publications of the Astronomical Society of the Pacific*, 125(933):1348–1361, November 2013.
- [67] A Monfardini, L J Swenson, A Bideaud, F X Désert, S J C Yates, A Benoît, A M Baryshev, J J A Baselmans, S Doyle, B Klein, M Roesch, C Tucker, P Ade, M Calvo, P Camus, C Giordano, R Guesten, C Hoffmann, S Leclercq, P Mauskopf, and K F Schuster. NIKA: A millimeter-wave kinetic inductance camera. *Astronomy and Astrophysics*, 521:A29, October 2010.
- [68] Shibo Shu, Martino Calvo, Johannes Goupy, Andrea Catalano, Aurelien Bideaud, Alessandro Monfardini, Samuel Leclercq, and Eduard FC Driessen. Optical response of lumped-element kinetic-inductance detector arrays. *IEEE Transactions on Terahertz Science and Technology*, 8(6):605–612, 2018.
- [69] Benjamin A Mazin. *Microwave kinetic inductance detectors*. PhD thesis, California Institute of Technology, 2005.
- [70] R M J Janssen, J J A Baselmans, A Endo, L Ferrari, S J C Yates, A M Baryshev, and T M Klapwijk. High optical efficiency and photon noise limited sensitivity of microwave kinetic inductance detectors using phase readout. *Applied Physics Letters*, 103(20):203503, November 2013.

- [71] Simon Doyle. *Lumped element Kinetic Inductance Detectors*. PhD thesis, Cardiff University, 2008.
- [72] Markus J Rosch, Francois Mattiocco, Theo A Scherer, Michael Siegel, and Karl-Friedrich Schuster. Modeling and Measuring the Optical Coupling of Lumped Element Kinetic Inductance Detectors at 120-180 GHz. *IEEE Transactions on Antennas and Propagation*, 61(4):1939–1946, 2013.
- [73] ANSYS HFSS Software HP: <https://www.ansys.com/products/electronics/ansys-hfss>.
- [74] M Roesch, A Benoit, A Bideaud, N Boudou, M Calvo, A Cruciani, S Doyle, HG Leduc, A Monfardini, L Swenson, et al. Development of lumped element kinetic inductance detectors for nika. *arXiv preprint arXiv:1212.4585*, 2012.
- [75] Markus Rösch. *Development of lumped element kinetic inductance detectors for mm-wave astronomy at the IRAM 30 m telescope*, volume 12. KIT Scientific Publishing, 2014.
- [76] J Goupy, A Adane, A Benoit, O Bourrion, M Calvo, A Catalano, G Coiffard, C Hoarau, S Leclercq, Hélène Le Sueur, et al. Microfabrication technology for large lekid arrays: From nika2 to future applications. *Journal of Low Temperature Physics*, 184(3-4):661–667, 2016.
- [77] T Durand. *Réalisation d’un interféromètre de Martin-Puplett pour le développement d’une caméra bolométrique*. PhD thesis, Université Joseph-Fourier, 2007.
- [78] Shibo Shu, Martino Calvo, Samuel Leclercq, Johannes Goupy, Alessandro Monfardini, and EFC Driessen. Prototype high angular resolution lekids for nika2. *Journal of Low Temperature Physics*, 193(3-4):141–148, 2018.
- [79] Matthew J Griffin, James J Bock, and Walter K Gear. Relative performance of filled and feedhorn-coupled focal-plane architectures. *Applied Optics*, 41(31):6543, 2002.

- [80] Sonnet Software HP: <http://www.sonnetsoftware.com/>.
- [81] D S Wisbey, A Martin, A Reinisch, and J Gao. New Method for Determining the Quality Factor and Resonance Frequency of Superconducting Micro-Resonators from Sonnet Simulations. *Journal of Low Temperature Physics*, 176(3-4):538–544, May 2014.
- [82] Omid Noroozian, Peter K Day, Byeong Ho Eom, Henry G Leduc, and Jonas Zmuidzinas. Crosstalk Reduction for Superconducting Microwave Resonator Arrays. *IEEE Transactions on Microwave Theory and Techniques*, 60(5):1235–1243, 2012.
- [83] Shibo Shu, Martino Calvo, Johannes Goupy, Samuel Leclercq, Andrea Catalano, Aurelien Bideaud, Alessandro Monfardini, and Eduard FC Driessen. Increased multiplexing of superconducting microresonator arrays by post-characterization adaptation of the on-chip capacitors. *Applied Physics Letters*, 113(8):082603, 2018.
- [84] PD Mauskopf, S Doyle, P Barry, S Rowe, A Bidead, PAR Ade, C Tucker, E Castillo, A Monfardini, J Goupy, et al. Photon-noise limited performance in aluminum lekids. *Journal of Low Temperature Physics*, 176(3-4):545–552, 2014.
- [85] L Bisigello, S J C Yates, L Ferrari, J J A Baselmans, and A Baryshev. Measurements and analysis of optical crosstalk in a microwave kinetic inductance detector array. *SPIE Astronomical Telescopes + Instrumentation*, 9914:99143L–99143L–8, July 2016.
- [86] Michael R Vissers, Jiansong Gao, Martin Sandberg, Shannon M Duff, David S Wisbey, Kent D Irwin, and David P Pappas. Proximity-coupled Ti/TiN multilayers for use in kinetic inductance detectors. *Applied Physics Letters*, 102(23):232603, June 2013.
- [87] A Adane Jr, C Boucher, G Coiffard, S Leclercq, K F Schuster, J Goupy, M Calvo, C Hoarau, and A Monfardini. Crosstalk in a KID Array Caused by the Thickness

- Variation of Superconducting Metal. *Journal of Low Temperature Physics*, 184(1-2):1–5, 2016.
- [88] Christopher M McKenney, Jason E Austermann, James A Beall, Bradley J Dober, Shannon M Duff, Jiansong Gao, Gene C Hilton, Johannes Hubmayr, Dale Li, Joel N Ullom, et al. Tile-and-trim micro-resonator array fabrication optimized for high multiplexing factors. *Review of Scientific Instruments*, 90(2):023908, 2019.
- [89] SJC Yates, JJA Baselmans, AM Baryshev, Simon Doyle, A Endo, L Ferrari, S Hochgürtel, and B Klein. Clean beam patterns with low crosstalk using 850 ghz microwave kinetic inductance detectors. *Journal of Low Temperature Physics*, 176(5-6):761–766, 2014.
- [90] Michael R Vissers, Jiansong Gao, Jeffrey S Kline, Martin Sandberg, Martin P Weides, David S Wisbey, and David P Pappas. Characterization and in-situ monitoring of sub-stoichiometric adjustable superconducting critical temperature titanium nitride growth. *Thin Solid Films*, 548:485–488, 2013.
- [91] X Liu, W Guo, Y Wang, LF Wei, CM Mckenney, B Dober, T Billings, J Hubmayr, LS Ferreira, MR Vissers, et al. Cryogenic led pixel-to-frequency mapper for kinetic inductance detector arrays. *Journal of Applied Physics*, 122(3):034502, 2017.
- [92] X Liu, W Guo, Y Wang, M Dai, LF Wei, B Dober, CM McKenney, GC Hilton, J Hubmayr, JE Austermann, et al. Superconducting micro-resonator arrays with ideal frequency spacing. *Applied Physics Letters*, 111(25):252601, 2017.
- [93] Sergey K Tolpygo, Vladimir Bolkhovsky, TJ Weir, CJ Galbraith, Leonard M Johnson, Mark A Gouker, and Vasili K Semenov. Inductance of circuit structures for mit ll superconductor electronics fabrication process with 8 niobium layers. *IEEE Transactions on Applied Superconductivity*, 25(3):1–5, 2015.

- [94] Faustin Wirkus Carter, Trupti S Khaire, Valentyn Novosad, and Clarence L Chang. scraps: an open-source python-based analysis package for analyzing and plotting superconducting resonator data. *IEEE Transactions on Applied Superconductivity*, 27(4):1–5, 2016.
- [95] M Calvo, M Roesch, F-X Désert, Alessandro Monfardini, Alain Benoit, Philip Mauskopf, P Ade, N Boudou, O Bourrion, P Camus, et al. Improved mm-wave photometry for kinetic inductance detectors. *Astronomy & Astrophysics*, 551:L12, 2013.